Aerosol cloud interactions in southeast Pacific stratocumulus: satellite observations, in situ data and regional modeling

Rhea George

A dissertation
submitted in partial fulfillment of the
requirements for the degree of

Doctor of Philosophy

University of Washington

2013

Reading Committee:

Robert Wood, Chair

Chris Bretherton

David Covert

Joel Thornton

Program Authorized to Offer Degree:
Atmospheric Sciences

University of Washington

Abstract

Aerosol cloud interactions in southeast Pacific stratocumulus: satellite observations, in situ data and regional modeling

Rhea George

Chair of the Supervisory Committee:
Title of Chair Robert Wood
Atmospheric Sciences

The influence of anthropogenic aerosols on cloud radiative properties in the persistent southeast Pacific stratocumulus deck is investigated using MODIS satellite observations, in situ data from the VAMOS Ocean-Cloud-Atmosphere-Land Study Regional Experiment (VOCALS-REx), and WRF-Chem, a regional model with interactive chemistry and aerosols. An albedo proxy is derived based on the fractional coverage of low cloud (a macrophysical field) and the cloud albedo, with the latter broken down into contributions from microphysics (cloud droplet concentration, N_{d}) and macrophysics (liquid water path). Albedo variability is dominated by low cloud fraction variability, except within 10–15° of the South American coast, where cloud albedo variability contributes significantly. Covariance between cloud fraction and cloud albedo also contributes significantly to the variance in albedo, which highlights how complex and inseparable the factors controlling albedo are. N_{d} variability contributes only weakly, which emphasizes that attributing albedo variability to the indirect effects of aerosols against the backdrop of natural meteorological variability is extremely challenging.

Specific cases of aerosol changes can have strong impacts on albedo. We identify a pathway for periodic anthropogenic aerosol transport to the unpolluted marine stratocumulus >1000 km offshore, which strongly enhances N_{d} and albedo in in zonally-elongated 'hook'-shaped arc. Hook development occurs with N_{d} increasing to polluted levels over the remote

ocean primarily due to entrainment of a large number of small aerosols from the free troposphere that contribute a relatively small amount of aerosol mass to the marine boundary layer. Strong, deep offshore flow needed to transport continental aerosols to the remote ocean is favored by a trough approaching the South American coast and a southeastward shift of the climatological subtropical high pressure system. DMS significantly influences the aerosol number and size distributions, but does not cause hooks.

The Twomey effect contributes 50-80% of the total aerosol indirect effect (AIE) both near sources and offshore during hook events. Meteorological variability between simulations can swamp the signal of AIEs, particularly due to the binary model cloud fraction field and distinguishing AIE requires determination of appropriate spatial and temporal averaging scales over which AIE is significant above this noise.

TABLE OF CONTENTS

LIST OF FIGURES

LIST OF TABLES

ACKNOWLEDGMENTS

Foremost I would like to express sincere gratitude to Robert Wood, who made my graduate experience exciting, challenging, and intriguing with his shear force of intellectual curiosity. I truly appreciated his guidance throughout this program. He allowed me freedom to develop independent research ideas (and direct a research aircraft as "mission scientist"!), while maintaining a helpful level of contact with the details of the project. I would also like to thank Chris Bretherton, an intellectual and adventure guru whose insights and perspective improved the project and running adventures. I am also greatly appreciative of Dave Covert, who joined my committee for the post-Masters work. His enthusiasm and curiosity were infectious and his insights were incredibly helpful. Joel Thornton also provided fresh and helpful questions of the work and I thank him for his help. Terri Klinger exceeded her duties as GSR and was wonderfully supportive and inquisitive about this work and my experience. Also, the support of Marc Michelson made this work possible, and in many cases he saved the day. My officemates, Jennifer and Rob N., made coming to the office a joyful experience and exposed me the world outside of my own interests. All of those who ran with me or simply let me babble about running are awesome human beings that helped encourage me to have a balance between work and play. Those who listened to the details of my project deserve are particularly appreciated, as this was essential toward result refinement. I am incredibly appreciative of my parents, Ted and Lynette, and brother, Jason, for an idyllic childhood and continuing support deep into adulthood. Their encouragement and belief in me bolstered my self confidence and helped drive me. Finally, I am incredibly amazed by and grateful to Toffer, who not only provided daily support and encouragement over the last 5 years, but also remained patient and understanding throughout my changing busy schedule and motivated me with adventurous kayak and backpacking trips. He has been a constant source of joy, humor, and inspiration.

Chapter 1

INTRODUCTION

1.0.1 Motivation

Atmospheric aerosol concentrations have increased markedly over the industrial age due to human activity, but the quantitative impact of these anthropogenic aerosols on Earth's radiative budget continues to elude scientists. Despite numerous rigorous studies over the last few decades involving measurements in field campaigns, satellite data and models, aerosols still represent a highly uncertain, and also significant, portion of the anthropogenic radiative forcing (Haywood and Boucher, 2000), which contributes to uncertainty in the magnitude of the total anthropogenic contribution to climate change (Randall et al., 2007).

The direct effect of aerosols upon solar and infrared radiation involves the direct interaction between aerosol particles and the radiation field. Its magnitude is uncertain (Schultz et al., 2006), but not as uncertain as the so-called indirect effect, which is a primary source of uncertainty in the anthropogenic impact on the global radiative budget (Randall et al., 2007) and precludes accurate determination of Earth's climate sensitivity (Kiehl and Jeffrey, 2007). Aerosols affect the radiative budget indirectly by affecting cloud microphysical and macrophysical properties (Lohmann and Feichter, 2007; Stevens and Feingold, 2009). The aerosol impacts upon the cloud radiative field are collectively termed aerosol indirect effects (AIE). The first AIE (also known as the 'Twomey' effect, Twomey, 1974) describes how, in the absence of changes in cloud macrophysical properties, increased aerosol concentrations lead to increased cloud albedo by increasing the droplet concentration N_{d} and total surface area comprised by droplets. Aerosol dynamical processes including nucleation, coagulation, cloud processing, condensation, and deposition determine the aerosol size distribution and number concentration of aerosols available to activate as cloud droplets. These aerosol characteristics as well as chemical composition (which influences hygroscopicity), mixing state and environmental properties (such as relative humidity, vertical velocity, and supersatu-

ration) determine how many aerosols activate to form cloud droplets (Penner et al., 2001) and influence the magnitude of the first AIE.

Secondary[1] AIEs encompass the changes to cloud *macrophysical* properties that occur in response to cloud microphysical changes. Most well-studied of these effects is a suppression of precipitation as N_{d} increases (Albrecht et al., 1990), which can either enhance or offset the first indirect effect by changing the moisture budget and entrainment rate (Ackerman et al., 2004; Wood, 2007). Observational evidence from in situ flight data in stratocumulus indicates aerosols can significantly impact precipitation rates (Terai et al., 2011). Other secondary effects include the influence of cloud droplet size upon condensation and evaporation rates (Wang et al., 2003; Xue and Feingold, 2006) and upon the entrainment rate through changes to the cloud droplet sedimentation flux (Bretherton et al., 2007).

The radiative forcing due to the first aerosol indirect effect has been estimated using global climate models (GCMs)to be in the range 0.25 to 1.75 Wm^{-2} with the large range evincing the low confidence we have in AIEs (Intergovernmental Panel on Climate Change-IPCC, Randall et al., 2007). The total uncertainty including secondary AIEs is even larger and depends on which secondary effects are included in each particular GCM (Lohmann and Feichter, 2007; Isaksen et al., 2009). The total AIE uncertainty stems from uncertainties in aerosol emissions and physicochemical processes, uncertainties in how aerosols affect cloud microphysical properties, and in how clouds respond dynamically to changes in their microphysics.

Both observational and modeling studies can contribute to reducing the uncertainties in the magnitude of the AIEs, but each has its own set of limiting factors. Generally, the wide range of scales involved from microphysical processes to their net impact on the global radiation budget causes computational challenges in model studies, while observational studies struggle with untangling the inherent covariability of meteorological and aerosol-related processes (Stevens and Feingold, 2009). In-situ measurement studies (typically collected using an instrumented research aircraft) demonstrate important relationships between aerosols and cloud parameters, such as the correlation between warm cloud microphysical properties

[1]The term 'secondary' should not be taken to imply that these effects are of secondary importance

and accumulation mode (particles in size range 0.1-1 μm) aerosol concentrations (Twomey and Warner 1967, Martin et al., 1994). However, in-situ observational studies are limited to intensive field studies and so there is a need to develop more regional observational approaches.

Satellite measurements provide the tools for such an approach. A number of satellite-based attempts to estimate the effects of aerosols on cloud properties have been made using present-day correlations between aerosols and cloud properties (e.g. Wetzel and Stowe, 1999; Breon et al., 2002; Kaufman et al., 2005; Quaas et al., 2008; Lebsock et al., 2008), but may be somewhat questionable due to covarying meteorological and aerosol impacts on clouds (e.g. Brenguier et al., 2003; Mauger and Norris, 2007; Stevens and Brenguier, 2009; George and Wood, 2010). Additionally, because satellite aerosol measurements require the absence of clouds, and cloud measurements require the presence of clouds, assigning some degree of causality to these correlations requires a major assumption that the aerosol properties at a location do not differ significantly in times when it is cloudy from times when there are no clouds. Little exploration of the likely impact of this assumption on derived AIE estimates has been carried out.

Model studies can simulate collocated aerosol and cloud properties and control for meteorology, but are limited by computing power, either by the need to parameterize small scale processes in larger scale climate models, or by a lack of generality for cloud resolving models. Paramaterizations that represent turbulence, entrainment, and subgrid variability in cloud microphysics introduce uncertainty into global model estimates of indirect effects. Although many well-tested, intelligently designed cloud parameterizations exist, behavior within larger scale models can be unexpectedly complex, especially if a parameterization has not been designed explicitly for use in a particular model. The specific combination of parameterizations chosen for a particular model simulation can affect the GCM results and there is a need for more intensive model validation techniques. High resolution cloud resolving models can lend insight into the physical mechanisms and behaviors of AIEs on small scales, but it is not straightforward to upscale their findings to coarser scale models that cover larger areas and are subject to larger scale meteorological variability. Models need observational constraints to gain confidence in the model representation of real pro-

cesses, but many large-scale model studies do not use observational metrics relevant to the representation of microphysics and microphysical variability. Thus the magnitude of aerosol impacts on radiation varies considerably between global climate models (GCMs) and contributes to the large uncertainty in AIEs computed from an aggregate of model results and produced for the IPCC.

Because the global aerosol indirect effect problem is so challenging, it makes sense to choose the simplest system one can find while maintaining some degree of realism. Breaking the problem into pieces and examining it systematically at the regional scale is one approach to combining simplification and realism. Stratocumulus cloud albedo is susceptible to aerosols (Platnick and Twomey, 1994) and the relatively plane parallel nature of stratocumulus clouds allows their macrophysical and microphysical properties to be determined reasonably accurately using passive satellite remote sensing (e.g. Painemal and Zuidema, 2011). Stratocumulus clouds are characterized by their low height (typically below the freezing temperature height in the tropic and subtropics) and extensive horizontal extent. These clouds thus do not trap much terrestrial radiation and reflect solar radiation effectively (high albedo), resulting in a strongly negative top of atmosphere cloud radiative forcing (Hartmann and Short, 1980). Their strong impact on radiation and prevalence over much (more than 25% of low cloud cover; Wood, 2012) of the ocean (where the albedo of the cloud is much higher than the albedo of the surface) cause this cloud type to have an important effect on the net energy balance of the earth (Hartmann et al., 1992). Despite this, marine stratocumulus clouds continue to be difficult to simulate accurately in general circulation models (Ma et al., 1996; Zhang et al., 2005; Hannay et al., 2009; Wyant, 2010). Additionally many stratocumulus regions are influenced by local and remotely transported anthropogenic pollution from a nearby continent (Wood, 2012). Stratocumulus cloud regions therefore constitute a system that is both well documented with observational data and is need of improvement in model representation, which provides an excellent opportunity to improve characterization of AIEs and low cloud variability.

To fully understand the strength of aerosol impacts on clouds independent of meteorology, it is fundamentally important to understand how meteorology impacts cloud properties (such as areal extent, time duration, albedo, and depth) independent of aerosol changes

(Stevens and Brenguier, 2009). On seasonal to interannual time scales, variations in low cloud amount are strongly correlated with variations in lower tropospheric stability (LTS), sea surface temperature, and atmospheric circulation (Klein and Hartmann, 1993; Wood and Bretherton, 2006; Norris and Leovy, 1994). On sub-seasonal timescales, correlations of low cloud amount with meteorological predictors are substantially weaker than on longer timescales, but LTS, relative humidity of the cloud layer (defined at 90% of the trade inversion height), and cold advection do significantly correlate with variations in low cloud amount (Klein et al., 1995; Klein, 1997). Similar correlations exist with cloud liquid water path (Xu et al., 2005). Some variations in microwave-estimated liquid water path largely reflect variations in cloud cover since microwave data do not allow separation into cloudy and clear contributions, but we also know that overcast stratocumulus have considerable variations in liquid water path (Wood and Taylor, 2001). Keeping in mind these meteorological processes that influence low clouds, regions of stratocumulus are an appropriate cloud type in which to quantify the impact of aerosols.

1.0.2 Region of study

The largest and most persistent deck of subtropical marine stratocumulus clouds swathes the Southeast Pacific (SEP; ∼10-40°S, 70-90°W) off the coast of South America (Richter and Mechoso 2004; Bretherton et al., 2004). Between 30°S and 30°N in regions of strong subsidence, tropical boundary layer clouds are the dominant contributors to aerosol-cloud feedback uncertainty (Bony and Dufresne, 2005), so the SEP situated in the southern range of this impact is suitable for reducing this uncertainty. A persistent subtropical high pressure system exists throughout the year centered near 30° S, 90° W. A descending branch of the Hadley cell circulation together with the Andes blocking of low-level westerly flow drives southerly flow along the South American coast and southeasterly flow around the high (Richtor and Mechoso, 2004; Toniazzo et al., 2011). This flow encourages lower tropospheric transport of continental air to the SEP (Yang et al., 2011; Allen et al., 2011; Saide et al., 2012). Further, the Andes high barrier within 200km of the coast discourages eastward transport of continental aerosols. The Andes interact with synoptic scale dynamics (through

mechanisms such as diurnal pumping and coastal low formation), leading to episodic outflow of continental boundary layer air into the marine free troposphere (FT; Rahn and Garreaud, 2010b; Allen et al., 2011; Toniazzo et al., 2011). Due to subsidence associated with the subtropical high (Klein and Hartmann, 1993) and increasing marine boundary layer (MBL) depth with distance from the coast (Bretherton et al., 2010), this continental air can be transported by winds moving to the northwest and may eventually intersect the marine inversion and be entrained into the MBL (Allen et al., 2011).

The large-scale meteorology establishes not just the advection of continental aerosols, but also maintains the persistent stratocumulus clouds. The subtropical high-related winds cause upwelling of cold ocean water near the coast (Bretherton et al., 2004). Dry subsiding air associated with the subtropical high warms the air above the MBL, which can be entrained into the MBL, leading to cooling of the ocean surface by evaporation (e.g. Takahashi and Battisti, 2007). Hence the SEP is a region of cold sea surface temperatures and strong LTS harboring extensive marine stratocumulus year-round (Richter and Mechoso, 2004). Figure 1.1 shows the mean state of cloud variables and the radiatively relevant quantity (proxy) albedo derived from satellite data in the SEP from 2000-2008. Mean surface winds overplotted with the albedo from NCEP reanalysis shows the location of the subtropical high and the dominant flow. Annual mean low cloud cover exceeds 60% over a large region and approaches 80% at the heart of the deck (Fig.1.1b). The spatial pattern of mean cloud fraction, f_c, in the SEP is well-correlated with that in LTS as it is in other stratocumulus regions (e.g. Wood and Bretherton, 2006; Klein and Hartmann, 1993), consistent with strong meteorological controls on the mean cloud field.

Anthropogenic aerosols emitted along the Chilean and Peruvian coastlines advect over the stratocumulus dominated SEP (Huneeus et al., 2006; Allen et al., 2011). Precursor gaseous species affect aerosols through in-cloud processing, contribute to new aerosol formation through nucleation, or condense onto pre-existing particles (Seinfeld and Pandis, 1998). Anthropogenic emissions of sulfate, organic and other primary and secondary aerosols as well as their gaseous precursors (such as SO_2 which oxidizes to sulfate) that are transported to the SEP originate mainly from industrial and urban sources, including copper mining and the Santiago metropolis (Tsapakis et al., 2002; Schüller et al., 2008). Santiago's

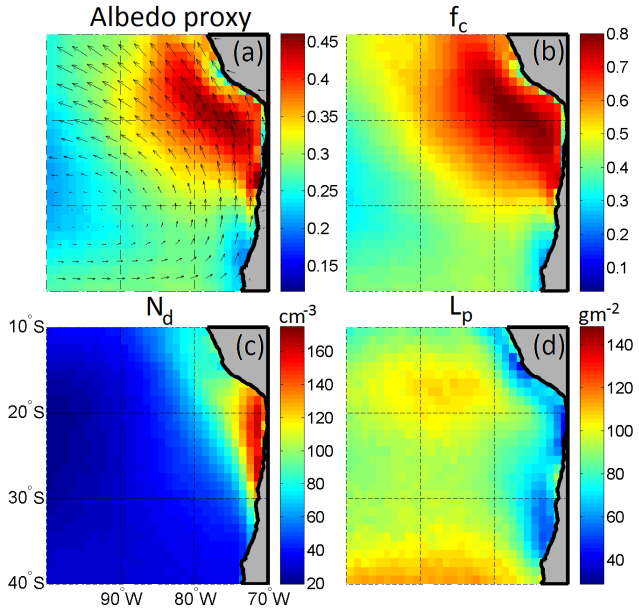

Figure 1.1: 2000-2008 mean of (a) low cloud albedo proxy and controlling variables derived from MODIS data: (b) low cloud fraction f_c, (c) cloud droplet concentration N_d, and (d) cloud liquid water path L_p. Vectors in (a) are mean surface horizontal winds with maximum magnitude of 8 m/s in the longest arrows

emissions combined with topographic transport restrictions causes this city to have one of the largest mass loadings of PM10 (aerosols smaller than 10 μm) in the world (>50 μgm^{-3} in 2006, Muñoz and Alcafuz, 2012). Natural emissions from volcanic and biogenic sources and DMS oxidation products from the ocean also contribute to the concentration of cloud condensation nuclei. While the contribution from ocean sources is uncertain (e.g. Bates et al., 1992), the oceanic reduced sulfur source is unlikely to be sufficient to explain the high droplet number concentrations downwind of the urban sources (Yang M. et al., 2011).

The pattern of mean cloud droplet concentration N_d (Fig.1.1c), largely reflects the spatial variation of accumulation mode aerosol number concentration (Wood et al., 2008) and is evidence of the strong continental aerosol sources. The dominant large scale meteorological variability relevant for producing patterns of clouds seen in Fig.1.1 is associated with the subtropical high pressure system. Two indices representing changes in the subtropical high strength, and extent explain 80–90% of the subseasonal sea level pressure variability over

2000-2008, and significantly modulate the cloud microphysical, macrophysical, and radiative cloud properties (George and Wood, 2010). Temporal variations in droplet concentration of up to 50% of the mean are associated with the meteorological driving, as well as enhanced cloud cover, but cannot isolate the aerosol transport and aerosol-independent contributions to this change because it solely uses observations (George and Wood, 2010). For example enhanced droplet concentration and cloud amount following days of strong subtropical high could potentially be caused by stronger offshore flow of aerosols, higher aerosol concentrations in the boundary layer and hence more activation and more cloud. Alternatively the increase in cloud amount could be due to stronger subsidence, a lower boundary layer and higher lower tropospheric stability associated with a stronger subtropical high. The N_{d} may change purely due to changes in entrainment of aerosol from the FT.

It is nonetheless recognized that the transport of anthropogenic aerosol and precursors from continents to remote marine regions impacts cloud microphysical and radiative properties (Schwartz et al., 2002). Given the attribution of near-shore large concentrations of N_{d} to anthropogenic sources (e.g., Allen et al., 2011), it is not unreasonable to expect meteorological conditions favoring offshore transport of aerosols to affect the variability of the SEP stratocumulus cloud properties. The clouds over the SEP forming in extremely clean air originating in the remote southern Pacific are particularly susceptible to aerosol increases. The SEP is therefore a region of strong mean-state contrasts between clean and polluted airmasses, but also of strong microphysical variability affected by a combination of meteorological conditions and aerosol processes. The SEP is thus a useful region for characterizing both the mean and variability of aerosol impacts, with an appropriate method for distinguishing aerosol effects from meteorological effects unrelated to aerosol transport.

Additionally, the VAMOS Ocean-Cloud-Atmosphere-Land Study Regional Experiment (VOCALS-REx; Wood et al., 2011a) that took place 15 October-16 November 2008 provides a wealth of in situ flight and ship data over the SEP. This dataset, combined with satellite data can inform a regional model that reasonably reproduces these observations provides a wealth of information about the region. With these three tools at our disposal, the SEP is notably situated to study aerosol-cloud interactions and their impact on radiation.

1.0.3 Approach

To study AIEs over the SEP we identify albedo, the fraction of incoming solar radiation reflected back to space, as the radiatively relevant quantity impacted indirectly by aerosols through aerosol-cloud interactions. The average albedo, α, of a region is simply related to the albedo of cloud and cloud fraction by the conventional relationship (Cess, 1976):

$$\alpha = f_c \alpha_{\rm cld} + (1 - f_c)\alpha_{\rm clear} \tag{1.1}$$

where $f_{\rm c}$ is the fraction of sky covered by low cloud, $\alpha_{\rm cld}$ is the cloud albedo and $\alpha_{\rm clear}$ the clear sky albedo. Over the ocean $\alpha_{\rm clear}$ variability is weak compared with the other variables involved (Loeb and Kato, 2002) and we assume a constant value of 0.1 in accordance with satellite broadband radiometric observations (Bony et al., 1992). The cloud albedo $\alpha_{\rm cld}$ is a function of optical depth, τ, and the incident solar zenith angle. We make the conservative scattering assumption (single scattering albedo $\omega_0 = 1$). Ignoring solar absorption, since its impact on albedo is small (Kindel et al., 2011), $\alpha_{\rm cld}$ solely depends on optical depth (τ) and the solar zenith angle, and not wavelength. We use a typical value of the asymmetry factor $g = 0.85$ for scattering by liquid cloud droplets with negligible absorption at visible wavelengths (Twohy et al., 2005). The cloud layer is assumed to be plane parallel. Even in relatively uniform stratocumulus clouds this assumption can introduce an albedo bias due to horizontally inhomogeneous $L_{\rm p}$ (e.g. Cahalan et al., 1994), but we do not account for this here. Based on Eq.(37) in King and Harshvardhan (1986), $\alpha_{\rm cld}$ is calculated using the two-stream approximation via the delta-Eddington method for conservative scattering. This method is accurate to better than 5% for values of solar zenith angle less than 60° and τ>0.9, which comprises most of the SEP region daytime properties (George and Wood, 2010).

A clear distinction of microphysical impacts from macrophysical ones, or equivalently of 1$^{\rm st}$ AIEs from 2$^{\rm nd}$ AIEs, can be made by noting that τ is a function of cloud droplet concentration, $N_{\rm d}$, and cloud liquid water path, $L_{\rm p}$ (Boers et al., 1995). We consider cloud droplet concentration, $N_{\rm d}$, rather than cloud droplet effective radius, as our fundamental cloud microphysical parameter, for three reasons: (a) droplet concentration is more funda-

mentally related to the underlying aerosol concentration than is the effective radius (e.g. Martin et al., 1994); (b) droplet concentration tends to be relatively constant with height in cloud whereas effective radius is strongly height dependent (e.g. Slingo et al., 1982); (c) for a given droplet concentration, the effective radius increases with increasing cloud liquid water, which causes undesirable "crosstalk" between the macrophysical variable L_{p} and r_{e} (Schuller et al., 2005).

We can thus think of N_{d} (a microphysical quantity), L_{p}, and f_{c} (macrophysical quantities) as being the three fundamental contributors to albedo and albedo variability. The influence of these parameters on albedo variability was not systematically explored before George and Wood (2010). For the IPCC fourth assessment report (Randall et al., 2007), estimates of the Twomey effect alone were used by GCMs to estimate the contribution of anthropogenic aerosols. There is a tendency in recent literature to either lump all indirect effects into one total AIE metric or identify the first AIE as the relevant quantity. The inconsistency between model representation of AIEs is a good reason to ignore AIE distinctions when comparing multiple models (Quass et al., 2009), but the downside is that this neglects understanding of the physics and cloud feedbacks through which AIEs occur. By evaluating the relative contribution of the 2nd AIEs compared to the 1st in this work we gain an estimate of the strength of the cloud feedbacks between microphysical and macrophysical parameters, as well as how aggregation of the microphysical scale affects the macrophysical scale. Aerosols are directly connected to N_{d} through cloud droplet activation processes, and distinguishing this from secondary impacts of macrophysics and albedo allows for a clear process based separation of AIEs.

This body of work aims to contribute to an understanding of the indirect effect of anthropogenic aerosols on albedo through their influence on cloud microphysics and subsequently, macrophysics, against a convolved background of meteorological and thermodynamic processes. Chapter 2 investigates subseasonal variability in SEP albedo using satellite data over 2000-2008. It establishes a method to quantify microphysical and macrophysical process impacts on albedo variability. However, contributions from the inherent covariability of cloud variables through feedback mechanisms and similar responses to meteorological conditions are not negligible and make this a challenging problem to analyze with observa-

tions alone. In Chapter 3 we describe and evaluate a regional model using new observations with online embedded chemistry, WRF-Chem, to study this problem. Chapter 4 uses this model to investigate development and impact of hooks, arc-shaped features of high droplet concentration that extend into the clean remote ocean and induce aerosol effects on cloud properties and radiation. These represent strong offshore anthropogenic aerosol transport events and allow us to study individual cases of strong AIEs. In Chapter 5 we establish a metric for evaluating the relative contributions of 1st and 2nd AIE over the SEP REx period. We then evaluate the strength and variability of AIE as a function of spatial and temporal scales of averaging.

Chapter 2

MODIS ALBEDO VARIABILITY

This chapter investigates SEP albedo variability using MODIS-derived cloud data. We construct an estimate of the top-of-atmosphere albedo using this data and derive a method separating dominant controls on albedo variance.

2.1 Data:Albedo proxy

We use spatially averaged 1×1° daily MODIS Level 3 data (derived from Level 2 cloud retrieval data, King et al., 1997) from the NASA Terra satellite for the time period 2000–2008 to derive an approximate, once-daily proxy estimate of the albedo, α. We investigate the dominant sources of subseasonal variability in this albedo estimate over the oceanic part of a spatial domain of 10–40° S and 70–100° W.

To construct the albedo estimate of Eq. 1.1, we begin with MODIS retrievals of effective radius, r_e, low cloud fraction (f_c, the fraction of the sky covered by clouds with cloud top temperatures warmer than 273 K), and cloud optical depth, τ. The main cloud variables of interest, L_p and N_d, are derived from the retrieved τ and r_e assuming that the liquid water content increases linearly with height in the cloud layer (Szczodrak et al., 2001):

$$N_d = K\tau^{1/2} r_e^{-5/2} \tag{2.1}$$

$$L_p = \frac{5}{9}\rho_w \tau r_e \tag{2.2}$$

where ρ_w is the density of liquid water and $K = 1.125\times10^{-6}\,\mathrm{cm}^{-1/2}$ is a weakly temperature and pressure-dependent thermodynamic constant (Bennartz, 2007), here estimated assuming a temperature of 280 K and a pressure of 900 hPa appropriate for conditions at cloud level over the SEP.

We generate an albedo proxy from Eq. 1.1 by making direct use of the MODIS f_c data, and by deriving α_{cld} from τ (MODIS), the incident solar zenith angle, the single scattering albedo (ω_0), and the asymmetry factor (g), employing a simple radiative model. MODIS data are collected at a local time of roughly 10:30 a.m., so we estimate the albedo due to collimated incident radiation (while allowing the solar zenith angle to vary with latitude and day of year). The delta-Eddington method for computing cloud albedo is accurate to better than 5% for values of solar zenith angle less than 60° and τ>0.9 (King and Harshvardhan, 1986), which encompasses most of the cloud retrievals in our dataset (the solar zenith angles at the time of the MODIS retrievals for our domain span 20°–66° and for only 0.3% of retrievals is $0< \tau<0.9$).

In the annual mean the albedo proxy (Fig. 1.1a) correlates strongly with daytime mean CERES albedo (r=0.93), although the MODIS proxy corrected to a top of atmosphere (TOA) is on average 0.04 (14%) higher than the CERES albedo. To correct to the TOA, we use the Fu-Liou radiative transfer model (Fu and Liou, 1992, 1993) applied to data from the EPIC Southeast Pacific stratocumulus cruise (Bretherton et al., 2004), to determine the effects of above-cloud absorption of solar radiation by water vapor and ozone, and above-cloud scattering. From this, an adjustment of the MODIS albedo proxy by a factor of 0.87±0.02 is used to compare with the CERES TOA values. The value is not highly dependent upon water vapor path above the cloud, depending primarily on stratospheric ozone and cloud albedo (Thomas Ackerman, personal communication). Even after this correction, the MODIS derived TOA albedo estimates are still larger than the CERES albedo. This is because (a) MODIS Terra overestimates the daytime mean f_c and L_p because there are significant afternoon decreases in cloud cover and liquid water path in this region (Rozendaal et al., 1995; Wood et al., 2002); (b) we neglect the albedo bias associated with the sub-1° variability in cloud properties, which is estimated to be less than 7.5% for marine low clouds (Rossow et al., 2002). However, neither of these issues is likely to significantly impact the general findings in this study since we are herein concerned with variability rather than the mean albedo.

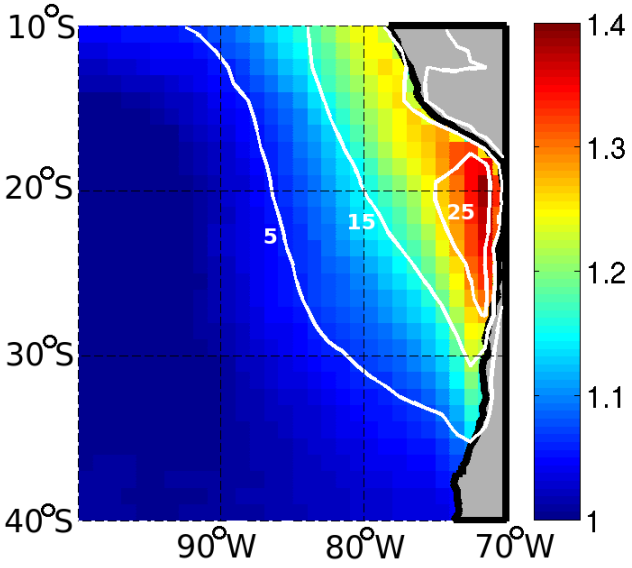

Figure 2.1: The ratio of time-mean albedo calculated with the observed N_d to the mean albedo calculated with the typical marine N_d is shown by the colored contours. To calculate the denominator the observed N_d over time at each point in space is replaced with the average time series of N_d in the domain of 30–40° S, 90–100° W, an area more "pristine" than near the coast providing a good representation of clean marine air. The white contour lines show the time mean of the difference between a diurnal mean estimate of the reflected solar flux and the same flux computed using the typical marine N_d. The numbers indicate Wm^{-2} of flux difference due to the different values for N_d.

2.2 Mean spatial correlations

Before we embark on an examination of the temporal variability of the albedo and its contributing factors, we first explore how the time-mean albedo might be affected by the large spatial variation in time-mean droplet concentration. Figure 2.1 shows the impact of the spatial variations in mean N_d shown in Fig. 1.1c on the mean albedo and the diurnal mean reflected solar flux. Interpreting this as the first aerosol indirect effect is only meaningful if one assumes that there are no cloud macrophysical responses to changes in N_d (i.e. there are no second indirect effects beyond the Twomey effect) or changes in the meteorological forcing. In the absence of such changes, Fig. 2.1 shows that increasing the cloud droplet concentration from remote marine values to values found in the coastal strip would lead to albedo increases of as much as 20–40%, or diurnal mean reflected solar flux

increases of 15–30 Wm^{-2}.

There is a degree of spatial correlation of the patterns of mean N_d with both f_c and the cloud liquid water path L_p north of 30° S within 5–10° of the coast(Fig. 1.1). These spatial correlations do not imply causality, but it seems reasonable to suppose that the time-mean pattern of N_d is affected by the same large scale meteorological processes (i.e. the advection of continentally-influenced airmasses and associated pollutants by the mean winds over the SEP) which also influence cloud cover and liquid water path. Such convolution of the meteorological and aerosol influences on cloud macrophysics makes it difficult to quantify aerosol indirect effects from the mean fields alone despite attempts in the literature to do this (Kaufman et al., 2005).

2.3 Factors influencing the albedo variance

In this section we explore the contributions to the temporal and spatial variability in the albedo from the three fundamental controlling variables f_c, N_d, and L_p using an equation for the variance of albedo dependent on the variances of the controlling variables.

2.3.1 Albedo variance

We can rewrite our albedo proxy (Eq. 1.1) as

$$\alpha = f_c(\alpha_\mathrm{cld} - \alpha_\mathrm{clear}) + \alpha_\mathrm{clear}. \tag{2.3}$$

Because we assume constant α_clear, Eq. 2.3 is a simple product of two variables, f_c and α_cld-α_clear. By redefining each variable x as a sum of a mean $\overline{x}$ and a perturbation value x', the terms can be rearranged (see Appendix A) to obtain an expression for the albedo variance:

$$\begin{aligned}\sigma_\alpha^2 = \overline{\alpha'^2} = \overline{(\alpha_\mathrm{cld} - \alpha_\mathrm{clear})^2 f_c'^2} + \overline{\alpha_\mathrm{cld}'^2 f_c^2} + \\ 2\overline{f_c}(\overline{\alpha_\mathrm{cld}} - \alpha_\mathrm{clear})\overline{\alpha_\mathrm{cld}' f_c'} + \left[-\overline{\alpha_\mathrm{cld}'^2 f_c'^2} - \left(\overline{\alpha_\mathrm{cld}' f_c'}\right)^2\right]\end{aligned} \tag{2.4}$$

2.3.2 Application to temporal variability

The subseasonal albedo variability (Fig. 2.2d) maximizes about five degrees upwind (see Fig. 1.1a for mean surface winds) of the maximum mean cloud cover and albedo (Fig. 1.1b,a). Figure 2.2 shows contributions from each of the terms to the temporal σ_α^2 at different locations throughout the domain. Far from the coast f_c variance dominates albedo variance, but in the region of maximal mean cloud cover (about 10–30° S, 70–90° W, Fig. 1.1b) and about 2–3 degrees upwind of this maximum its contribution is weaker, which makes intuitive sense, since one would expect $\sigma_{f_c}^2$ to be smaller in regions that are more consistently cloudy. This reduced contribution from f_c variance is compensated for by α_{cld} variance, and, particularly on the western side of the maximum in f_c, by the covariance of α_{cld} with f_c. The covariance is positive because for times when clouds have greater cover their liquid water path is also greater. The fourth order terms in Eq. 2.4 contribute 6–10% over most of the domain, and so are generally weaker contributors to albedo variance, but their non-negligibility suggests a relatively high level of complexity in the covariability of cloud cover and cloud albedo. These four terms completely explain the variance in albedo, and thus provide a useful tool for distinguishing the impacts of the variances of the defining variables.

A similar analysis is applied to the cloud optical thickness τ, which almost uniquely[1] determines α_{cld}. Rearranging Eqs. 2.1 and 2.2, we can write

$$\tau = C\mathscr{N}\mathscr{L} \tag{2.5}$$

where C=$\left[\frac{9}{5}\frac{1}{\rho_w K^{2/5}}\right]^{5/6}$=0.2303 $\text{m}^{8/3}\,\text{kg}^{-5/6}$ is effectively a constant (Wood and Hartmann, 2006), $\mathscr{N}$=$N_d^{1/3}$, and $\mathscr{L} = L_p^{5/6}$. This allows us to treat the analysis of τ variance as a product in the same way as we did for f_c and α_{cld} contributions to overall albedo. We see from Fig. 2.3 that $\mathscr{L}$ dominates the α_{cld} variability throughout the domain, although $\mathscr{N}$ makes a significant contribution in the northwest quadrant of the domain, explaining up to 40% of the τ variance. However, the region where the variance of $\mathscr{N}$ contributes most is

[1]It was found that variations in solar zenith angle contributed little to α_{cld} variations compared with variations in τ.

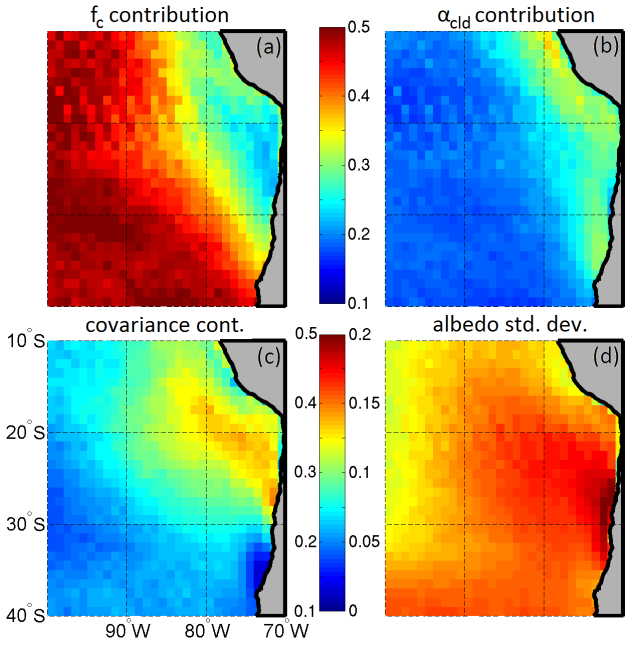

Figure 2.2: Relative fractional contribution of terms in Eq. 2.4 to albedo time variance. The panels show the contributions from the first, second and third terms in the equation, and because the squared coefficients of variation of f_c and α_{cld} are small ($\left(\frac{x'}{\overline{x}}\right)^2$ <1, see Appendix A), the terms represent contributions from **(a)** f_c variance, **(b)** α_{cld} variance, and **(c)** the covariance between f_c and α_{cld} to albedo variance. These are all computed by dividing the corresponding terms by the sum of the absolute value of all terms. 4th order terms are not shown because their relative contribution is smaller (∼6–10%) over most of the domain (up to 21% in small localized regions south of 30° S). **(d)** is the albedo standard deviation.

where the variance of f_c, rather than that of α_{cld} dominates the variance of albedo. A multiplication of the contributions of $\mathscr{N}$ to τ (Fig. 2.3b) by the contribution of α_{cld} to albedo (Fig. 2.2b) gives a rough idea of how much $\mathscr{N}$ contributes to albedo (Fig. 2.4). Interestingly, the contribution of $\mathscr{N}$ variance to overall albedo is strongest downwind of aerosol sources, but the contribution is very small (<10%) throughout the entire domain. Insofar as variations in $\mathscr{N}$ reflect underlying aerosol variability, this suggests that *it is difficult to separate meteorological and aerosol impacts on the albedo using temporal variability since the albedo variability is swamped by variability in cloud fraction and liquid water path.* The covariance between $\mathscr{N}$ and $\mathscr{L}$ constitutes a relatively small contribution to τ (Fig. 2.3c),

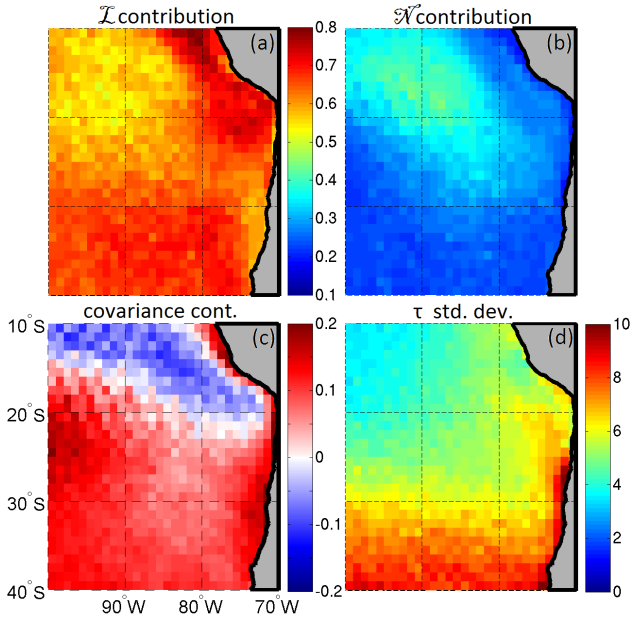

Figure 2.3: Relative fractional contributions of defining terms to τ time variance based on Eqs. (5) and (6). The squared coefficients of variation for $\mathcal{N}$ and $\mathcal{I}$ are small ($\left(\frac{x'}{\bar{x}}\right)^2$ <1, see Appendix A). The panels show the relative contributions from **(a)** $\mathcal{I}$ variance, **(b)** $\mathcal{N}$ variance, and **(c)** the covariance between $\mathcal{N}$ and $\mathcal{I}$, all computed by dividing the corresponding terms by the sum of the absolute value of all terms. 4th order terms (not shown) were negligible (< 6%). **(d)** is the τ standard deviation.

can be either positive or negative depending upon location, and is very similar to the direct correlation between N_d and L_p (not shown).

2.3.3 Application to spatial variability

The same procedure can be applied to the variance in albedo over space. On each day the spatial variance of the $1 \times 1^\circ$ albedo estimates over the domain is derived, as well as fractional contributions from the albedo-controlling variables. We then have time series of fractional contributions of each variable's spatial variance to the albedo spatial variance on each day. The controlling variables contribute to the albedo spatial variance in a similar manner as they did for time variance. Cloud fraction is the largest contributor on 97% of the days, explaining on average 43% of the albedo spatial variance (Table 2.1). Covariance

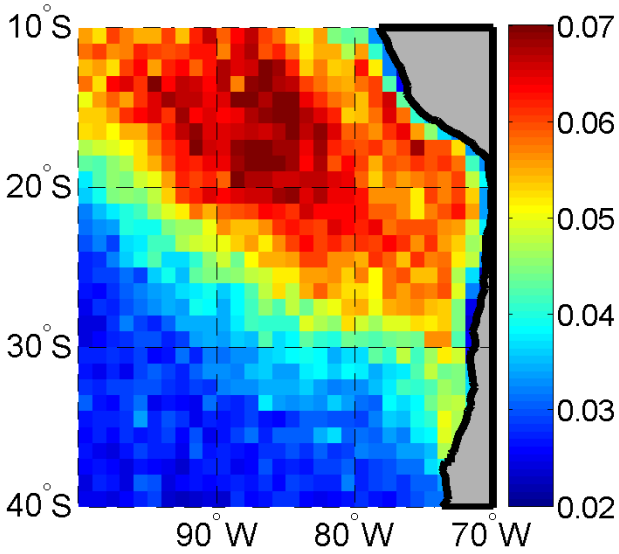

Figure 2.4: Fractional contribution of $\mathscr{N}$, or essentially $N_{\rm d}$, to albedo variance approximated by multiplying the contribution of $\mathscr{N}$ to τ variance (Fig. 2.3b) by the contribution of $\alpha_{\rm cld}$ to albedo variance (Fig. 2.2b).

of $\alpha_{\rm cld}$ with $f_{\rm c}$ is the second largest contributor followed by $\alpha_{\rm cld}$. As is the case for temporal variance, the spatial variance of $N_{\rm d}$ rarely explains more than 10% of the albedo spatial variance. The domain mean fractional increase in albedo associated with the mean pattern of $N_{\rm d}$ (Fig. 2.1) is 12%, so this is consistent. Thus both the temporal *and* spatial variability contributions of $N_{\rm d}$ to albedo variability are somewhat small compared with variations in other cloud parameters, emphasizing the challenge that we face in detecting relatively small aerosol indirect effects on albedo above the meteorological noise.

It is interesting that although the mean (Fig. 1.1c) and variance (not shown) of $N_{\rm d}$ are high near the coast, the $N_{\rm d}$ variance contribution to albedo variance is fairly weak. This is partially due to the 1/3 power dependence of albedo on $N_{\rm d}$, but is also indicative that even large excursions in cloud droplet concentration can be overwhelmed by the variations in cloud liquid water path and cloud cover that also occur in the coastally influenced region. We should note that nonlinear and time lagged relationships between $N_{\rm d}$ and the other cloud variables involved are not captured in this analysis, so it is possible the full impact of high droplet concentrations on the albedo is not realized locally. For example, if a

Table 2.1: Fractional contributions to albedo spatial variance (2000–2008 time series). The mean, and the 90th and 10th percentiles of the distribution of daily contributions to spatial variance from each variable are shown. The L_p and N_d spatial variance contributions to albedo variance are computed by multiplying their contributions to τ spatial variance by the contribution of α_cld to albedo spatial variance.

	f_c	Cov(f_c, α_cld)	α_cld	L_p	N_d
90%	0.52	0.31	0.23	0.16	0.079
Mean	0.43	0.25	0.19	0.11	0.047
10%	0.36	0.19	0.15	0.076	0.021

parcel of air experiences an injection of aerosols and forms cloud, then advects, this analysis will not capture how changes in N_d in one location affect the albedo further downwind, after the aerosol has had time to affect the macrophysical cloud fields. Also, large scale meteorological influences known to play a role in cloud variability (e.g. stability, temperature advection, winds, and subsidence associated with the subtropical high) could simultaneously influence both cloud macrophysical and cloud microphysical properties. It is thus clear that investigation of the meteorological influence is necessary.

Meteorological influence on dominant modes of cloud variability

We apply empirical orthogonal analysis (EOF) analysis directly to the cloud variables (over a subdomain of the maximal mean cloud cover, 10–30° S, 70–90° W, to capture stratocumulus variability) and find dominant patterns of cloud variability qualitatively similar to the composite lagged differences of cloud variables on the dominant mode of variability in SLP (which represents the strength of the subtropical high, see George and Wood, 2010). Maximal positive anomalies in f_c and albedo associated with their repsective dominant modes of variability are seen in the region of peak cloud cover, and maximal anomalies in N_d are near the coast. The first principal components (PC1) of albedo, f_c, and N_d have peak power in periods near 10 days, consistent with the peak power in SLP (George and

Table 2.2: Ratio of the time mean of the spatial variance of each variable at a $1 \times 1^\circ$ grid resolution compared with that using a $2 \times 2^\circ$ grid resolution.

L_p	α_cld	N_d	α	f_c	z_i
1.60	1.46	1.27	1.23	1.22	1.09

Wood, 2010). Consistently, the PC1's of albedo, f_c, and N_d correlate significantly (99% confidence level) with the 3 day lagged SLP PC1 with maximum correlation coefficients of 0.2–0.3. The correlation coefficient between SLP PC2 and either albedo PC1 or f_c PC1 is in the range 0.3-0.4, and the correlation coefficient between SLP PC2 and N_d PC1 is approximately 0.5. This indicates that SLP PC2 is important for cloud variability despite explaining only 20% of SLP variability. This evidence helps to confirm that the subtropical high is an important driver of the dominant modes of large-scale variability of the cloud parameters, especially the cloud droplet concentration. In addition, the PC1's of albedo, f_c, and N_d correlate strongly with each other (correlation coefficients ranging from 0.6 to 0.9), indicating that these dominant modes of cloud variability likely reflect similar physical mechanisms due to large scale meteorological influence.

The first EOF/PCs of cloud parameters tend to explain only 10–30% of the variance in these parameters because the cloud data both is higher resolution and has higher spatial variability at small scales than SLP. The latter effectively constitutes a source of small-scale noise in our analysis that is likely to be uncorrelated with the large scale influences, and is particularly acute for cloud liquid water path (Table 2.2). SLP is clearly not the only controlling variable for stratocumulus clouds, and other meteorological processes, many of which may be independent of SLP changes, may play a role in controlling clouds. However, no single meteorological predictor was found to be better connected to the cloud variability than SLP. We cannot distinguish between meteorological forcing and aerosol indirect effects using SLP alone.

Liquid water path complicates attempts at simple physical interpretation of findings. Of

the parameters considered, L_p is the most variable on spatial scales comparable with the data resolution. Liquid water path shows the greatest loss of variance when averaged over 2×2° compared with the standard 1×1° (Table 2.2), has the smallest amount of variance explained by its first EOF/PC (∼9%), and has the weakest lagged signal composited on other PC1s. The power spectra of the L_p PC1 peaks at period of 6-8 days while the other variable's PC1s peak closer to 10 day periods (not shown). Liquid water path variability dominates α_{cld} variability in time (Fig. 2.3a) and space (as seen by the ratio of α_{cld} spatial variance at higher versus lower resolutions, Table 2.2), and thus α_{cld} also deviates from the behaviors of the relationship between SLP and cloud variables albedo, f_c, and N_d. The small-scale L_p variability is likely more strongly influenced by mesoscale cellular convection (Wood and Hartmann 2006) than are the other cloud variables. We note that this small-scale variability adds an additional complication to the separation of meteorological and aerosol effects.

2.4 Discussion and MODIS study conclusions

We have found little evidence for microphysical variability being a dominant contributor to albedo variability, even though the values of N_d above the marine background levels have the potential to alter the mean albedo substantially (Fig. 2.1). What then, is the outlook for the use of observations to help constrain the magnitude of aerosol indirect effects?

Clearly, it would appear that a priority must be to focus efforts on developing a better understanding of the meteorological factors controlling low cloud macrophysics and corresponding aerosol variability. Breaking the problem down into controls on cloud fraction, liquid water path and droplet concentration, may offer clues regarding the key physical processes. While large scale meteorological variables (e.g. the strength of the subtropical high, or its location) may be significant modulators of low cloud properties, we also know that there are mesoscale processes at work, particularly in the coastal zones, that are playing a significant role as well. Coastal synoptic features, such as coastal lows (Garreaud et al., 2002, Garreaud and Rutllant, 2003) and coastal jet episodes (Garreaud and Munoz, 2005) can change the cloud properties near the coast and their legacy in cloud properties can advect northwestward with the mean flow. While we encountered an index that encapsu-

lates events on shorter time and space scales than simple variability in the strength of the subtropical high, some of the cloud development may take place somewhat independently of large scale synoptic forcing. Gaining better conceptual and quantitative understanding of how these mesoscale systems influence cloudiness is important.

It will be also extremely important to understand the mechanisms by which meteorological variability helps drive aerosol variability. Here again, there may be feedbacks associated with cloud processing and coalescence scavenging that would lead to correlations between aerosol/cloud microphysics with meteorology that may be occurring through the meteorological control on cloud macrophysics.

We explore contributions to the subseasonal temporal and spatial variability of albedo over the southeast Pacific and find that cloud microphysics does not contribute more than 10% to this albedo variance. Albedo variance is dominated by macrophysics and the covariation between macrophysical parameters of cloud cover and liquid water path, and these features may be masking or suppressing microphysical impacts.

Our results provide several constraints for model evaluation based on subseasonal variability, and hypothesis that may be testable with regional models. The nature of the correlation of cloud microphysics with the macrophysical variables is one simple constraint beyond the mean state. Capturing the high spatial and temporal variability of L_{p} will be important for correctly representing and identifying feedback processes. In addition, models should be able to accurately represent the pattern and magnitude of the fraction of albedo variance explained by all the variables seen here. It would be useful to examine patterns of cloud variable composites on the large scale meteorological indices presented here. If a model could reproduce the patterns related to subseasonal variability of the system together with the mean states, then this would increase our confidence in the use of the model to quantify aerosol indirect effects.

Chapter 3

WRF-CHEM SPECIFICATION, EVALUATION AND SENSITIVITY

We use the Weather Research and Forecasting (WRF) model, a regional weather model, with interactive chemistry (WRF-Chem) because it is suited to a regional scale study and simulates most of the chemical, thermodynamic, and aerosol-related processes relevant over the SEP for our purposes. It includes online chemistry, as well as interactions between clouds, aerosols, turbulent mixing, and radiation, and is thus useful to this problem that involves the intersection of aerosol and meteorological processes.

3.1 Model configuration

We run the WRF-Chem version 3.2 (Grell et al., 2005; Fast et al., 2006) over an outer domain spanning 0-50°S, 60-100°W at $0.5 \times 0.5°$ horizontal resolution with 27 vertical levels, 10-12 of which are typically in the MBL, from 15 October to 16 November 2008 following nine days of spin-up. The spin-up period is sufficient to minimize the impact of chemical initial conditions due to species' lifetime. To accurately simulate the near-mountain flow and associated transport processes, we show results primarily from a nested, higher resolution domain spanning 3-40°S, 65-95°W, at $0.125 \times 0.125°$ resolution. For the outer domain, NCEP $1 \times 1°$ final analysis (FNL) winds, pressure, thermal and moisture fields at 6 hourly time resolution provide the meteorological boundary conditions. Chemical boundary and initial conditions come from the Model for OZone and Related chemical Tracers (MOZART-4; Emmons et al., 2010).

3.1.1 Chemical Emissions

An inventory compiled for VOCALS-REx described by Mena-Carrasco et al. (2010) provides point and area emissions from anthropogenic and volcanic sources. These combine data from the Comisin Nacional del Medio Ambiente (CONAMA) 2008 point source Chilean inventory,

estimated municipal mobile and residential inventories, EDGAR FT 2000 gaseous inventory (Olivier and Berdowski, 2001) with a current black carbon and organic carbon inventory (Bond et al., 2004), and analysis of OMI SO_2 PBL retrievals for SO_2 emissions outside of Chile. Point sources assume a static distribution that accounts for plume rise, and resulting estimates are included in the emissions inventory. Lima (12°S, 77°W) emissions have been reduced by a factor of 100 because in the simulation they cause excessive column SO_2 at Lima that was not observed by the Ozone Monitoring Instrument in 2004-2005 (Carn et al., 2007) and excessively high N_d in the northern part of the domain not present in MODIS retrievals. No biogenic or fire emissions are included in the simulations. WRF-Chem's online wind-blown dust emissions are excluded from the simulations because they are much larger than MOZART-4 dust emissions in this region and in any case do not affect CCN concentrations. Sea spray emissions are computed following Gong et al. (1997), and do not include organic components, which are small during the VOCALS campaign (Shank et al., 2012). The model does not include emissions of anthropogenic aerosol particles, but rather relies on nucleation and aerosol growth processes from gas phase emissions.

3.1.2 Physics

The physics and dynamics of the model are calculated using the Advanced Research WRF (ARW) dynamic solver. The dynamical equations used are nonhydrostatic, Eulerian and fully compressible. A constant 10 hPa pressure surface acts as the model top and vertical levels under this are defined by a terrain following hydrostatic pressure vertical coordinate. We use a timestep of 3 minutes, and a third-order Runge-Kutta scheme integrates the model over time. We run the model in parallel using a distributed memory computer cluster, which drastically improves computing time. The RRTM longwave radiation scheme, the Goddard shortwave radiation (Chou et al., 1998), the Grell-3D ensemble cumulus scheme, the Monin-Obukhov surface scheme, and the NOAH land surface model comprise other chosen options. Based on code from Xin-Zhong Liang at the University of Maryland we implement the University of Washington PBL scheme (UWPBL; Bretherton and Park, 2009) designed for the Community Atmosphere Model (CAM) to improve representation of stratocumulus in

coarse resolution models.

3.1.3 Chemistry

Chemical reactions are represented via the Regional Acid Deposition Model version 2 (RADM2; Stockwell et al., 1990; Chang et al., 1990), which employs the Quasi-Steady State Approximation method for 38 predicted, 3 constant, and 22 diagnosed species. This choice is a compromise between resolving chemical detail and restricting computing requirements. It includes aqueous phase chemistry (Fahey and Pandis, 2001) that is coupled to the microphysics and aerosol schemes. Represented are 14 stable inorganic species, 4 reactive intermediates and the abundant stable species O_2, N and H_2O. It also includes 26 organic stable species and 16 peroxy radicals, which are treated using a reactivity aggregated molecular approach to reduce complexity (aggregation factors from Middleton et al., 1990). Species of similar reactivity are treated in bulk. Gas phase and heterogeneous reactions are included, as well as some aqueous reactions, which is necessary for appropriate sulfur aerosol precursor and aerosol processing.

The oceanic emissions of DMS is a major source of natural SO_2 and plays an important role in setting cloud properties and the magnitude an anthropogenic SO2 perturbation makes on a cloud (Yang et al., 2011). Because DMS is not included in the RADM2 mechanism, we have added a uniform ocean surface DMS concentration of 2.8 nML^{-1} with a parameterized sea-air flux based on Nightingale et al. (2000) dependent on wind speed as described in the VOCA Modeling Experiment Specification[1], and we have added reactions of DMS with OH and NO_3 radicals to form SO_2

3.1.4 Aerosols

The MADE/SORGAM modal aerosol option (Ackermann et al., 1998; Schell et al., 2001) defines aerosol properties and behavior, and tracks three lognormal size modes representing the Aitken($\sim$0.01-0.1 μm), accumulation($\sim$0.1-1 μm) and coarse($>$ 1 μm) modes of aerosols. The total number of particles in each mode and the mass of each chemical compound for

[1]Available at *http://www.atmos.washington.edu/$\sim$mwyant/vocals/model/VOCA_Model_Spec.htm*

both interstitial and in-cloud aerosol are tracked as prognostic variables. The geometric mean diameter of each mode is not independently tracked, but rather can be computed from the mode number concentration and species mass concentrations. The distribution geometric standard deviation is fixed. Processes represented also include gas and heterogeneous chemistry, gas-particle partitioning, coagulation, cloud and ice-nucleation, dry and wet deposition. However, in WRF-Chem dry deposition tends to overestimate the loss of some species (Kazil et al. 2011), and since over the SEP the dry deposition is small and minimally contributes to the sulfur budget (Yang et al. 2011; Wood et al., 2012), we neglect it in our simulations. Nucleation is applied via Kulmala et al. (1998), computing homogenous nucleation in a sulfuric acid water system. Species output include SO_4, Na, Cl, NO_3, NH_4, elemental carbon, and lumped organic quantities encompassing primary organic aerosols from aromatics, and secondary organic aerosols from aromatics, alkanes, and alkenes.

3.1.5 Aerosol Indirect Effects

The first and second aerosol indirect effects, as well as the direct and semi-direct effects are represented through interactions between aerosols, radiation, and clouds (Fast et al., 2006; Gustafson et al., 2007; Chapman et al., 2009). In the VOCALS region there is little black carbon thus its direct and semi-direct effects are small in our region of study (Shank et al., 2012). The first AIE is implemented through a direct link of droplet concentration to the Goddard shortwave radiation scheme. The Lin microphysics parameterization (Gustafson et al., 2007; Chapman et al., 2009) is used, and has been modified to include prognostic cloud droplet number (Liu et al., 2005) that impacts the autoconversion rate and thus leads to 2nd AIEs. Aerosol particles activate to cloud droplets using the parameterization of Abdul-Razzak and Ghan (2000), based on critical supersaturation, which is diagnosed used the grid-scale vertical velocity field and the parameterized subgrid turbulent velocity. We modified the cloud droplet activation code to use the UWPBL turbulent kinetic energy (TKE) output following Morrison and Pinto (2005) rather than the eddy diffusivity of heat to compute subgrid vertical velocity variance, as was done in CAM (Gettelman et al., 2010). A Gaussian distribution of updraft speeds is used for the calculation of activated fraction

rather than a single updraft speed to avoid assuming the entire model layer has the same vertical velocity with no deviation due to local turbulence. Activation is predicted for each aerosol mode, and within each mode particles are assumed to be internally mixed.

The cloud droplet number affects the autoconversion rate (the Liu et al. (2005) autoconversion is used) and thus precipitation is altered by aerosol impacts. This in turn affects aerosol properties through changes in wet scavenging, the dominant aerosol loss mechanism in the SEP (Yang et al., 2011). Specifically wet scavenging removes both in-cloud aerosols and interstitial aerosols. Evaporation of cloud droplets releases aerosols back into the interstitial phase, but this process is not mirrored in the model precipitation. Rain that evaporates before reaching the surface does not renew the aerosol mass/number. This is not important for aerosol number but does affect aerosol mass.

3.1.6 Main simulations

For the purposes of quantifying anthropogenic AIEs we compare two main simulations. The first simulation 'Anth', which we use as our baseline simulation, has all the aforementioned emissions. A second labeled 'NoAnth' has no anthropogenic emissions and a third 'NoDMS' has all emissions other than DMS. Additional simulations used for sensitivity studies are described in this chapter and in section 4.4.6.

3.2 Model development

We implemented and experimented with several changes to the WRF-Chem model system to optimize the SEP stratocumulus representation. Although we mention some of these above, this list distinguishes the model development carried out as part of this thesis work from parameterization choices.

- Incorporated UWPBL scheme into current WRF-Chem system. Connected input and output variables with model system and extensively tested for correct implementation and units.

- Changed WRF-Chem activation code to compute the tubulent vertical velocity as $\sqrt{\frac{2}{3}TKE}$, where TKE is the turbulent kinetic energy output from the UWPBL scheme

instead of the eddy diffusivity for heat divided by the depth of the model layer. The latter is a function of the TKE but is likely implemented simply because most PBL parameterizations provide the eddy diffusivity for heat, but not all provide explicit output of TKE.

- Altered MOZART chemical boundary/initial conditions to exclude sulfuric acid, because combined with the sulphate aerosol boundary conditions this caused double counting of input of sulfur species at the boundaries.

- Removed 'unspeciated PM2.5' from MOZART boundary/initial conditions because this category led to unrealistically large N_d has no direct corollary in WRF-Chem. The closest analogy is the species that represents dust, but unspeciated PM2.5 is not just dust, but rather a combination of unidentified species not scientifically justifiable.

- Wrote a program to regrid emissions inventory and translate given emissions species to WRF-Chem chemistry and aerosol variables.

- Added DMS and reactions with OH and NO_3 to form SO_2 to the RADM2 chemical model.

- Recomputed CCN to improve the diagnostic estimate provided in the WRF-Chem output. See section 3.2.1 for details.

- Explored implementation options of including UW shallow cumulus scheme, but deemed it unessential for the scientific questions posed in this study. Interfacing it with the chemistry model would be particularly challenging, because the cumulus-radiation feedback that allows the radiation and photolysis schemes to recognize parameterized clouds is only permitted in WRF-Chem for the Grell cumulus schemes. Without this feedback surface temperatures are too warm and there is a low bias in the SO_2 to SO_4 conversion. We use the Grell cumulus scheme.

- Experimented with turbulent mountain stress parameter in PBL scheme to improve behavior of scheme over steep topography. This work was not found to impact our results.

- Translated WRF-Chem output to VOCA experiment to contribute to the model intercomparison study by Matthew Wyant at the University of Washington.

3.2.1 Diagnostic CCN re-calculation

We determined that the cloud condensation nuclei (CCN) concentration, a diagnostic field in WRF-Chem, is not computed optimally and includes a low bias in the SORGAM modal aerosol module. It is a diagnostic quantity and does not impact other model properties, but needs to be corrected for comparisons with observations. The model computes CCN using the Abdul-Razzak and Ghan (2001) formulation, but incorrectly assumes the modal geometric mean diameters are the the mode minimums (0.01, 0.07, and 1 μm for Aitken, accumulation and coarse modes respectively), the sizes used to initialize the modes before aerosol processes allow them to grow to more typical sizes (around 0.03, 0.15, 5 μm). A log-normal aerosol particle size distribution is assumed for each mode. The fraction of particles that activate in a single mode is computed as :

$$\frac{N_{activated}}{N_{particles}} = 1/2 * [1 - \mathrm{erf}(u)]s \tag{3.1}$$

where

$$u = \frac{\ln(\frac{S_m}{S_{max}})}{3\sqrt{2}\ln(\sigma)} \tag{3.2}$$

and σ is the standard deviation of the aerosol size distribution in the mode, $N_{particles}$ is the number of aerosols in a mode, and $N_{activated}$ is the number of particles that will activate. S_m is the critical supersaturation for a particle with the geometric mean radius of the aerosol size distribution and S_{max} is the critical supersaturation for the smallest particle activated. To compute the number of particles that would activate at a particular supersaturation s (CCN), S_{max} is prescribed as s and S_m is computed from the aerosol mode geometric mean radius a_m as

$$S_m = \frac{2}{B}(\frac{A}{3a_m})^{3/2} \tag{3.3}$$

where A is a coefficient that takes into account the droplet surface tension(curvature effect) and B takes into account hygropicity (solute effect) associated with Kohler curve theory.

In the WRF-Chem code S_m is computed for each aerosol mode assuming a constant minimum geometric mean mode size rather than deriving this value. Although the mode mean size is not explicitly recorded in the model, it can be computed using the total mode number concentration and an aggregate of the individual aerosol mass concentrations within each mode using the assumed particle density of each species. The composition of aerosol mass within an aerosol mode is also used to compute a volume weighted hygroscopicity already, and can be modified to identify the effective geometic mode mean as well.

We compare several REx mean quantities in section 3.3, but it is relevant to note here that the model underestimates the observed VOCALS REx mean CCN in the MBL and FT. Applying the corrected formulation for CCN increases the REx mean CCN closer toward the observations, particularly in the more polluted regions near the coast, and on average increases the CCN estimate at 0.5% supersaturation over the SEP by about 60%. There is still low bias in condensation nuclei due to a deficit of small particles in the model and this will be discussed in the next section.

3.3 Model evaluation during REx

Other studies using similar versions of WRF-Chem to simulate the VOCALS-REx period have been able to reproduce, with some fidelity, the key cloud and chemical features, including 20°S time-mean longitudinal gradients of sulfate, aerosol concentration and N_{d} (Yang et al., 2011b; Saide et al., 2012). Although our simulations employ slightly different parameterization options and resolution, it also reasonably reproduces REx mean conditions. The gradient of REx mean N_{d} along 20°S agrees well with satellite and aircraft data (Fig. 3.1a) even though the magnitude is underestimated by 10-30%. L_{p} is strongly underestimated – this is a common problem in many models simulating the SEP (Wyant et al., 2010) that we have not resolved in this work. Both Saide et al. (2012) and Yang et al. (2011) underpredict this field as well for clouds of the SEP. It appears to be a more systemic problem than particular cloud parameterization choices.

We compare chemical and aerosol quantities in the marine boundary layer (MBL) and

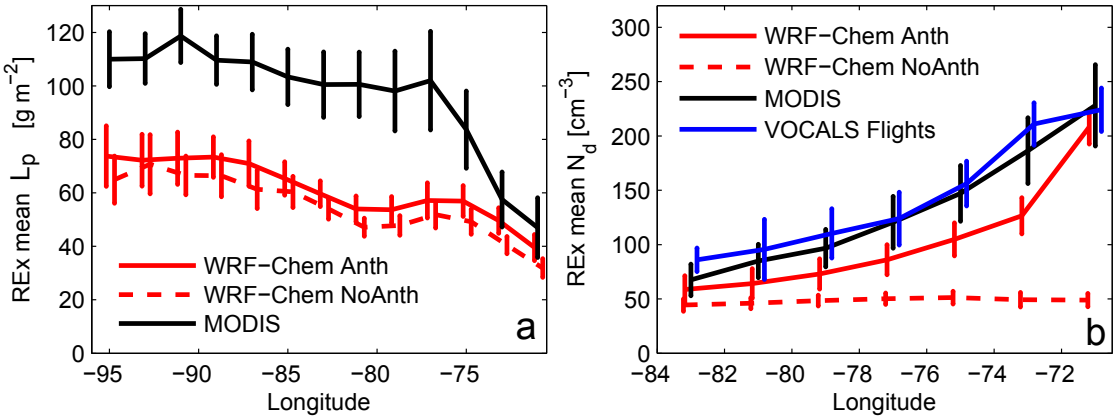

Figure 3.1: VOCALS-REx 19-21°S time mean cloud properties from MODIS retrievals (black), VOCALS flight data (blue) and WRF-Chem model output (red; at 15 UTC to compare with MODIS) for Anth (solid) and NoAnth (dashed) simulations in 2 degree longitude bins for (a) L_{p} and (b) N_{d}. Error bars show the 95% confidence interval of the standard error of the mean.

free troposphere (FT) with REx-mean VOCALS flights along 20°S reported in (Allen et al., 2011). The model inversion height is determined as the minimum model level in which the relative humidity is smaller that 40%. If an inversion level is not identified within 4 km from the surface, the model level above the highest level with a negative rate change in liquid water content with height is chosen. If this fails, the inversion height is considered undefined, which does not occur often in the stratocumulus region. MBL quantities are computed 2 model levels below the inversion and FT quantities 2 levels above. These levels fall roughly near the height ranges specified in Allen et al. (2011). Like the Yang et al. (2011b) and Saide et al. (2012) simulations, the offshore MBL SO_2 concentrations are on the low end of VOCALS observations, but reasonably capture the longitudinal gradient (Fig. 3.2a,c). Very closer to shore FT SO_2 exceeds observations. Sulfate aerosol mass concentrations are similar to observations offshore both above and below the inversion 3.2b,d), although this sulfur species concentration is also too large between 70-73°W in the FT, whereas the MBL SO_4 mass fits observations quite well. A high SO_2 bias near-shore and a low bias offshore may indicate chemical and aerosol offshore transport is not quite strong enough in the REx mean, or that emissions from nearby local sources (such as the Ilo smelter at 17.6°S, 71.3°W)

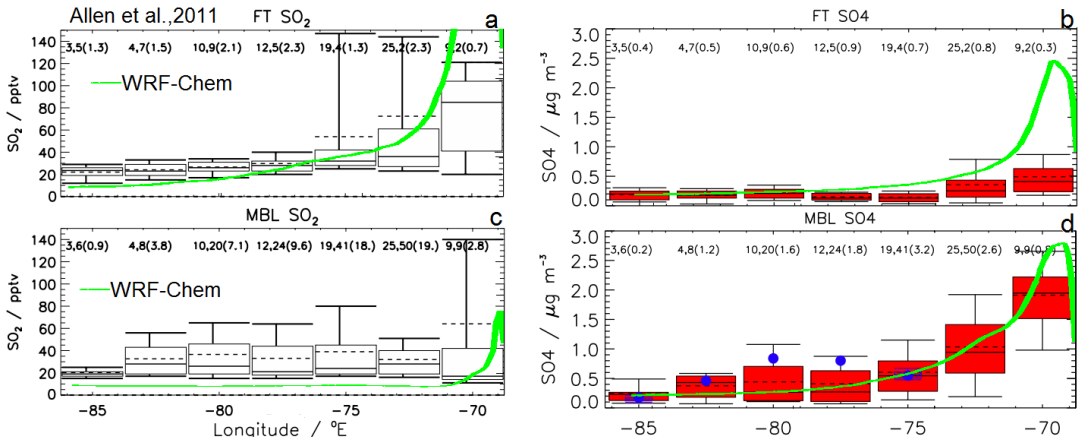

Figure 3.2: Figure from Allen et al. (2011) showing VOCALS flight REx mean observations of SO_2 mixing ratio and SO_4 mass concentration in 2.5-degree longitude zones in the free troposphere and marine boundary layer ((a),(b)1700-3200 m altitude and (c),(d) below 1200 m altitude). Numbers before the comma in each longitude zone indicate number of flights contributing to each statistic, followed by the number of straight and level runs, with the total sampling time in decimal hours in parentheses. Boxes indicate quartiles of data. Blue circles indicate median Ron Brown data. Superimposed on this figure is REx mean WRF-Chem output (green).

are too large. The Ilo smelter was not running during much of the VOCALS field campaign, and the emission dataset includes a correction for this, though it is posible these emissions are still overestimated. Unlike Saide et al. (2012) we do not tune the background SO_2 in the FT to match VOCALS observations. While our offshore estimates of SO_2 are somewhat low, this may be partly due to that measured concentrations are near the minimum detectable concentrations for the instrumentation (personal corespondence, Robert Wood).

As in Saide et al. (2012), we find that Lin microphysics leads to a mean high precipitation bias (Fig. 3.3) along 20°S. Although the magnitudes are near the aircraft mean values, most of these flights occurred at nighttime and so the appropriate comparison is with the mean Cloudsat data. This contributes to the model's low L_{p} bias, and may partially explain the low bias in N_{d} and shorten the lifetime of aerosol species in the MBL.

Along 20°S, model CCN magnitudes are less than half that reported by the VOCALS observations in Allen et al. (2011; Fig. 3.4). This is a stark contrast from the reasonable

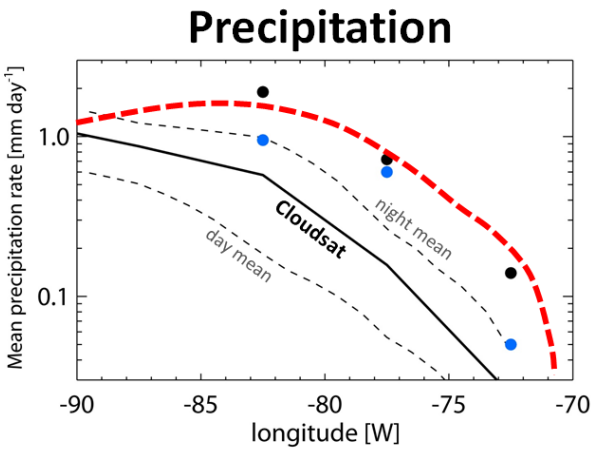

Figure 3.3: REx mean column maximum precipitation rate along 20°S for model (red dashed line), and VOCALS flight data using the Wyoming Cloud radar (black dots, courtesy of Dave Leon) and in-situ cloud probes (blue dots). CloudSat estimates using blended attentuation and Z-R methods is shown with the black line, with daytime and nighttime means in dashed black lines.

comparisons of other variables discussed thus far. As noted in the previous section the WRF-Chem diagnostic output needed to be corrected, but this does not resolve the entire difference between model and observations (Fig. 3.4). A deficit of small particles in the model may explain this discrepancy. With nucleation processes only simulating the water-sulfuric system, other small particles that grow into activatable sizes are missing from the model representation. The accumulation mode aerosol concentrations from the model compare well with VOCALS (Fig. 3.5), which are in the size range most expected to actually activate. This explains why the CCN is biased so low, yet the N_{d} and aerosol mass species are reproduced reasonably well with only small ($< 30\%$) biases. The missing small particles introduce a bias to our total diagnostic CCN, but do not appear essential to capturing the activation of particles reasonably well (i.e. N_{d} is reasonable) nor do they impact aerosol mass due to their size. Thus the model reasonably simulates the aerosol and cloud features we care most about for investigating AIEs.

To add confidence to the use of the UWPBL scheme, we also compare REx mean model turbulent vertical velocity to that recorded by VOCALS flights (not shown) and find the

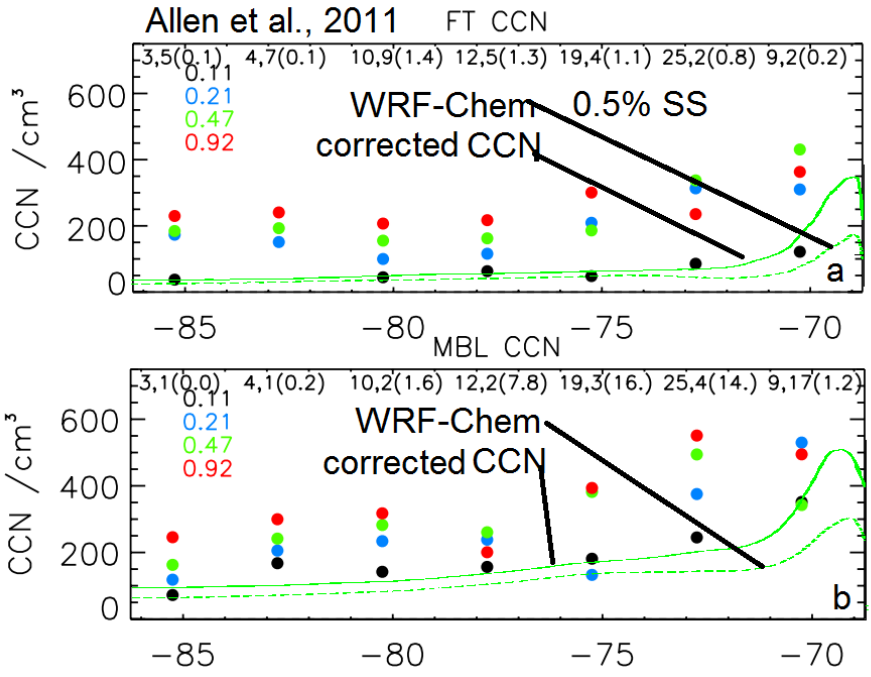

Figure 3.4: Figure from Allen et al. (2011) showing VOCALS flight REx mean observations of CCN number concentrations in 2.5-degree longitude zones between 1700-3200 m altitude (top) and below 1200 m altitude (bottom). Numbers before the comma in each longitude zone indicate number of flights contributing to each statistic, followed by the number of straight and level runs, with the total sampling time in decimal hours in parentheses. REx mean WRF-Chem CCN at 0.5% supersaturation (green) is superimposed on this figure. The lower curve is the WRF-Chem CCN output and the upper curve is the recomputed CCN considering the modal mean of aerosol size distributions.

model value falls within the quartiles of observations (∼0.3-0.6 $\mathrm{m\,s^{-1}}$). This confidence is enhanced when we compare results from the UWPBL scheme to the Yonsei University Scheme (YSU; Hong et al., 2006), which was suitable for Yang et al. (2011) but does a poor job at our coarser resolution runs. It is a 1st order nonlocal turbulence scheme with explicit treatment of entrainment processes. The bulk Richardson number is used to define the PBL top. The UWPBL scheme also includes explicit entrainment, has an advanced 2nd order closure scheme and is dsigned to represent stratocumulus, including a sharp capping inversion in a coarse resolution model. Figure 3.6 demonstrates that the mean (15-26 October shown here) N_d, f_c and L_p reproduce MODIS data with a magnitude

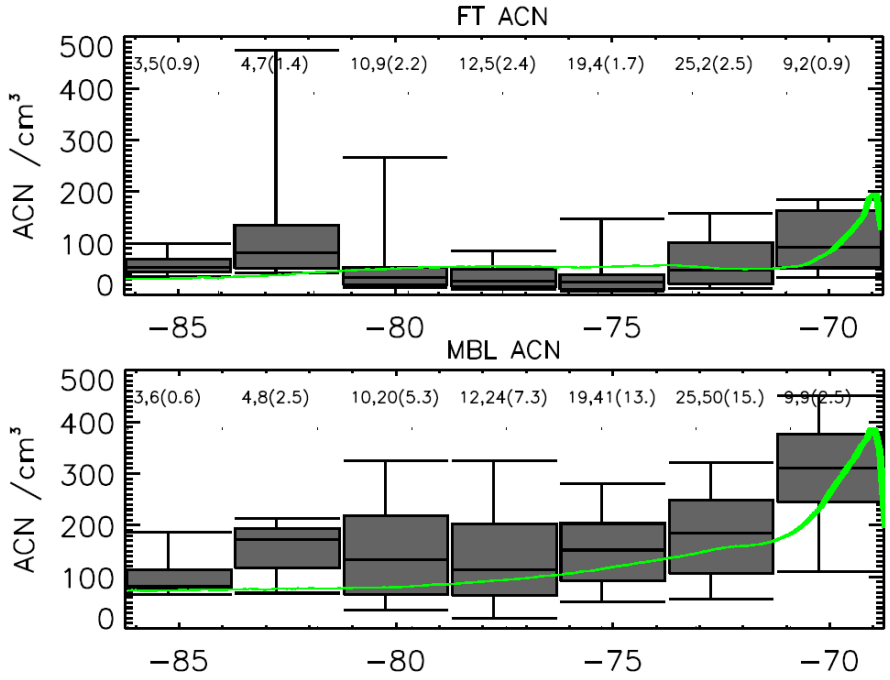

Figure 3.5: Figure from Allen et al. (2011) showing VOCALS flight REx mean observations of accumulation mode aerosol number concentrations (ACN) in 2.5-degree longitude zones between 1700-3200 m altitude (top) and below 1200 m altitude (bottom). Numbers before the comma in each longitude zone indicate number of flights contributing to each statistic, followed by the number of straight and level runs, with the total sampling time in decimal hours in parentheses. Boxes indicate quartiles of data. REx mean WRF-Chem accumulation mode aerosol concentration (green) is superimposed on this figure.

bias described earlier. The comparison with the YSU PBL scheme is markedly worse in all cloud variables and indicates our chosen set of parameterizations does well at reproducing mean cloud conditions.

To evaluate model inversion height, we use a once-daily estimate of the marine boundary layer (MBL) depth z_i derived using the difference between Reynolds sea surface temperature and cloud top temperature (using the MODIS Terra L3 data at $1\times1^\circ$ resolution). This employs the lapse rate formulation from Wood and Bretherton (2004), and makes the assumption that the top of the MBL is commensurate with the cloud top height, a good assumption for this region (Caldwell et al., 2005). Comparisons of this approach with ra-

diosonde estimates of cloud top height in the region (Zuidema et al., 2009) show that the instantaneous uncertainty is better than 300 m, consistent with error estimates from Wood and Bretherton (2004). Averaging over multiple days reduces this uncertainty.

A comparison of model, MODIS and VOCALS inversion height along 20°S (Fig. 3.7) demonstrates a reason the YSU performs so poorly – it produces a low inversion across the domain which suppresses cloud development. UWPBL also has a lower inversion height than the MODIS estimate and VOCALS data, but falls within the uncertainty of these quantities, so is not statistically significantly different from observations.

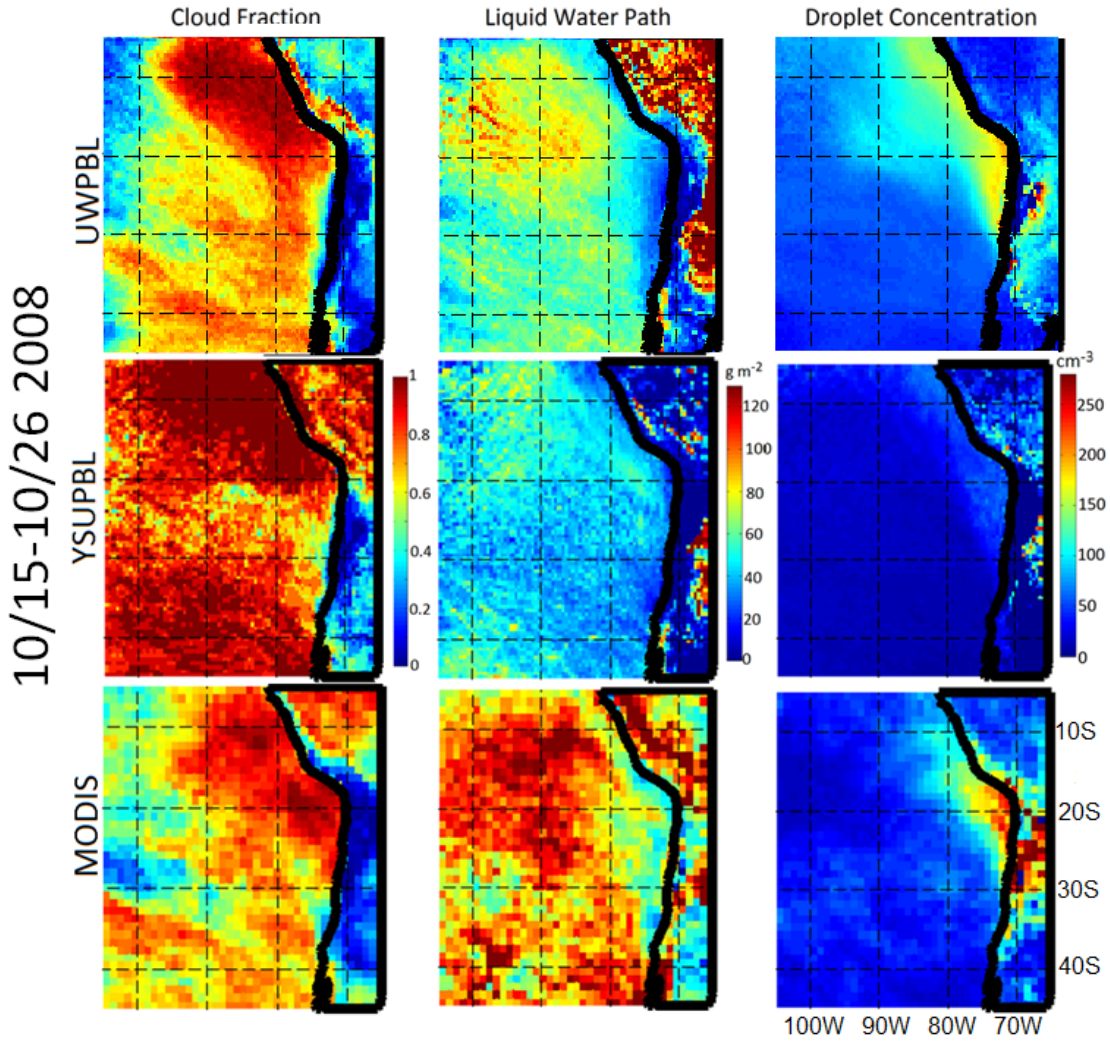

Figure 3.6: Mean 15-26 Oct, 2008 of cloud properties f_c, L_p, N_d in 0.5° resolution model using UWPBL scheme in the top row, YSU in the middle, compared to MODIS satellite data in the bottom row.

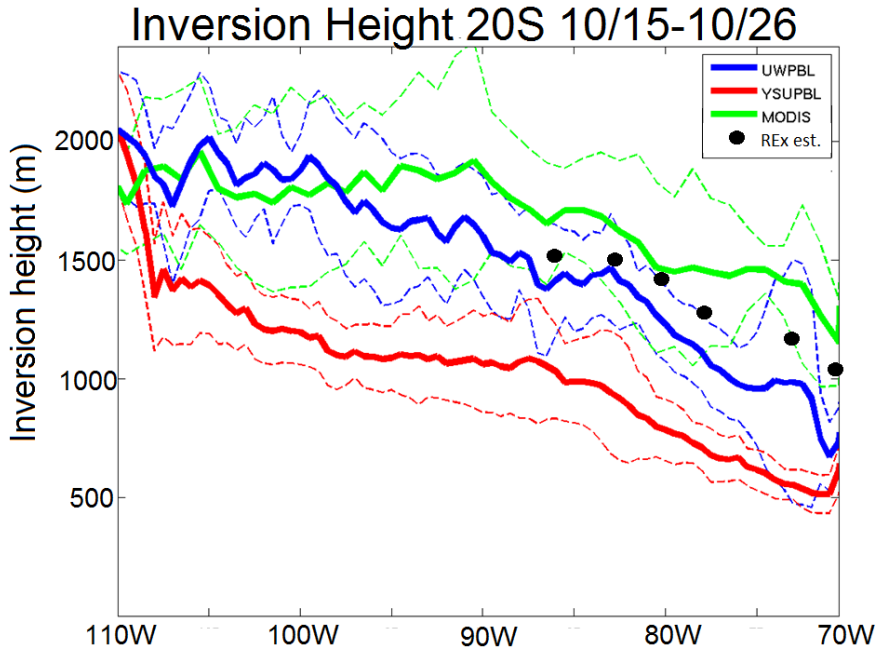

Figure 3.7: Mean inversion height over 15-26 Oct, 2008 from MODIS data (green), VOCALS REx estimates (black circles), and two different PBL schemes - UWPBL (blue) and YSU(red).

3.4 Additional Sensitivity studies

Through the course of this work we ran many simulations to test the impact of parameter choices on the simulation quality. It is worth noting that despite the suitability of the main model set-up, other parameterizations can produce wildly different and/or unrealistic SEP stratocumulus, as we noted in the previous section with the YSU PBL scheme. The use of chemistry modules has not been fully tested with all physical parameterizations and thus only specific combinations of choices at specific resolution ranges reproduce the main cloud features of the SEP. This challenge is not limited to WRF-Chem, as demonstrated by Wyant et al (2010). A few sensitivity studies, including a run with no DMS emissions, and various anthropogenic emissions scenarios are relevant to Chapter 4 and thus will be discussed there instead. An ensemble simulation is discussed in Chapter 5.

Here we show the impact of wet scavenging on the REx-mean cloud properties. There

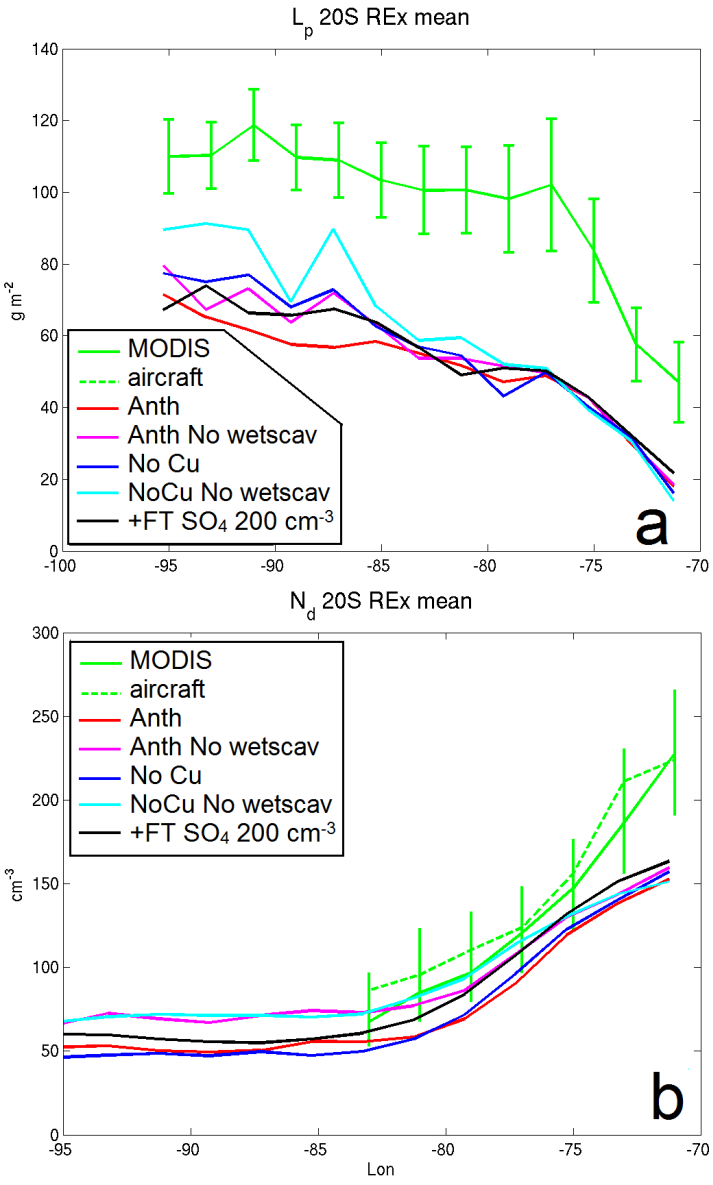

Figure 3.8: Binned REx mean 20°S (a) N_{d} and (b) L_{p} from observations (green) and WRF-Chem at 0.5° resolution for 4 simulations: Anth(red), Anth with wetscavenging flag turned off (magenta), Anth with cumulus scheme turned off (blue) and Anth without cumulus scheme wetscavenging flag turned off (cyan). Also shown is an experiment with an extra 200 cm^{-3} Aitken mode sulfate particles in the western free tropospheric boundary conditions (black).

is a WRF-Chem option that turns off wet scavenging in the chemistry module that allows precipitation but prevents aerosol loss. However, the Grell cumulus scheme also incorporates some wet scavenging of species, so in our simulation the wet scavenging flag does not remove this aerosol sink completely. But, as described earlier in this chapter, turning off the cumulus scheme can have consequences for radiation, photolysis and SO_2 to SO_4 conversion rates. Yang et al. (2011) and Saide et al. (2012) both do not use a cumulus scheme, but they also use higher resolution and they do not elaborate on the known consequences of their choice. Close to the coast the cumulus scheme has little impact, but can influence further offshore in the domain we how. Figure 3.8 demonstrates that the cumulus scheme has minimal impact on N_{d} but that the impact on L_{p} is as strong as turning off the wet scavenging flag. Note the simulations shown are from the $0.5 \times 0.5^{\circ}$ resolution, in which the Anth simulation N_{d} gradient does not compare to observations as well as the $0.125 \times 0.125^{\circ}$ due to the impact of resolution over the Andes on offshore transport. Turning off both cumulus and wet scavenging leads to strange longitudinal variability in L_{p} between 85-95°W that may indicate no cumulus scheme is inappropriate for this region. For N_{d} both processes off is no different than just turning off wet scavenging for most longitudes, except between 77-85°W where both processes off leads to exceptionally good agreement with MODIS. Sadie et al. (2012) hypothesizes that scavenging is too strong in the model and that the optimal representation is in between simulations with wet scavenging on and off.

Turning off wet scavenging, either with the flag, the cumulus scheme, or both increases the remote ocean N_{d} and L_{p} towards observations, but has little impact close to shore because precipitation and cumulus scheme processes are not as relevant there (Fig. 3.3). This is helpful for remote ocean N_{d}, but does not resolve the L_{p} low bias. Additionally the effect of 200 cm^{-3} free troposheric Aitken mode sulfate particles added to the boundary conditions is to increase N_{d} by 5-15 cm^{-3} and L_{p} by less than 10 gm^{-2}, about half the magnitude of the wet scavenging effects. We do this to imitate the method of Saide et al. (2012) for obtaining improved free tropospheric estimates of sulfur species and aerosol concentrations. It is clear than that the REx-mean quantities are at least weakly sensitive to processes that affect aerosol concentrations and the concentrations of aerosols advecting in from the boundary conditions. However, none of these options dramatically changes the

estimates enough to change the nature of the gradients, but rather are simply interesting perturbations.

3.5 Controls on model albedo variability, validation

In addition to the mean state of cloud variables, to gain confidence in the model's representation of cloud variability, we refer back to the method derived in Chapter 2 for computing dominant controls on albedo variability. Although the REx period is too short for an extremely robust comparison between MODIS and WRF-Chem output, there is a reasonable correspondence between model and satellite derived controls on albedo variability over the REx period (Fig. FOVA). The spatial contrast between contributions of cloud fraction(f_c) and cloud albedo (α_c) and their covariance is captured by both Anth and NoAnth simulations. This indicates that anthropogenic aerosols do not impact the relationship between f_c and α_c with respect to their contribution to α variance. This is expected because the drop off in f_c variance near the coast is more demonstrative of the persistence of the stratocumulus deck over time than it is about microphysical impacts. Because the binary model f_c is at 14 km resolution and the MODIS binary f_c is at 1 km resolution, in addition to model biases, model f_c is missing variability in the 5-14 km range that is incorporated into the 1° MODIS product. This may explain some of the differences in magnitude and shape, but a longer simulation would need to be compared to determine how much of an impact this has.

The model contribution of $\mathscr{N}=N_d^{1/3}$, and $\mathscr{L} = L_p^{5/6}$ to optical depth (τ) variability (Fig. 3.10) demonstrates a good magnitude comparison with MODIS, though the region of enhanced $\mathscr{N}$ variability is offset by a few degrees northeast in the Anth simulation compared to MODIS. This Anth pattern of $\mathscr{N}$ contribution coincides more with the MODIS climatological mean, so this offset could be to monthly variability not captured by the model. The NoAnth simulation N contribution is largest along the Peruvian coast, presumably due to nearby volcanic emissions. Although the pattern of the contribution of covariance between $\mathscr{L}$ and $\mathscr{N}$ is highly variable, both simulations agree there are regions of positive and regions of negative correlations. The region of positive correlation north of 20°S coincides with the region of strongest positive 2nd AIE magnitudes, and is not present in MODIS. This may

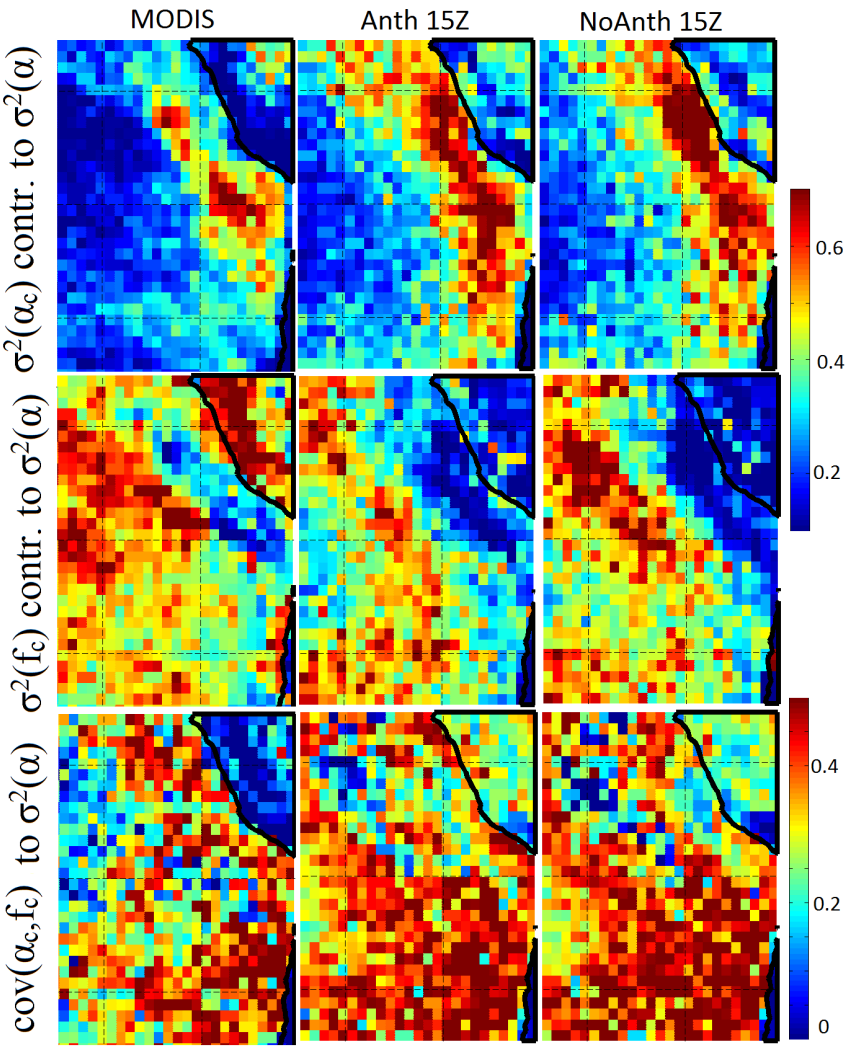

Figure 3.9: The contribution of time variability in f_c, α_c and their covariance on α variability over REx at 15 UTC from MODIS, and Anth and NoAnth WRF-Chem simulations.

indicate that the parameterized 2nd AIEs in the model are too strong in this region leading to large enhancements in $\mathcal{I}$ coinciding with $\mathcal{N}$ increases. Or, it is possible that 2nd AIEs not represented in the model offset this effect in observations. The weaker positive strip along the Peruvian coast in MODIS may be due to similar processes as those modeled in the region, but the model just represents the effect to strongly.

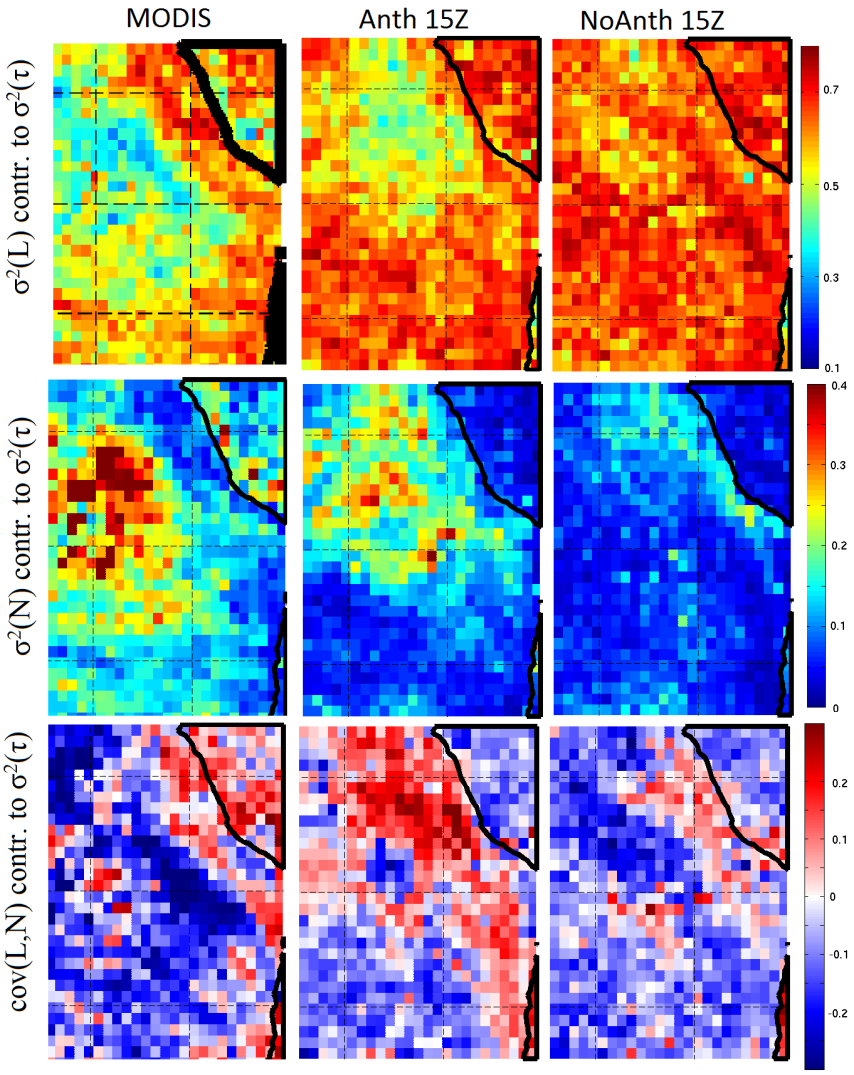

Figure 3.10: The contribution of time variability in $\mathcal{I}$, $\mathcal{N}$ and their covariance on τ variability over REx at 15 UTC from MODIS, and Anth and NoAnth WRF-Chem simulations.

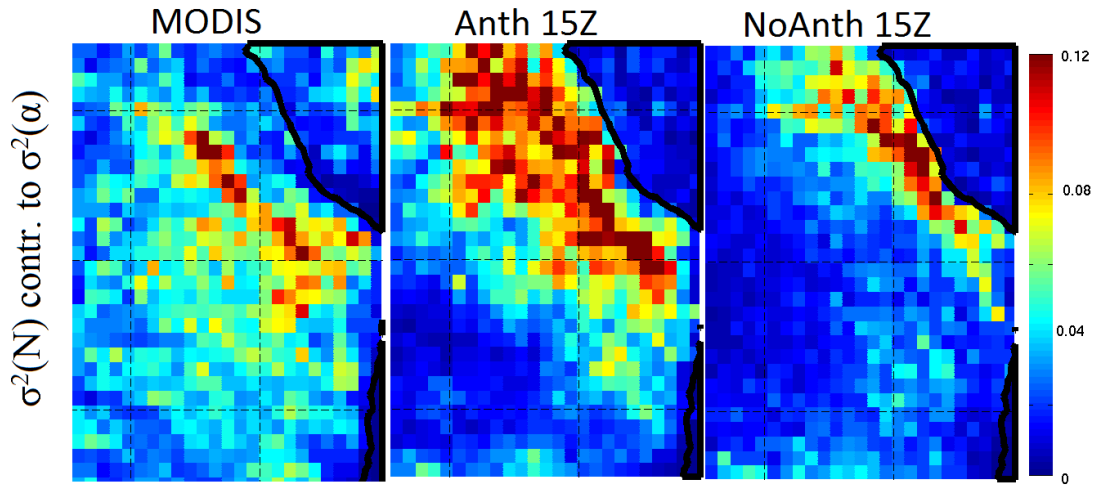

Figure 3.11: The contribution of time variability in $\mathscr{N}$ on α variability over REx at 15 UTC from MODIS, and Anth and NoAnth WRF-Chem simulations.

Chapter 4

HOOKS

4.1 Hook introduction

Over the SEP, N_d estimates derived from MODIS satellite retrievals George and Wood (2010) show strong mean zonal gradients from the relatively 'pristine' MBL west of 80°W to high concentrations near to the Chilean coast (Fig. 4.1a). The increase east of 75°W is associated with anthropogenic aerosols transported by two pathways: direct advection in the MBL from coastal sources; episodic transport in the FT and entrainment into the MBL (Huneeus et al., 2006; Allen et al., 2011). Composites of MODIS N_d and derived reflected solar flux at the top of the atmosphere are constructed for those days when mean N_d in the domain 19-21°S, 82-86°W is more than 87 cm^{-3} (one standard deviation above the climatological mean). This box is chosen to sample the region where N_d contributes most to albedo variance (see Fig. 5 in George and Wood, 2010). Comparing these increased offshore N_d composites (Fig. 4.1b) with the mean state (Fig. 4.1a) reveals a shift in the pattern of N_d not only within the compositing box (which, by construction must occur) but over a broad region between the box and the coast. The hook-like shape of enhanced N_d extends southeastward from the compositing domain (Fig. 4.1b) and strongly enhances the albedo and the Twomey effect offshore (Fig. 4.1c vs. 4.1d). Around the compositing box, days with high N_d experience 25-40 Wm^{-2} larger reflected solar flux than on average and 10-20 Wm^{-2} (∼40-50%) of this is due to the Twomey effect. The remote composites therefore demonstrate important microphysically-driven albedo variability in an often pristine region. The non-Twomey component of the albedo increases may be caused by secondary AIE's and/or meteorological covariability with N_d. This motivates our need to investigate the reasons for strong N_d variability over the remote SEP.

Instantaneous images over consecutive days showing N_d from the GOES satellite (Section 4.2.1) during periods of elevated offshore N_d typically show a narrow band of high N_d

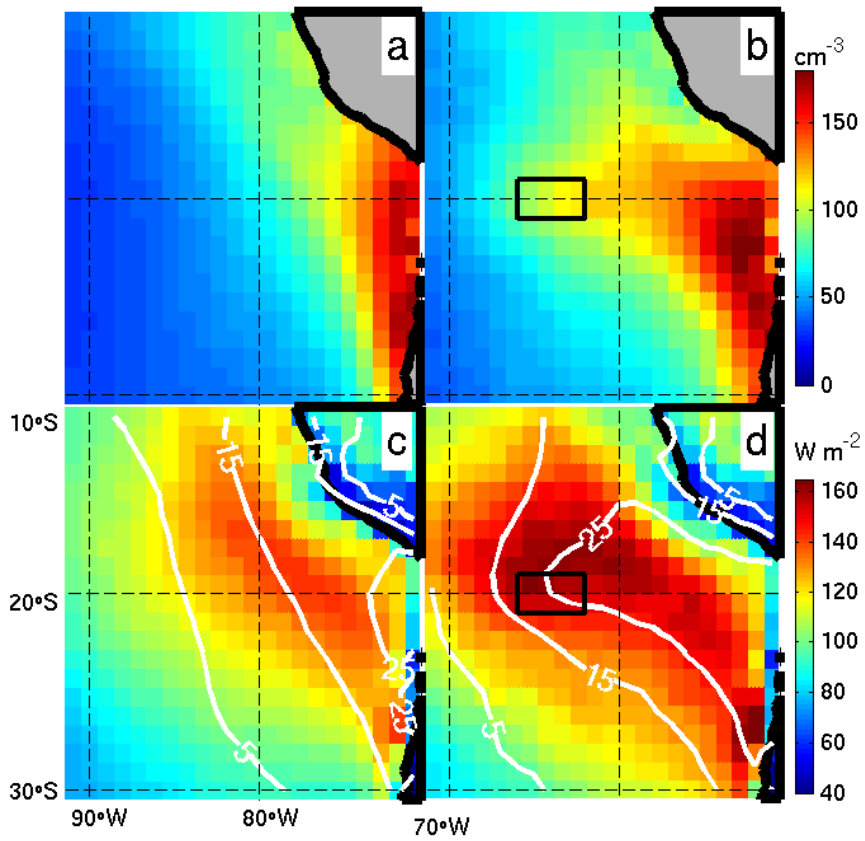

Figure 4.1: 2000-2008 MODIS time-mean cloud droplet concentration (N_d) from **(a)** all retrieved days and **(b)** days when N_d averaged over the domain 19-21°S, 82-86°W is larger than 87 cm^{-3} (time mean plus standard deviation). Shaded colors in **(c)** show the diurnal mean estimate of reflected solar flux at the top of the atmosphere. The white contour lines are the time mean of the difference between the reflected solar flux and the same flux computed using the typical pristine marine N_d (average time series of N_d in the domain 30-40°S, 90-100°W), which is an estimate of the Twomey effect. The contour numbers indicate Wm^{-2} of flux difference due to the increase in N_d above typical marine values. **(d)** is the same as **(c)**, but composite on the same days as **(b)**.

characterized by an east-west 'hook' of high N_d with maximum N_d in the range 150-350 cm^{-3} standing out against marine background values of ∼50 cm^{-3}. The example in Fig. 4.2 (17-20 October, 2008) occurred during the VAMOS Ocean-Cloud-Atmosphere-Land Study Regional Experiment (VOCALS-REx; Wood et al., 2011b) that took place 15 October - 16

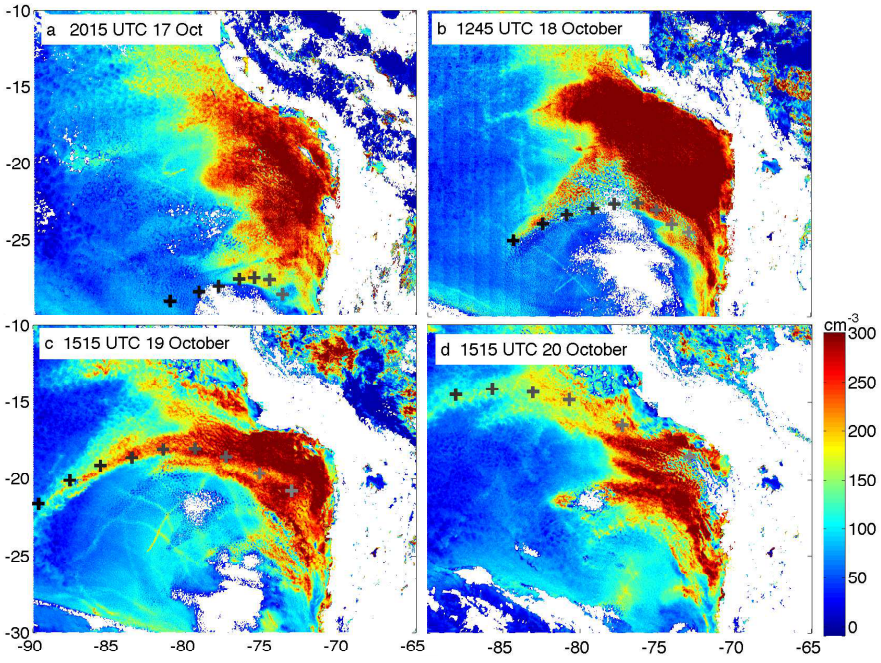

Figure 4.2: Observations of Hook1 N_d derived from GOES retrievals (Section 4.2.1) on **(a)** 17 October at 2015 UTC, **(b)** 18 October at 1245 UTC, **(c)** 19 October at 1515 UTC, and **(d)** 20 October at 1515 UTC. Markers (+) show points along ECMWF MBL 2D (at 950 hPa) forward and backward trajectories (see AppendixB) initialized at locations along the hook on 19 October at 15 UTC.

November, 2008. During REx, hooks that extended west of 80°W coincided with research flights at least 3 times (18 Oct, 2 Nov and 15 Nov), and we refer to these cases as Hooks 1, 2, and 3 respectively.

In this study we investigate the development and impact of hooks using aircraft data, satellite data and regional modeling. Section 4.2 investigates the evolution of Hook1 using trajectory analysis. We next use the Weather Research and Forecasting model with chemistry (WRF-Chem) to show that the simulated Hook1 formed predominantly by entrainment into the MBL of anthropogenic aerosols transported offshore from the Santiago region above the MBL, rather than by aerosol transport within the MBL or by other means. Chapter 3 detailed WRF-Chem simulations and compares them to satellite and aircraft observations and section 4.3 summarizes the evaluation useful for this chapter. Section 4.4

describes in detail cloud and chemical changes that occur during the development and decay of Hook1, identifies the meteorological conditions supporting the hook formation and discusses its impact on albedo. Section 4.5 considers Hook2 and Hook3 and compares them to Hook1. Conclusions follow in Section 4.6.

4.2 Observational investigation of hook CCN sources

4.2.1 Data

We consider VOCALS-REx observations from the NSF/NCAR C-130 and the UK BAe-146. On both platforms N_d was measured with a Cloud Droplet Probe. Measurements of CCN were made by the University of Wyoming instrument on the C-130, which consists of a static thermal-gradient chamber and optical detection system (Snider et al., 2006). We primarily consider measurements between 0.4-0.5% supersaturation to compare to model CCN at 0.5% supersaturation. DMS and SO_2 were measured at 1 Hz on the C-130 using an atmospheric pressure ionization mass spectrometer by Drexel University (Bandy et al., 2002; Thornton et al., 2002). More detailed instrument specifications can be found elsewhere (e.g., Allen et al., 2011; Wood et al., 2011a).

MODIS satellite retrievals of N_d are limited by the daily time resolution, so we also use Geostationary Operational Environmental Satellite (GOES) retrievals of LWP and effective radius provided by Dr. Patrick Minnis's research group at NASA Langley Laboratory (http://www-angler.larc.nasa.gov/) to compute N_d at 4 km horizontal resolution, 30 minute time resolution by the method of Bennartz (2007) with a corrected formulation for the vertical condensation rate (from Albrecht et al., 1990). While the N_d accuracy depends upon solar zenith angle, midday retrievals reasonably match VOCALS flight observations and MODIS estimates (Painemal et al., 2012).

European Centre for Medium Range Weather Forecasting (ECMWF) operational analyses on a $0.125 \times 0.125^\circ$ grid with 91 hybrid model levels at 6 hour time resolution are used to drive 3D and 2D trajectories (see Appendix B) presented here. 2D isobaric trajectories at a mid-MBL pressure of 950 hPa track satellite cloud features advecting with the MBL flow quite well, lending confidence in the use of trajectory analysis. We attribute the agreement

to the high quality of the ECMWF wind analysis (Bretherton et al., 2010) and the relatively weak vertical shear of winds within the MBL.

4.2.2 Hook1 observations

Of the three cases, Hook1 has the strongest anomalous N_{d} and extends the furthest west into the remote ocean, and is particularly striking on 19 Oct at 15 UTC (Fig. 4.2c). Isobaric two-dimensional forward and backward trajectories at 950 hPa based on ECMWF analyses initialized from points on the hook on 19 October at 15 UTC trace the hook advection quite well between 18-20 October (Fig. 4.2b-d). However, prior to this on 17 October (Fig. 4.2a) the three outermost trajectory points have $N_{\mathrm{d}} < 70 \ \ \mathrm{cm}^{-3}$, typical of pristine marine air, and all trajectory points have significantly lower N_{d} than on 19 Oct. Although accumulated trajectory errors could potentially contribute to this, it appears that the hook in N_{d} is not explained solely by advection of an aerosol-rich airmass from the coast within the MBL.

Entrainment of FT aerosols thus warrants investigation as a significant contributing hook source. Three-dimensional back trajectories using ECMWF analyses (Fig. 4.3) from points along the hook (Fig. 4.2) at the level of the inversion (identified as the height of minimum temperature where relative humidity is larger than 50% from ECMWF profiles, which is 1-1.5 km at most hook locations) on 18 October at 12 UTC indicate subsidence and advection from the South American coast at 700-800 mb between 34-37°S (Fig. 4.3). This suggests that a possible source of hook aerosols could be entrainment of FT air that has been lofted by upslope flow in the vicinity of Central/Southern Chile. Although the two westernmost trajectories do not quite intersect the coast, the clearly connected nature of the observed hook (Fig. 4.2c) suggests that these outer hook locations have similar sources. All the FT trajectories may be subject to increasing errors near the coast and close to the Andes, where upslope flow is closely confined to the orography (e.g. Toniazzo et al. 2011). Despite not intersecting the coast, the westernmost 3D trajectories get closer to it than do the corresponding 2D MBL trajectories (from Fig. 4.2, also reproduced in Fig. 4.3), further supporting the idea that advection of continental aerosols to the remote ocean is more likely in the FT than the MBL.

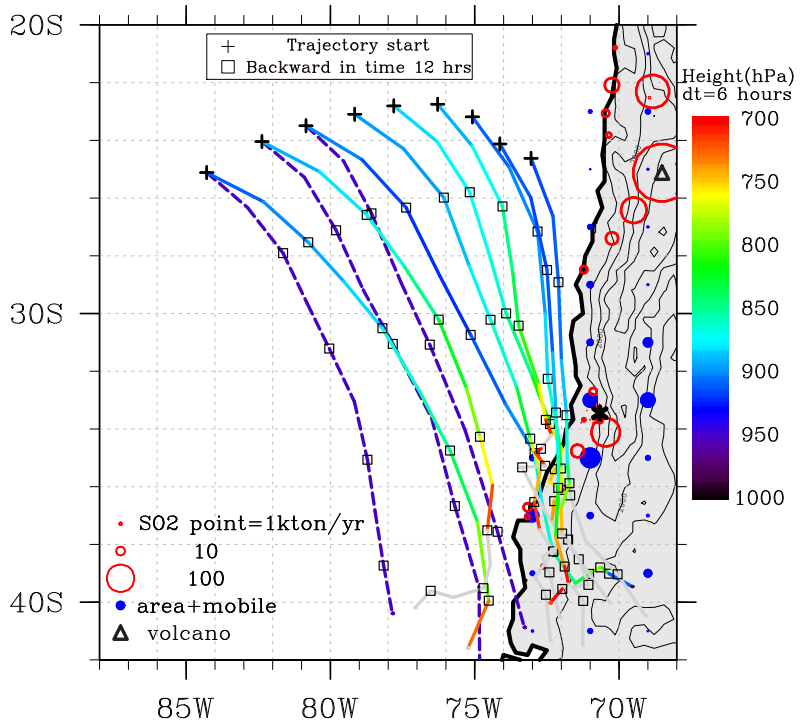

Figure 4.3: ECMWF 3D back trajectories initialized from 2D hook MBL trajectory points on 18 October at 12 UTC (Fig. 4.2), but at the inversion level (the ECMWF level at which temperature is a minimum for relative humidity larger than 50%) rather than 950 hPa. Colors represent trajectory heights in hPa, gray indicating heights above 700 hPa. Squares mark 12 hour time intervals. Dashes lines show a few 950 hPa MBL 2D trajectories from Fig. 4.2. Land contours are elevation height in 1000m resolution and the * marks Santiago. SO_2 emissions from anthropogenic and volcanic sources are shown with open red circles for point sources (including smelters and volcanos) and blue filled circles demonstrating $2 \times 2°$ average area+mobile urban and industrial sources.

The latitudes where most of the 3D hook back trajectories approach the coast are mainly to the south of the major anthropogenic sources (including Santiago at 33.5°S, 70.7°W, 500m AMSL and the Caletones copper smelter at 34.1°S, 70.5°W, 1700m AMSL, see Fig. 4.3). Over land the back trajectories do not appear to originate from this source region. The small

point emissions near sea-level on the coast near 37°S are insufficient to provide significant hook CCN. Coastal biogenic, dust and fire related aerosols are unlikely to cause the heavily polluted N_d seen in the hook given they do not explain the large mean N_d nearer the coast (Allen et al., 2011). Volcanic emissions and copper smelters in Northern Chile (north of 30°S) are large sources of SO_2, but hook trajectories do not indicate obvious influence from this region.

The VOCALS C-130 flight that took place 18 October (Wood et al., 2011b) along 20°S and sampled the large remote N_d a few degrees north of the trajectory end points in Fig. 4.3 measured 100-200 cm^{-3} CCN concentration (at a supersaturation σ=0.4-0.5%) during above-cloud flight legs, which is insufficient to explain the observed 150-300 cm^{-3} N_d measured during in-cloud legs and noted in satellite data. Given the lack of an observed FT source in this case, it is difficult with REx observations alone to establish the source of hook CCN.

4.3 Model evaluation

In Chapter 3 we described our WRF-Chem configuration and provided validation against several metrics that provided confidence in the model. Here we show the ability of the model to reproduce key features of Hook1. Other studies have used versions of WRF-Chem to simulate the VOCALS-REx period and have been able to reproduce, with some fidelity, the key cloud and chemical features, including 20°S time-mean longitudinal gradients of sulfate, aerosol concentration and N_d (Yang et al., 2011b; Saide et al., 2012). Although our simulation employs slightly different parameterization options and resolution, it also reasonably reproduces REx mean conditions. The gradient of REx mean N_d along 20°S agrees well with satellite and aircraft data (Fig. 3.1) even though the magnitude is underestimated by 10-30%. Like the Yang et al. (2011b) and Saide et al. (2012) simulations, the MBL aerosol and sulfate concentrations are biased low, but capture the longitudinal gradient. Unlike Saide et al. (2012) we do not tune the background SO_2 in the FT to match VOCALS observations, so mean SO_2 and CCN in the FT are also lower than observed. As in Saide et al. (2012), we find that Lin microphysics leads to a mean high precipitation bias along 20°S, which partly explains the model's low LWP bias (Fig. 3.1), may explain

the low bias in N_d and possibly shortens the lifetime of aerosol species in the MBL.

4.4 Hook1

4.4.1 Modeled Hook1 evaluation

The model captures the life cycle of a hook between 17-20 October, shown in Fig. 4.4, that is in broad agreement with the observed Hook1 shown in Fig. 4.2, although there are some differences in its timing and extent. On 19 Oct at 1515 UTC the observed N_d spatial pattern (Fig. 4.2c) is a clear example of what we define as a hook. At this time, there is a modeled hook (Fig. 4.4e), but it is shifted several degrees to the north of the observed hook. The modeled hook 24 hours earlier (Fig. 4.4c) more accurately represents the observed hook at 15 UTC on 19 Oct, indicative of a timing bias. In addition, the westward tip of the modeled hook is about 5 degrees further west than the observed hook. The N_d maxima in the modeled hook are comparable to those in the observed hook, and the arched shape of the hook is well-captured, but the observed hook is considerably narrower than the modeled hook. The time evolution of N_d is in good agreement with observations, with both showing a persistent feature advecting northward through the region over several days before decaying. On the other hand, several features of the pattern of observed and modeled N_d do not match. The model simulates a second large hook north of the one we have focused on (Fig. 4.4b, 4.4c). Although the observations do indicate a protuberance of polluted N_d reaching west of 80°W ahead of Hook1 (Fig. 4.2b, 2c), this observed feature is not so clearly hook-shaped, does not extend as far westward, and is more spatially separated from Hook1 than in the model (Fig. 4.2b, 6c). The model also does not reproduce the high N_d values east of 75°W between 18-26°S.

Model MBL 2D trajectories accurately follow the modeled hook feature (Fig. 4.4). Trajectories are computed both forward and backward starting from points along the maximum model N_d on 19 Oct at 03 UTC to trace both the development and decay of the modeled hook. Trajectories are initialized two model levels below the inversion, between 910-950 hPa, and are computed with horizontal wind components only. Figure 4.4 suggests that the modeled hook along these trajectories coincides with a large source of CCN just above

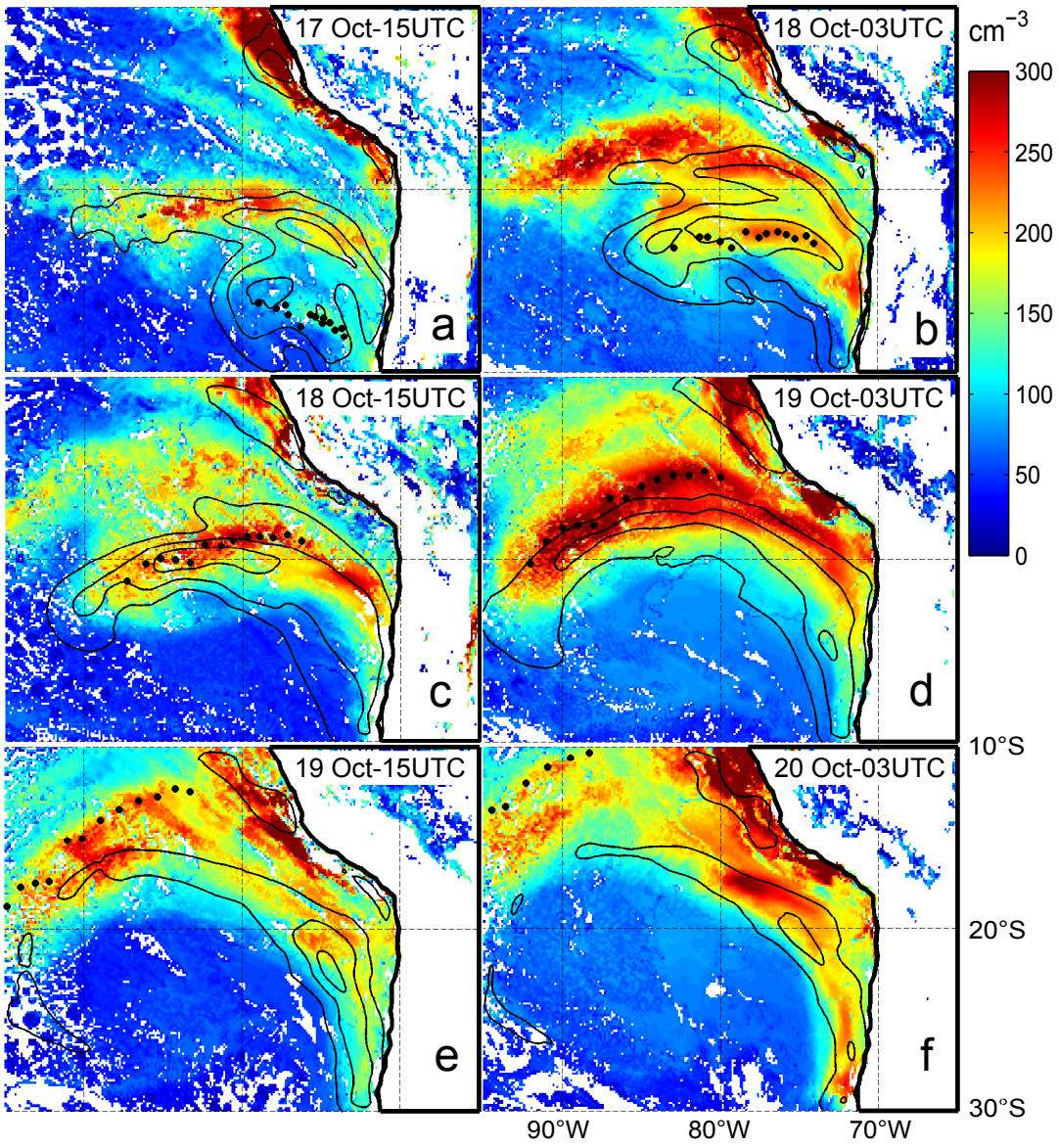

Figure 4.4: Model N_d (colors) with filled black circle markers following thirteen WRF-Chem 2D MBL trajectories. Trajectories are initialized from points along the peak N_d on 19 Oct at 03 UTC (panel **d**) 2 model levels below the inversion (∼910-950 hPa). They are computed forward until they reaches the NW corner of the domain, and backwards until 17 Oct at 03 UTC. Black contours are CCN in the model layer above the inversion at 100, 300 and 500 cm^{-3}.

the inversion. Over time, this modeled FT source decreases in number concentration due to entrainment and falls behind the hook due to vertical wind shear.

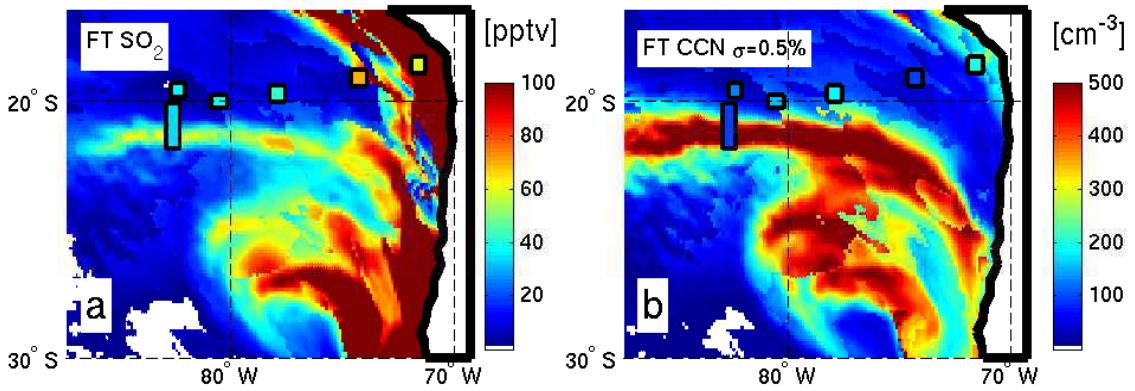

Figure 4.5: Contours of model **(a)** SO_2 and **(b)** CCN at $\sigma = 0.5\%$ in the model level above the inversion on 17 October at 15 UTC, 24 hours before the VOCALS C-130 RF02 flight (13-21 UTC 18 Oct) to correct for model and satellite observations time offset of N_d (Figs. 4.2 and 4.4). Superimposed rectangles show above-cloud flight leg mean data SO_2 measurements and CCN when measured for $\sigma = 0.4 - 0.5\%$.

Measured SO_2 and CCN concentration (at σ=0.4-0.5%) in the FT during the C-130 Hook1 flight (on 18 October) indicates the flight did not sample a strong FT aerosol source (Fig. 4.5) that can explain the coincident large N_d (e.g. Fig. 4.2b). The time offset between model and satellite observations of the peak hook N_d crossing 20°S is 24 hours, so flight data is compared with model output 24 hours earlier (Fig. 4.5), on 17 October. Although flight SO_2 values are in agreement with the branch of model SO_2 elevated above the background slightly south of the flight measurements, this is partly due the mean bias in the model FT SO_2 concentrations. The 40-50 pptv observed in the remote ocean FT is slightly larger than the 20-40 pptv observed on average by C-130 flights during REx along 20°S (Allen et al., 2011), but because the CCN measured in the FT is also not notably large this was not interpreted as a significant FT pollution event. The CCN flight measurements agree very well with the model (except in the furthest SW leg), which inspires some confidence in the model representation. The model suggests that a large FT CCN source coincided with Hook1 (Fig. 4.5b), but further south than the flight measured. Additionally this modeled

FT CCN source contributes to the northern N_{d} hook that is erroneously large as explained above. It is likely that during the flight N_{d} was large due to a FT source that had already entrained. At the comparison time modeled N_{d} is not large in the flight region (Fig. 4.4a), but later times in the model (e.g. Fig. 4.4b) indicate that large N_{d} ahead of a large FT CCN source can occur and is modeled, just not in the same times and places as observed. The flight did not sample the hook edge, and thus likely simply did not sample a region of entrainment of high concentrations of FT CCN.

4.4.2 Interpolation over 2D trajectories

Hook development

Figure 4.6 shows cloud and aerosol properties interpolated along WRF-Chem 2D MBL backward and forward trajectories initialized at a set of points along the hook at 03 UTC on 19 October (see Fig. 4.4), and demonstrates the development and decay of Hook1. We construct a time series of the average in-cloud N_{d} over all trajectories with LWP > 0.01 gm^{-2} (Fig. 4.6a). The concentration $N_{\mathrm{CCN,FT}}$ of CCN in the model layer above the marine inversion peaks at $\sim$600 cm^{-3}, some 15 hours before the peak of CCN within the MBL, and decreases rapidly thereafter. By the time of peak N_{d}, fewer than 100 cm^{-3} FT CCN remain. During the second half of the hook life cycle, the $N_{\mathrm{CCN,FT}}$ decreases to low levels (Fig. 4.6a) and precipitation reaching the surface increases (not shown) while air entrained from the FT has low CCN concentrations, so $N_{\mathrm{CCN,MBL}}$ and N_{d} decrease without a major source to replace droplets lost to precipitation and dilution. This provides strong evidence that entrainment of FT aerosol is a dominant source of simulated hook aerosol and N_{d}. The earlier increase of $N_{\mathrm{CCN,FT}}$ (Fig. 4.6a) is due to the arrival at the inversion of a subsiding aerosol layer (see Section 4.4.4).

The peak in hook N_{d} lags the final rise in MBL CCN concentration ($N_{\mathrm{CCN,MBL}}$) by $\sim$9 hours and the $N_{\mathrm{CCN,FT}}$ peak by 24 hours (Fig. 4.6a). The former lag is explained by a reduced supersaturation maximum and therefore a lower fraction of CCN activated in the clouds during daytime because TKE is stabilized by solar absorption (local transition from night to day occurs at $\sim$12 UTC). This effect is also seen during the subsequent day

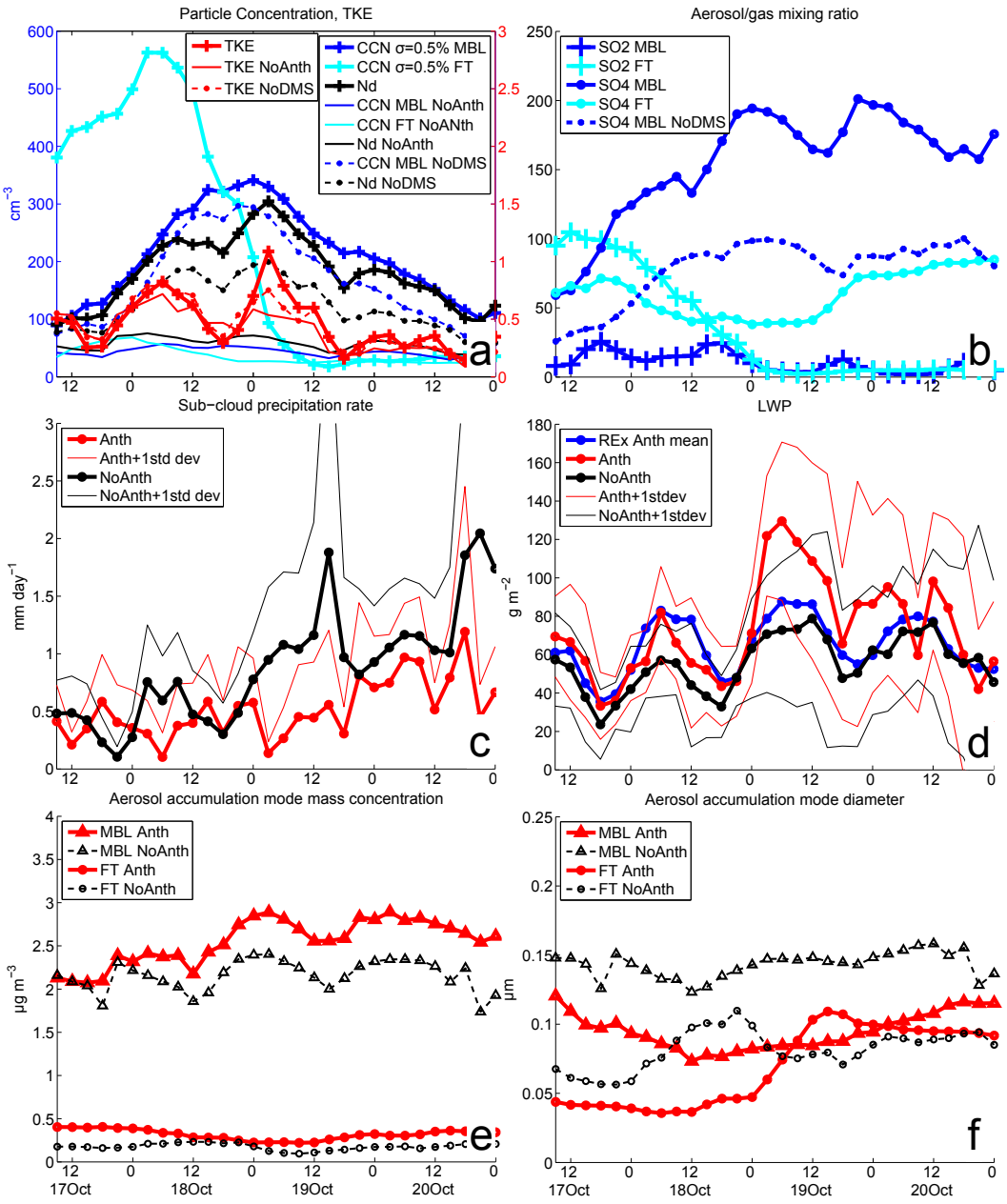

Figure 4.6: Average of cloud and aerosol properties interpolated along ninety-five 2D hook trajectories, computed in the same manner as those marked Figure 4.4, both in the model layer just above the inversion (FT) and in the MBL at the cloud level. **(a)** FT CCN (cyan) and MBL CCN (blue) at 0.5% SS with N_d (black) and turbulent kinetic energy (red). The Anth simulation has '+' markers. Lines without markers are the NoAnth simulation and circle markers with dashed lines indicate the NoDMS simulation. **(b)** SO_2 ('+') and SO_4 (circles) in the FT (cyan) and MBL (blue). The dashed blue line indicates NoDMS MBL SO_4. In **(c)**-**(f)** properties in the Anth (red) and NoAnth (black) are compared. Thin solid lines indicate 1 standard deviation outside the mean of hook points. **(c)** Precipitation rate simulations at sub-cloud level. **(d)** LWP and REx mean L_p at the same time of day at hook trajectory locations (blue). Accumulation mode aerosol mass and computed accumulation mode diameters are shown in the **(e)** and **(f)** in the MBL (triangles) and FT (circles).

starting at 12 UTC on Oct 19. The daytime decline in TKE reduces the turbulent vertical velocity variance and thus maximum effective in-cloud supersaturation, which increases in the size of the smallest particle activated and decreases the fraction of aerosol particles that become droplets. The daytime separation between N_{d} and $N_{\mathrm{CCN,MBL}}$ is indicative of a population of small CCN entrained from the FT that is strongly sensitive to the maximum supersaturation achieved during the activation process. That is, there are small CCN that aren't activated, but would in a more turbulent cloud with higher supersaturation.

The activation of these additional CCN occurs during the 6-9 hours leading to peak N_{d}, which also corresponds to a peak in TKE. The increase in $N_{\mathrm{CCN,MBL}}$ is the essential condition enabling hook formation, but MBL turbulence and chemistry also influences the variability in N_{d} over the lifecycle of a hook. As the hook feature forms, FT SO_2 is elevated well above MBL values, so entrainment is a source of SO_2 (Fig. 4.6b), which is oxidized to sulfate in the MBL. This entrainment source explains some, but not all, of the large increase in MBL SO_4 aerosol mass during the hook growth period. A surface sulfur source is also important as demonstrated by the fact that the MBL SO_4 mass is reduced by $\sim$40% in the NoDMS simulation (Fig. 4.6b). Despite the importance of the surface DMS source for increasing MBL sulfate aerosol mass, $N_{\mathrm{CCN,MBL}}$ is not strongly sensitive to the surface DMS source (Fig. 4.6a). This is primarily because the SO_2 mainly condenses onto and enlarges existing particles. While this does move some particles into the CCN size range, this is not a major effect, consistent with previous modeling studies (e.g., Woodhouse et al., 2010).

The value of N_{d} is more sensitive than is $N_{\mathrm{CCN,MBL}}$ to the inclusion of DMS (Fig. 4.6a). This is also seen in Fig. 4.7a,b, which compares the N_{d} fields at one particular time for NoDMS with the control Anth simulation. This sensitivity is due to a complex consequence of several factors, including changes in particle size and TKE differences (Fig. 4.6a). However, another consideration is that in the NoDMS run, the hook in N_{d} is displaced a few degrees southeast, so the maximum N_{d} is not sampled by the trajectories shown in Fig. 4.6a.

Although the hook event appears to result from significant entrainment of CCN, the total accumulation mode aerosol mass per unit volume above the inversion is less than 0.5

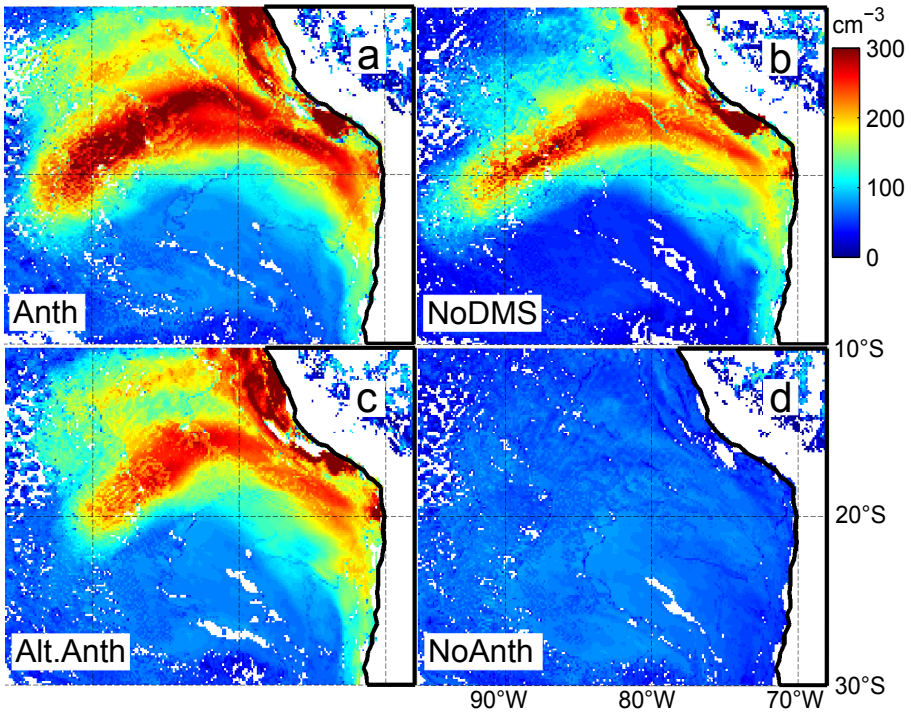

Figure 4.7: Snapshots of N_d on 19 Oct at 3 UTC from different simulations: **(a)** Anth, full anthropogenic emissions, includes DMS; **(b)** NoDMS, full anthropogenic emissions, no DMS; **(c)** Alternative Anth: no anthropogenic emissions south of 30°S, east of 70°W, includes DMS; **(d)** NoAnth, no anthropogenic emissions, includes DMS.

μgm^{-3}, much smaller than the 2-3 μgm^{-3} averaged in the MBL (Fig. 4.6e). The mean accumulation mode dry volume diameter (calculated from mass and number values) is only $\sim$0.04 μm in the FT vs $\sim$0.1 μm in MBL (Fig. 4.6f) during hook development. With sea salt aerosols comprising a large fraction of the accumulation mode aerosol mass in the MBL, only a small relative increase in MBL aerosol mass occurs as the FT aerosols are entrained. Thus the FT source is comprised of numerous small aerosols, strongly impacts the MBL aerosol number concentrations and has little impact on aerosol mass within the hook. It is also worth noting that the contribution of organic aerosols to the overall aerosol mass in the FT immediately above the hook is only 10-20% in the model, and so most of the contribution to CCN associated with the hook is from sulfate.

Hook impacts on cloud properties

Without anthropogenic aerosols (in the NoAnth simulation), no hook forms (Fig. 4.7). Thus, comparing the cloud properties in the NoAnth and Anth simulations at the same locations/times allows us to distinguish cloud macrophysical changes due to anthropogenic aerosols from meteorological changes. Their differences between the NoAnth and Anth simulations maximize near peak hook N_{d} ($\sim$3 UTC on 19 Oct, Fig. 4.6a) and show diurnal modulation. The hook aerosols cause increased TKE (Fig. 4.6a) and LWP (Fig. 4.6d), most likely due to the suppression of precipitation due to increased CCN (Fig. 4.6c) and associated reduction in stabilization (Ackerman et al, 2004). The precipitation below cloud base is 1-2 mmday^{-1} in the NoAnth simulation right around the time of the peak hook N_{d}, and is cut by roughly 50% due to the hook aerosols. A strong diurnal cycle in LWP is found in both the Anth and NoAnth cases (Fig. 4.6d) but hook aerosols increase LWP more at night (especially during the night of the peak hook N_{d}). This is likely a consequence of the strong coincident precipitation suppression. We examine the impacts of these cloud macrophysical changes on the albedo in Section 4.4.3. From 0-9 UTC on 20 October surface precipitation is suppressed (not shown), but sub-cloud base precipitation rate is only weakly suppressed and Anth LWP is much smaller than the night before, due to a weakened influence of hook aerosols and dips strongly at 9 UTC. This doesn't coincide with a more rapid CCN loss rate, so may indicate a process that reduces droplet size during hook decay.

For context, Fig. 4.6d also shows the mean LWP from the Anth simulation at the same times of day/locations from the entire REx period. Other than exhibiting a strong diurnal cycle, the REx mean LWP does not change markedly following the northward motion of the evolving trajectory position, indicating that the LWP evolution along the trajectory in the Anth and NoAnth runs is not driven by geographical variation in meteorology. That the nighttime LWP increases from the night of the 17-18 October to the following night in the NoAnth simulation means some of the increase in Anth simulation nighttime LWP is caused by meteorological peculiarities of the hook event. During the initial hook formation stages subsidence is stronger than average (Fig. 4.8), which causes lower inversion heights than average (not shown) despite weaker lower tropospheric stability than in the REx mean.

Following the developing hook the stability increases, which maintains the strong capping inversion and weakens entrainment, which suppresses the lifting of the cloud base level. The weakening subsidence allows the MBL top to rise despite the strengthening stability, so cloud thickness and LWP increase.

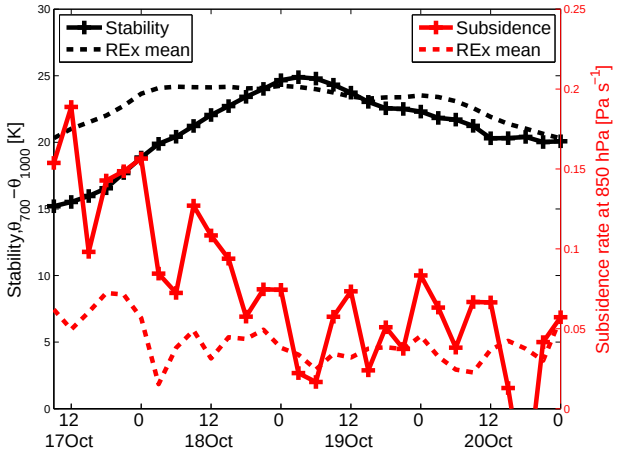

Figure 4.8: Average stability (black) and 850 hPa subsidence rate (red) interpolated over Hook1 2D trajectories (same trajectories used in Figure 4.6). Stability is defined as the difference in potential temperature between 700 hPa and 1000 hPa ($\theta_{700} - \theta_{1000}$) and subsidence is the grid-scale vertical velocity in pressure units (Pas^{-1}). Crosses mark the Anth simulation and dashed lines denote the REx mean at the locations and times of day of the Hook1 trajectories.

4.4.3 Impact of hook on albedo

LWP and N_d (discussed above) and f_c (not shown) are, on average over the hook, greater due to the hook-forming aerosols in the Anth simulation than in the NoAnth simulation (Figure 4.6), so the secondary indirect effects of anthropogenic emissions generally enhance the Twomey effect on hook albedo. We estimate model albedo using model-derived N_d, LWP and f_c following the method of George and Wood (2010). This allows us to separate the Twomey effect, the impacts of microphysics (N_d), from albedo changes due to secondary effects (LWP and f_c). These computed albedo values are about 10% larger than albedo derived from model top of atmosphere shortwave flux due to the influence of atmosphere

above the clouds not addressed by the computation and differences in scattering assumptions between the albedo computation and the model. For each day following the hook the daily solar insolation weighted mean albedo is computed to capture the net hook AIE impact. The albedo from the Anth simulation along the hook trajectory is 35-50% larger than in the NoAnth simulation (Fig. 4.9). Albedo computed using the Anth simulation macrophysical properties, but NoAnth values of N_{d} (blue circles in Fig. 4.9) demonstrates that the Twomey effect contributes ∼50-70% of the hook albedo enhancement over that in NoAnth, while aerosol-induced LWP and f_{c} changes and meteorological variability between Anth and NoAnth simulations contribute the rest. Note that Fig. 4.9's representation of the Twomey effect uses the Anth simulation as the reference case, which is different from studies using global climate models which would typically use NoAnth as the reference. The ∼20% temporal increase in Anth albedo following the hook (from 0.41 to 0.49) demonstrates the significant change in albedo that an individual hook event can cause. The smaller (∼13%; 0.3 to 0.34) temporal increase in NoAnth albedo is due partly to the increase in LWP associated with the increasing stability and weakening subsidence. Removing DMS from the simulation causes a 20-25% reduction in hook albedo, and indicates a systematic effect of aerosol growth due to DMS-derived SO_2 (Fig. 4.9). Before the hook has formed on 17 October, excluding DMS reduces albedo to a magnitude similar to the NoAnth simulation and a ∼43% temporal increase in the NoDMS hook albedo indicates omitting this important SO_2 source would cause an overestimation in the albedo change caused by the hook. DMS thus impacts the background MBL properties that noticeably affect the entrained hook aerosols and resulting radiative changes.

4.4.4 3D pathway of hook FT aerosol

The evolution of aerosol and cloud properties along 2D MBL trajectories allows us to examine how the hook is formed by entrainment of FT aerosols, but this cannot identify the original source of the aerosols, nor does it explain the meteorological conditions that allow for the transport of pollution to the remote ocean. Model 3D back trajectories (not shown) from regions of large FT CCN indicate that the Santiago region (33-35°S, 70-72°W) is the

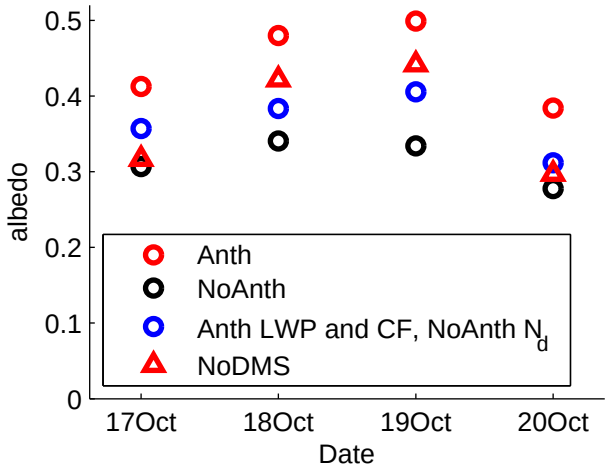

Figure 4.9: Average albedo interpolated over Hook1 2D trajectories (same trajectories used in Figure 4.6) and averaged over each day, weighted by solar insolation. The Anth (red circles), NoAnth(black), and NoDMS(red triangles) simulations are shown. The blue circles are albedo computed using Anth L_{p} and f_{c}, and NoAnth N_{d} and include a correction for biases caused by WRF-Chem's binary f_{c} (average the Twomey effect estimates using Anth and NoAnth as the base simulations with constant L_{p} and f_{c}). The Twomey effect estimate is thus the difference between red and blue circles, while secondary effects are represented by the difference between blue and black circles.

dominant source of aerosols and precursors for the hook. It is more illustrative to examine forward 3D trajectories initialized among the Santiago-region sources that eventually transport offshore and contribute to the hook CCN. The circle markers in Fig. 4.10 show one such representative trajectory. It begins 15 Oct at 18 UTC at 2 km altitude near the surface above the Caletones smelter (34.125°S 70.5°W, 1700 m AMSL). The Caletones smelter contributes SO_2 emissions of 108 kTonyr^{-1}, or ∼40% of the total SO_2 emissions south of 28°S and west of the Andes. Although smelters alone make a relatively small contribution to the mean SEP aerosol population (Twohy et al., 2012), this trajectory represents one pathway in which copper smelter emissions may reach the remote ocean. The left panels of Fig. 4.11 and Fig. 4.12 show longitude-height slices at key times at the latitude of the trajectory location; the right panels show corresponding REx-mean conditions. The trajectory is situated within a plume of high CCN concentrations (cyan contours) and SO_2

concentrations (yellow contours) and reaches the inversion level near 80.5°W, 20.5°S on 18 Oct at 15 UTC (Fig. 4.12c), contributing aerosols to MBL in the Hook1 growth phase (see Fig. 4.6).

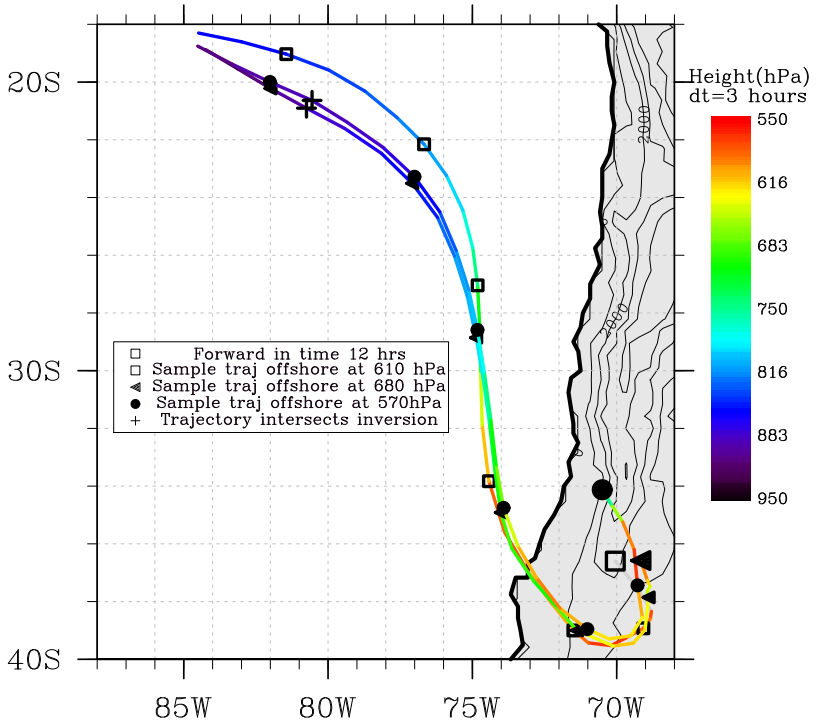

Figure 4.10: Three forward WRF-Chem trajectories from 15 October at 18 UTC to 19 October at 0 UTC that follow polluted CCN in the FT from land to Hook1 and advect offshore at different heights. Markers indicate 12 hour intervals and marker shapes distinguish the trajectories. Circle markers follow the trajectory shown in Figures 4.11 and 4.12.

During the early days of this trajectory (15-16 Oct), anomalously strong southward Andes barrier winds (Rahn and Garreaud, 2010a; Toniazzo et al., 2011) prevail north of 37°S over the Andes (compare left and right panels, Fig. 4.11a-d), causing stronger than average southward transport of Santiago region emissions. This is supported by an upper

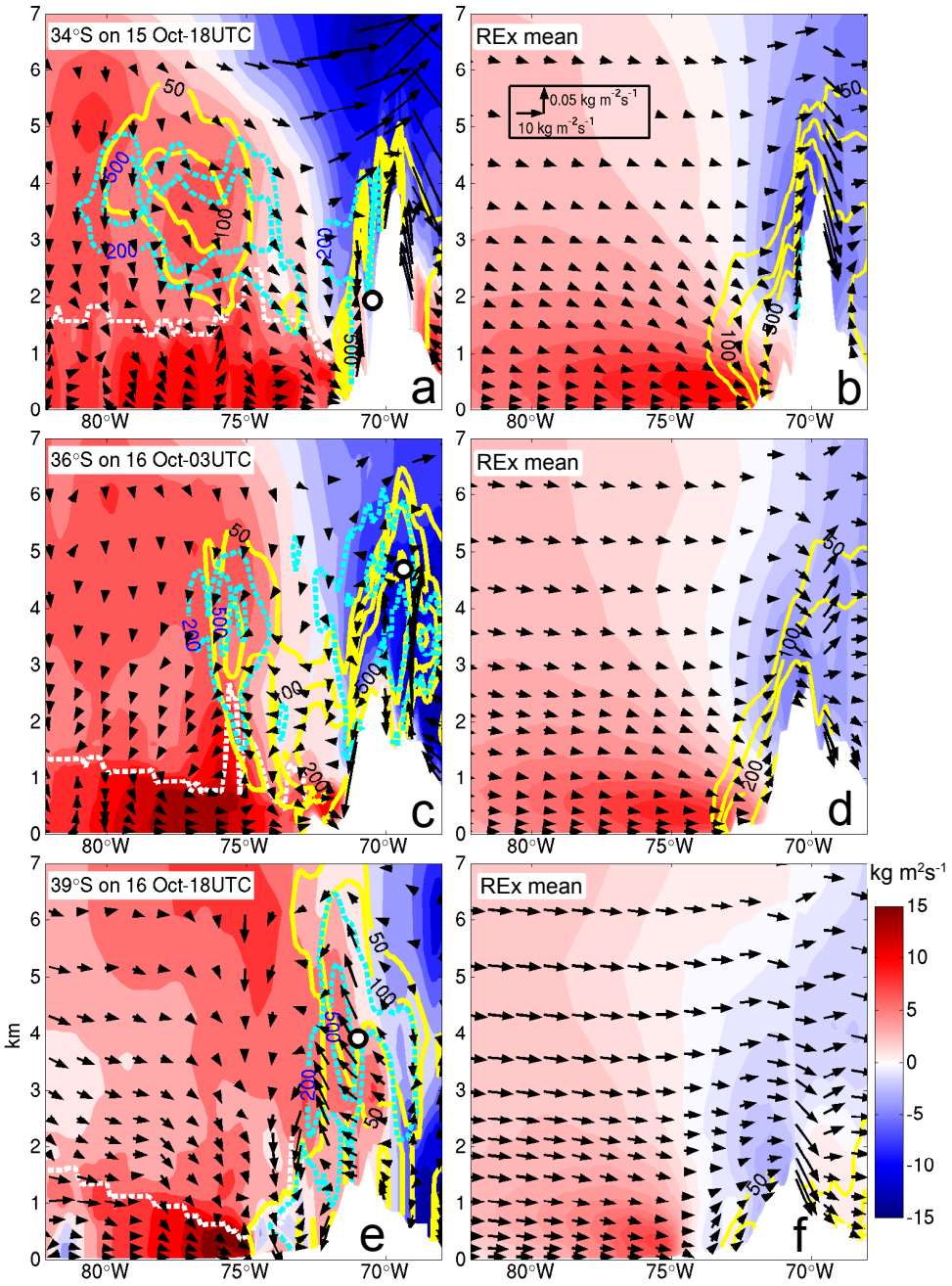

Figure 4.11: WRF-Chem zonal transects at latitudes following a WRF-Chem 3D trajectory (white circle markers here, following the trajectory marked with circle in Fig. 4.10) of winds (multiplied by density to give mass fluxes), CCN at 0.5% supersaturation (cyan dashed lines) at 200 and 500 $cm^{-}3$ (labeled blue), and SO_2 concentrations (yellow lines) at 50, 100, 200 and 500 pptv (labeled black). Filled colored contours show the magnitude of the meridional component of wind (positive is southerly flow), while vectors show zonal and vertical components. The white dashed line indicates an estimate of the inversion height. Left columns are interpolated snapshots at the time of the trajectory and right columns show REx mean properties at the same latitude.

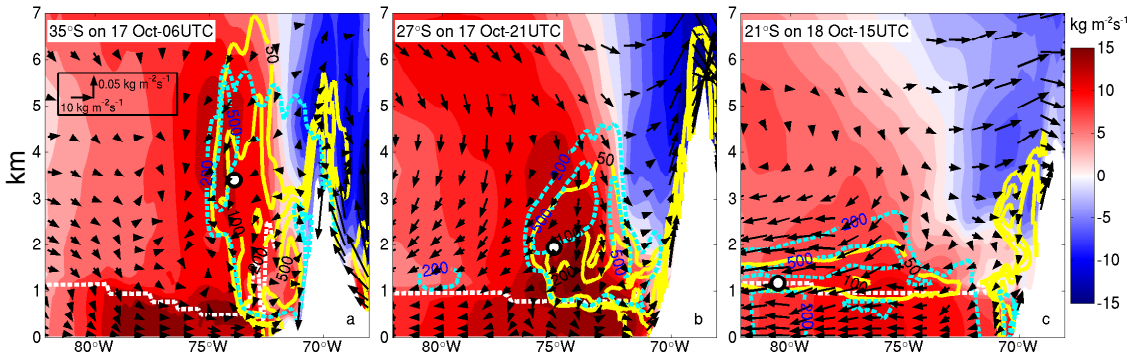

Figure 4.12: Same as left column of Figure 4.11, but for second half of the WRF-Chem 3D trajectory (circle markers in Fig. 4.10) described in Section 4.4.4 as it advects northwest and subsides towards the boundary layer.

level trough (Fig. 4.13b) ahead of a southeastward shifting subtropical high and cyclonic flow ahead of this feature near Santiago. The polluted air advects southward along and up the Andes and reaches 37-40°S, a typically clean region with few local pollution sources (Fig. 13f), on 16 October. During this period of southward transport, ascent over the Andes is also stronger than average (Fig. 4.11a vs. 4.11b). Some of the vertical enhancement may be due to the normal diurnal cycle, as in the vicinity of the Andes the mountain breeze maximum and land-sea circulation are associated with ascent later in the day (Toniazzo et al., 2011). At the trajectory start time (local time ∼3 pm) ascent is therefore expected. However, there is also stronger than average onshore flow aloft (due to the anomalous cyclonic flow) encountering the Andes barrier (Fig. 4.11a, 4.11b) and enhancing the vertical motion. The upward motion leads to a large plume of SO_2 and CCN rising to over 5 km near 36°S nine hours after the trajectory start (Fig. 4.11c). The trajectory actually moves over the crest of the Andes. At this time, the flow at 3-6 km contains little or no zonal component as the trajectory nears the center of the mid-tropospheric cyclone (Fig. 4.13b).

The shift of the subtropical high towards the coast on Oct 16 drives strong surface southerlies at 36°S and the approaching upper level trough encourages onshore flow at 700 hPa to the north of 36°S and offshore flow to the south (Fig. 4.13b). Normally, the flow near and south of Santiago is onshore throughout the lower troposphere (Fig. 4.11b, d, f)

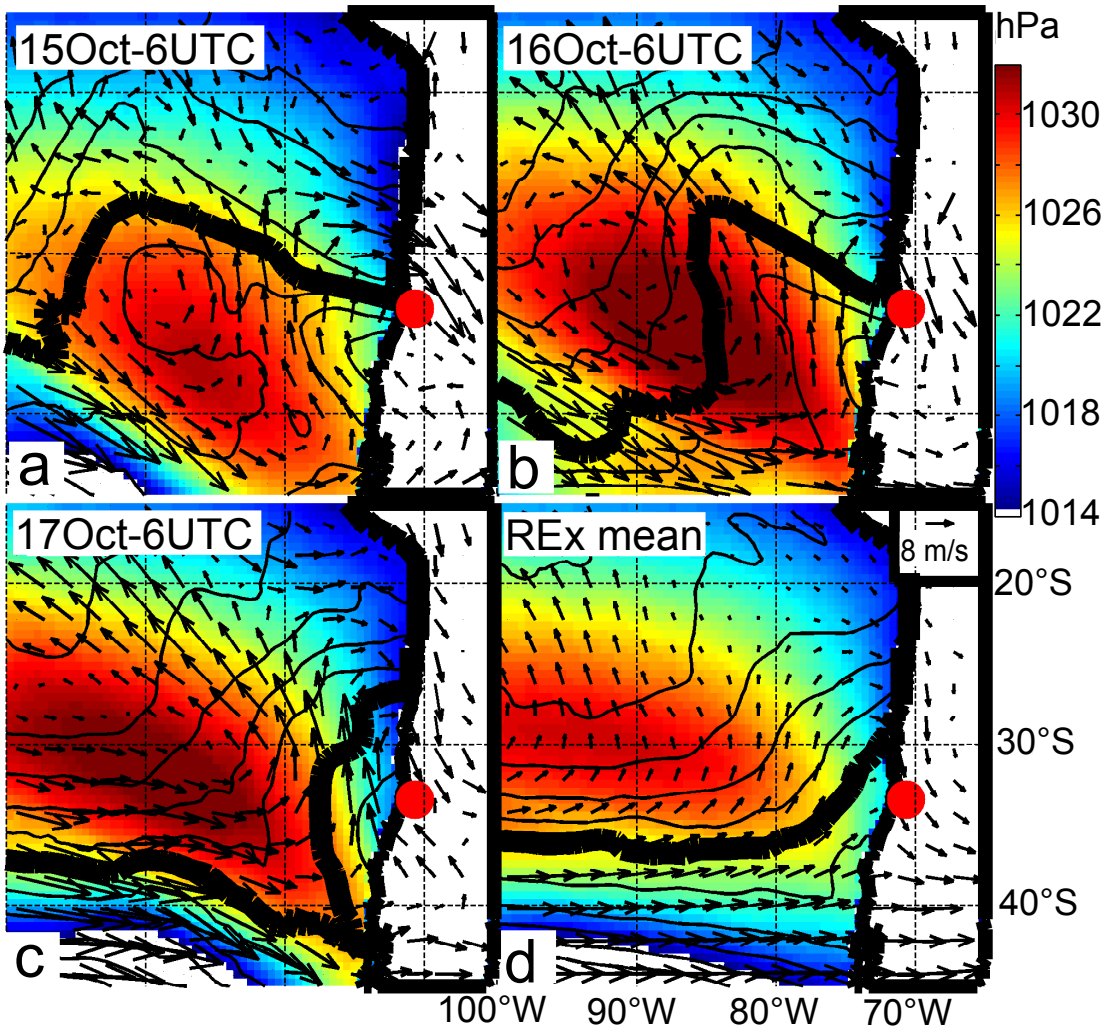

Figure 4.13: WRF-Chem simulation surface pressure (colored contours), 500 hPa heights (line contours) and 700 hPa winds (arrows) at **(a)**-**(c)** in days preceding Hook1 at 06 UTC, and **(d)** REx mean conditions. The red circle marks Santiago. The bold 500 hPa contour is 5350 m and the contour interval is 50 m.

and does not therefore carry urban emissions over the remote ocean. On average surface emissions in the Santiago area advect weakly northward (similar latitude shown in Fig. 4.11b), but if lofted high enough (>2 km) to reach the Andes northerly barrier flow, the primary direction of transport is southward. In the Hook1 case, the pollution plume, having moved southward to 39°S, is then subject to offshore flow over a deep layer from the surface

to over 6 km (Fig. 4.11e). This day coincides with the peak in the strength of the subtropical high (Fig. 4.13b), which is shifted southeast of its REx mean (Fig. 4.13d). The lower height of the Andes at 39°S compared with Santiago's latitude also reduces their blocking effect and allows westward flow at lower levels and a deep column of offshore aerosol transport.

Southward transport of Santiago region emissions occurs regularly and is visible in the modeled REx-mean SO_2 concentrations. For example, at 36°S SO_2 concentrations exceeding 100 pptv extend above 4km on average (Fig. 4.11d). Usually, this plume is advected eastward across the Andes; it is the enhancement of this feature (over 500 pptv above 4km, Fig. 4.11c) due to the strengthened southward winds, combined with meteorological conditions conducive to subsequent offshore flow that allows for the formation of the modeled Hook1. Nucleation of the enhanced SO_2 in this specific case is also important to create the high CCN seen in Hook1, but not in the mean state.

By 6 UTC on 17 Oct (Fig. 4.12a) northwestward flow has looped the trajectory back to its starting latitude, but west of its starting point, by which time the subtropical high has partly relaxed towards its climatological mean (Fig. 4.13c). As the upper level trough nears the coast it suppresses the normal zonal flow and induces a strong northward flow, especially at 74-75°W (Fig. 4.10). Together with stronger than average subsidence west of the trough on 17 Oct, between 6 and 21 UTC on 17 Oct (Fig. 4.12a, 4.12b), the trajectory advects westward by only about 1°, but northward by about $7 - 8°$ and subsides by about 1.5 km. The top of the plume also drops substantially, and for the remainder of the FT plume lifespan it subsides and spreads above the inversion level. By the time the trajectory reaches 20.5°S on 15 UTC 18 Oct the plume is entraining into the MBL and its vertical extent reaches only to 1 km above the inversion (Fig. 4.12c).

Whether a particular polluted plume in the FT contributes to a hook downstream is dependent on the timing, magnitude and location of offshore flow and its altitude above the stratocumulus. For example, at 36°S on 03 UTC 16 Oct (Fig. 4.11c), a plume of SO_2 between 1-3 km (72-75°W) extends offshore in low level easterlies. But as it advects northwards (not shown) it encounters onshore flow associated with near-coast low pressure (Fig. 4.13c) and never contributes to remote CCN. The broad polluted plume already existing in the FT at 34°S 75-81°W at the start of the shown trajectory (Fig. 4.11a) advects

northward until around 28°S (not shown), at which point westward flow associated with the subtropical high transports the plume out over the ocean, providing the source aerosol for the modeled hook to the north of (i.e., preceding) Hook1 (Fig. 4.4b). As mentioned in Section 4.4.1, this feature doesn't match satellite observations well but may represent a noted protuberance of high N_d ahead of Hook1. Back trajectories indicate this modeled plume advected offshore near 39°S on 14 Oct, and before that had traveled southward from the Santiago region, similar to the transport mechanism associated with Hook1. This offshore flow is associated with the same approaching ridge/trough that affects Hook1, and a strong surface coastal low on 13 October.

Figure 4.10 shows two additional 3D trajectories, initialized in a similar elevated SO_2 plume presumably due to earlier southward transport. Despite the difference in starting locations, all three trajectories advect offshore at a similar time, but at different pressures (from 570 hPa to 680 hPa). The lower two trajectories follow very similar paths. The highest trajectory ultimately contributes to the hook further west and later than the lower two as it takes longer to subside. However, the faster speed at which this trajectory travels is offset by the weakened influence of subtropical high induced easterly flow at these higher altitudes, increasing the distance it must travel to the remote ocean compared to the lower trajectories. Thus in this case transport of high CCN into the remote ocean depends on offshore flow at a level that is high enough to avoid intersecting the MBL before reaching the remote ocean, but low enough to be turned westward by the low level flow between 20-30°S.

The model 3D trajectory traced in Figs. 4.11 and 4.12 advects from land to ocean at a pressure level near 610 hPa, which is somewhat higher by ∼100 hPa than those of the ECMWF 3D back trajectories starting at the inversion above the hook (Fig. 4.3). In the model, large SO_2 and CCN concentrations extend up to ∼500 hPa (Fig. 4.11c) and the hook of elevated N_d extends further west than the observed hook. This is consistent with the model simulating overly strong upward vertical transport over land, leading to CCN in the FT in the model that extends further north and west than the observed N_d suggests.

4.4.5 Interpolation over 3D trajectories

Most chemical and aerosol fields interpolated over the 3D trajectory described in Section 4.4.4 do not vary much during FT transport over the SEP (not shown). However, Aitken mode number concentrations decline from ∼800 cm^{-3} to ∼400 cm^{-3} over 12 hours during the early part of the descent toward the MBL top while there is minimal change in the accumulation mode concentration, suggesting coagulation of the relatively large number concentrations of the small ∼0.01 μm particles in the plume. Following this period, accumulation mode, Aitken mode, and CCN number concentrations remain steady until very near the inversion level. Additionally the SO_2 concentration remains steady, as does sulfate mixing ratio, though once the trajectory is near the MBL SO_4 gradually increases by 40% due to aqueous phase processing of entrained and DMS-derived SO_2. This indicates relatively simple advection without significant chemical/aerosol changes until entry into clouds. There is no evidence of strong nucleation events, significant aerosol size changes, or any other mechanism that would change the CCN as a plume of polluted air transports over the marine SEP in the FT.

4.4.6 Sources of hook aerosols

Neither DMS-derived SO_4 nor long-range transport of species input via boundary conditions, both of which are present in the NoAnth simulation, cause hook formation (Fig. 4.7d). A model run without DMS (NoDMS) has lower N_d by ∼15% both in and outside the hook, but the NoDMS hook N_d peak occurs about 1-2 degrees 'behind', or southeast of, the Anth simulation hook (Fig. 4.7a, 9b). In the NoDMS run, both Aitken and accumulation mode number concentrations are very close to those in the Anth simulation, but the accumulation mode particles are smaller, which shifts the MBL size distribution and reduces the number of particles activated. A binned aerosol scheme would probably be more appropriate than a modal scheme to investigate this further.

When emissions south of 31°S are excluded, no clear Hook1 forms (not shown). Emissions from the Northern Chilean smelters and volcanoes do not appear to advect to the remote SEP (Twohy et al., 2012). In a simulation without anthropogenic emissions east

of the Andes (70°W) south of 30°S (Fig. 4.7c), the hook is also shifted behind the Anth hook with smaller peak N_d magnitude, but the basic hook characteristics remain intact. The emissions east of the Andes are small compared to the Santiago region, but also advect offshore with the cyclonic flow and affect the hook shape, extent and magnitude. These sensitivity studies clearly demonstrate that transport of anthropogenic aerosol sources from the Santiago region is the dominant source of Hook1 N_d, but the location and magnitude of the hook is sensitive to processes affecting the FT plume and the MBL CCN.

4.5 Other hooks

Our analysis shows that are four key elements of the Hook1 event are (a) Santiago area emissions; (b) an initial southward and upward transport; (c) subsequent offshore flow; (d) subsidence and entrainment. Two other pronounced hooks formed during REx. In this section we present observations and simulations of these cases, looking for these same elements. Unfortunately, WRF-Chem underestimates the offshore extent and magnitude of the observed N_d maximum in Hook3 and especially Hook2 (Fig. 4.14). However, in both of these cases, the model does simulate offshore flow of Santiago region emissions in the FT that subsides, entrains and enhances N_d west of the region most impacted by coastal aerosols on average (Fig. 4.1).

4.5.1 Hook 2: 2 November, 2008

Hook2, at its peak, is an extended region of high N_d cloud reaching from the Chilean coast between 24-30°S in a northwestward direction out to 20°S, 83°W on 2 Nov (Fig. 4.14a). ECMWF MBL 2D back trajectories from the offshore tip of the hook trace a region of high N_d clouds to near the coast (not shown), indicating that some pollution transport takes place within the MBL from coastal sources to the remote ocean, in contrast to Hook1. The transition from the polluted hook to the clean conditions was sampled near 22°S, 80°W between 09 and 12 UTC on 2 November by the VOCALS C130 flight RF08. Near the coast CCN concentrations exceeding 500 cm^{-3} (at σ=0.5%) were measured in the FT along 20°S, but much lower concentrations (∼150-180 cm^{-3}) further west along 20°S indicate a lack of FT aerosol support for the polluted tongue.

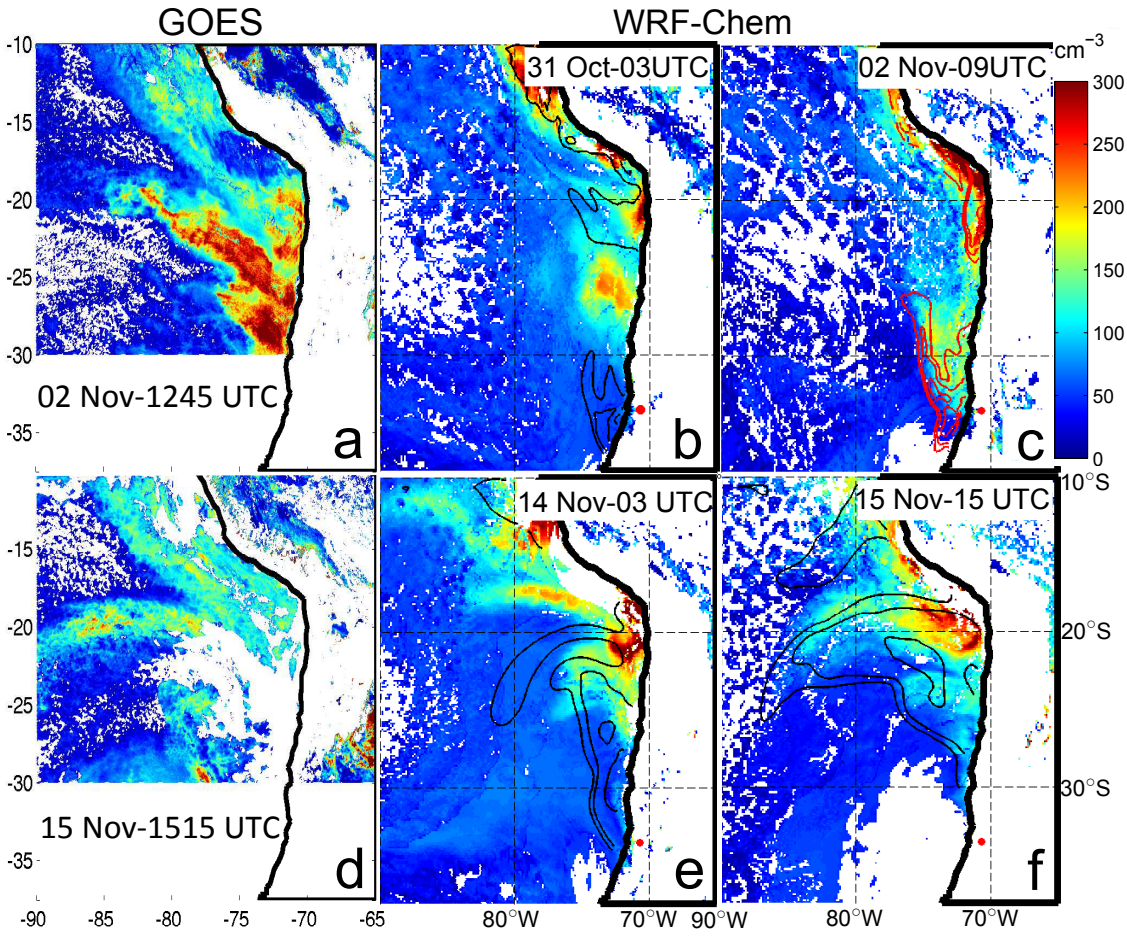

Figure 4.14: GOES-derived N_d of Hook2 on 2 November at 1245 UTC in **(a)** and of Hook3 on 15 November at 1515 UTC in **(e)**, with model N_d snapshots on **(b)** 31 October at 3 UTC, **(c)** 2 November at 9 UTC (chosen because it demonstrates closer agreement with (a) than other times),**(e)** 14 November at 3 UTC and **(f)** 15 November at 15 UTC. The red dot marks Santiago. Black contours are FT maximum CCN at 0.5% at 100, 200 and 500 cm^{-3}. By **(c)** marine FT CCN is <100 cm^{-3} near the region of large N_d, so instead SO_2 at 100, 200, and 400 pptv is shown in red contours.

WRF-Chem severely underestimates the hook N_d for this event (Fig. 4.14c) although a region of somewhat increased N_d extends from the Santiago region to ~25°S, 75°W. This region does not develop further over the remote ocean at later model times. This suggests the model is not correctly simulating the offshore advection of aerosol. There is offshore flow of FT air with 200 cm^{-3} CCN on 30-31 October (Fig. 4.14b) extending from south of

Santiago. On the day of the hook, FT SO_2 concentrations reach 400 pptv along the western edge of the modeled region of elevated N_d region, but no substantial model FT source of CCN remains over the ocean (Fig. 4.14c). The simulated region of large FT SO_2 does not reach west of 77°W or north of 25°S, consistent with the RF08 observations of a relatively unpolluted FT further to the northwest.

Figure 4.15 shows 3D WRF-Chem back-trajectories from the FT above the modeled region of elevated N_d seen in Fig. 4.14c. They indicate lofted air from south of Santiago subsiding towards the MBL (Fig. 4.15a). That higher concentrations of FT SO_2 but smaller number concentrations of CCN are transported offshore in the FT than in the Hook1 case indicates weaker nucleation processes prior to offshore advection and reduces the impact of the entrained plume on N_d (because entrained SO_2 is more likely to add mass to existing aerosols rather than nucleate more particles in the MBL). Three possible reasons why WRF-Chem does not produce the distinct observed hook are (1) excessive CCN loss rates within the MBL, which quickly remove CCN advected in the MBL from coastal pollution sources; (2) underestimated nucleation of new particles in the pollution plume that can subsequently serve as CCN, which may prevent the FT aerosol plume from maintaining the offshore portion of the hook; (3) modeling errors in the altitude, latitude, and/or magnitude of offshore flow of polluted air necessary for continental air to reach the remote ocean.

Like Hook1, a southeastward shifted subtropical high behind an upper level trough both precede the observed hook, but the sea level pressure anomaly is much weaker than in Hook 1 and the upper level trough intersects the coastline further north. This causes a weaker event and a different hook shape, but nonetheless favors transport of pollution into the remote ocean.

4.5.2 Hook 3: 15 November, 2008

Hook3, like Hook1, extends far offshore (Fig. 4.14d), as seen in the satellite retrieval chosen to overlap with VOCALS flight RF14 that sampled the hook out to 80°W near 20°S on 15 Nov between 15 and 20 UTC. A layer with mean SO_2 concentrations of 550 ppt was observed

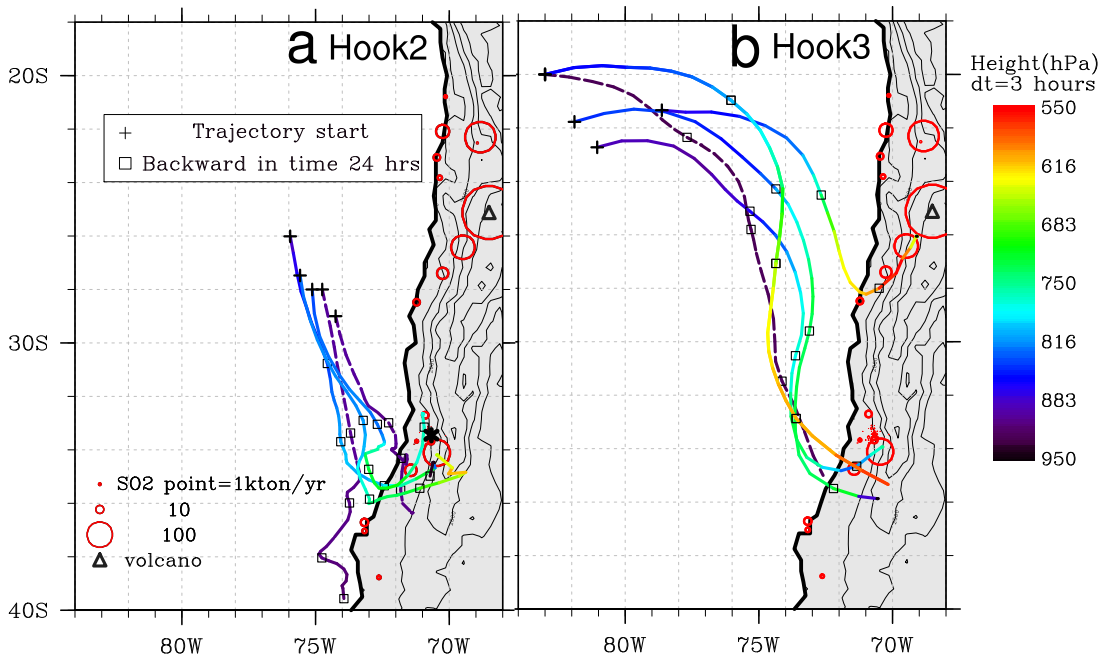

Figure 4.15: WRF-Chem 3D back trajectories (solid) initialized from points in the model level above the inversion within region of large SO_2 concentrations and 2D back trajectories (dashed) in the MBL (2 model levels below the inversion) at points of large model N_d. Trajectories are initialized on **(a)** 2 November at 9 UTC corresponding to the model Hook2 in Fig. 4.14c and **(b)** 15 Nov at 15 UTC corresponding to the model Hook3 in Fig. 4.14f. Square markers indicate 24 hour intervals and red circles are SO_2 point sources as in Fig. 4.3.

in the FT less than 100 m above cloud top at 80°W, 20-22°S. The mean concentration of CCN at σ=0.5% during this flight leg was 1100 cm^{-3} indicating an unusually polluted FT over the remote SEP.

The model produces a hook qualitatively similar to, but less extensive than that observed (Fig. 4.14f). It captures a hook of large FT CCN concentrations (Fig. 16f), but the CCN concentration at 80°W is much smaller than measured. Again, model back trajectories indicate that much of the FT transport is composed of Santiago region emissions (Fig. 4.15b). However, Fig. 4.15b also shows that some model 3D back trajectories from the hook correspond to offshore flow at 27-28°S in the FT, so sources north of Santiago may also contribute to the polluted air over the remote ocean. From both sources, high concentrations

of SO_2 and CCN advect upward and southward, then offshore, but less far south than in Hook1. 2D MBL model back trajectories encounter the coast just to the south of the Santiago region, so MBL transport cannot be ruled out as a hook source of CCN in this case. However, over the four days of transport from the coast to the remote ocean, aerosol number loss processes such as precipitation and cloud processing reduce the likelihood of it being the sole source of hook CCN.

As with the other hook cases, a high pressure system shifted southward and eastward from its climatological mean occurs. The high stays close the coast south of Santiago for several days, contributing to Hook3 and, subsequently, a much stronger hook on 19 Nov. The upper level flow is not characterized by the same system noted in Hook1 and Hook2, but a near-shore trough does allow for upper level offshore flow. Polluted FT plumes contributing to Hook3 travel north of 24°S before westward advection past 75°W (Fig. 4.15b), far enough away from the southward shifted subtropical high to experience weaker subsidence than average. Thus, FT polluted layers that have not yet been entrained into the MBL are observed on RF14 lying above the remote ocean cloud. In the model a plume of high CCN concentration at 2 km altitude at 28°S, 72.5°W on 6 UTC 14 Nov does not intersect the MBL until it reaches 22°S, 82°W on 15 November at 12 UTC. This took 12 hours longer to subside to the inversion and traveled about 3.5 degrees longitude further than the Hook1 trajectory (Figure 4.12b, 4.12c) subsidence from near 2 km to the inversion (over a similar latitude change). This weaker subsidence allows for greater westward FT transport than other situations of offshore flow at 2 km. Nevertheless, Hook1 extends further west than Hook3 in the model because of the deeper layer of FT offshore transport.

4.5.3 Commonalities between Hooks

Although the model does not reproduce all three major observed N_d hooks in the REx period well, it does simulate FT offshore flow of polluted plumes of CCN and SO_2 from the Santiago region and as far south as 35.5°S in the model. The model does not simulate FT offshore flow this far south at any time during REx besides the 2-3 days preceding the three hook cases. Hence, it suggests that FT flow off the Chilean coast near or just south of Santiago is

an important component of hook formation during REx. Emissions at other latitudes and altitudes may contribute to the observed hook in some cases, but Santiago region emissions are key. Santiago-area pollution plumes experience some lofting (to altitudes of 3-6 km) and southward transport in all three cases, especially Hook1, before being advected offshore, after which they subside and are entrained into the MBL, contributing to the hook feature in N_d. All three hooks also have evidence of MBL transport of regions of elevated N_d after the FT source has been depleted. Although in some cases direct MBL transport from coastal regions may substantially contribute to hook CCN (especially Hook2), entrainment appears key to supporting offshore high N_d. In summary, remote ocean N_d hooks appear strongly linked to FT transport of Santiago region emissions, though more cases would need to be studied to gain absolute confidence in this association.

4.6 Hook conclusions

Periodic free-tropospheric transport of anthropogenic emissions to the typically stratocumulus-dominated pristine SEP remote ocean produces strong AIEs and a large source of cloud droplet concentration (N_d) variability. Stratocumulus N_d variability over the remote SEP is modulated by the passage of hooks – bands or arcs of enhanced N_d (typically >100 cm^{-3}) extending from close to the coast for up to 1500 km offshore. The mean MBL accumulation mode number concentration was measured by VOCALS to be ∼150 cm^{-3} in the MBL over the remote ocean west of 80°W along 20°S (Allen et al., 2011), with mean N_d values below 100 cm^{-3}. To achieve the 250-350 cm^{-3} N_d observed in hooks without a supply of additional CCN would require unrealistically large supersaturation to activate all of the accumulation mode and a substantial number of small Aitken mode particles. Within a developing hook, supersaturation changes driven by precipitation impacts on TKE do appear to influence the magnitude of the N_d increase substantially as shown in this paper, but this is a secondary effect compared with the introduction of high CCN concentrations in the remote MBL.

In this study, the WRF-Chem model is run for the month-long VOCALS-REx period (15 Oct to 16 Nov, 2008), during which three major hook events were identified. The strongest of the three is reproduced quite faithfully by the model (except for a significant timing error)

and is used to investigate the formation, evolution, decay and possible radiative impacts of a hook. Trajectory analysis indicates the aerosols responsible for this feature were primarily transported in the lower free troposphere above the inversion from south of Santiago before entraining into the MBL and enhancing cloud droplet concentration ∼1000 km offshore to levels more typical of the near-shore polluted region. This mechanism likely explains many of the hook features observed over the SEP and similar features may be occurring over other subtropical eastern ocean regions. Advection of coastal pollution within the MBL appears to be more important for one of the other two hook events, though it is unlikely facing loss processes of precipitation and dilution that MBL advection can lead to remote ocean hooks without some additional FT support supplying CCN to the MBL along the way. Oceanic DMS emissions have noticeable secondary effects on simulated hooks. Differences between the observed hooks and their simulated counterparts suggest that the detailed location and strength of hooks is sensitive to various possible sources of error, including subtle differences in the wind field and vertical mixing, especially on the slopes of the Andes, the assumed emissions, and both the free-tropospheric and boundary layer processing of aerosol.

The first hook event experiences a significant increase in N_{d} over the remote ocean that cannot be explained by MBL advection and model results indicate entrainment of FT aerosols is responsible. Albedo at the peak of the hook is larger than a simulation without anthropogenic aerosols, which is due largely to the Twomey effect though secondary AIEs enhance this the Twomey effect and contribute 30-50% of the net albedo change. Albedo also increases during hook development primarily due to aerosol changes, but an increase in stability and weakening subsidence associated with the coincident meteorology is also noted in the simulation without anthropogenic aerosols and explains part of the albedo change.

Synoptic meteorological conditions and their interactions with the Andes topography are important to the FT CCN transport that leads to hook formation. Subsidence and the increase in MBL depth offshore often limit the westward reach of anthropogenic aerosols in the FT, so high concentrations of CCN in the remote FT must originate from significant lofting up the Andes prior to offshore flow or weak subsidence during offshore transport. However, the required westward flow is associated with the north end of the subtropical high and does not extend to heights of more than 5-6 km at most. Other meteorological scenarios

may lead to offshore transport, but the ones during REx all coincided with a southeastward shift of the subtropical high associated with an upper-tropospheric trough approaching the Chilean coast from the west, causing changes to the normal direction of transport (Rahn and Garreaud, 2010a). Whether the transport is in the FT or the MBL, hook events require meteorologically anomalous offshore flow driven by changes in the strength and location of the subtropical high and a method to preserve or even enhance high CCN concentrations in the MBL during passage to the remote region.

Although there is general agreement between the observations and model for strong hook events, the model fails to match exactly the timing and extent of any of the hook features studied here. Because they affect the variability of N_{d} and therefore AIEs over the remote ocean and are so difficult to reproduce with a model, hooks represent a significant challenge in quantifying regional AIEs. The difficulty simulating them, even with a regional model with relatively high resolution, reflects the very precise sequence of meteorological conditions must occur for these narrow bands of elevated offshore transport to bring aerosols to the right place at the right time. In addition, to capture the impact of a hook on radiation the model must accurately represent the aerosol processing within the MBL that adds aerosol mass from DMS-produced SO_2, in addition to turbulent and activation processes within stratocumulus. Correctly capturing and quantifying the variability in AIEs thus represents a formidable challenge.

Chapter 5

PARSING AEROSOL INDIRECT EFFECTS

Chapter 4 identified and documented a mechanism for continental aerosol transport to the remote southeastern Pacific and showed how this manifests as hook-shaped regions of large cloud droplet concentration extending offshore. In this chapter we estimate the overall magnitude of the aerosol indirect effects (AIEs) on albedo over the southeastern Pacific (SEP) due to anthropogenic aerosols using WRF-Chem simulations over the entire REx period. Specific foci are the relative contribution of the Twomey effect and secondary aerosol impacts on cloud macrophysical properties, how these vary spatially and temporally, and how we can quantify uncertainties in the derived AIEs.

The enhancement in albedo following a hook (Chapter 4) is significant from a purely statistical standpoint, but not addressed in the analysis is how unusual this change compares to the typical variability of remote ocean albedo and AIEs nearer to the South American coast. Do hook events represent periods of especially large AIEs compared to mean conditions near anthropogenic sources and offshore? Given the significant but weak contribution of N_{d} variability to albedo variability (Chapter 2), are aerosol impacts on albedo sufficiently strong to be distinguished from the meteorological variability between simulations? What is the temporal variability in the strength of AIEs that contributes to the mean magnitude? We identify a relatively simple method for the attribution of AIEs to changes in cloud droplet concentration, liquid water path and cloud cover using WRF-Chem simulations with and without anthropogenic aerosols. Similar to the observational study in Chapter 2, we distinguish between microphysical and macrophysical influences on AIE. We use this method in the model to investigate the time variability in AIEs in the SEP over the entire REx period and assess the temporal and spatial scales of averaging needed for aerosol effects to become statistically significant above meteorological noise.

5.1 Motivation: Approaches to AIEs

The radiative effect of aerosols from anthropogenic sources contributes to the total human-induced component of climate change, which is highly uncertain. A suite of model studies quantify the magnitude of the 1st AIE for use in the Intergovernmental Panel on Climate Change (IPCC), but the variety of cloud parameterizations and cloud-climate feedbacks within different models leads to an estimate of the 1st AIE in the broad range of 0.25 to 1.75 Wm^{-2}. This ignores 2nd AIEs, which vary even more broadly across models and widen this uncertainty range. Many models compare a simulation with anthropogenic sources to one that represents predindustrial times either with anthropogenic sources or using a prognostic droplet concentration computed from different sulfate concentrations. This is a common method employed by GCMs to estimate the AIEs (e.g. Penner et al., 2006; Lohmann et al., 2007), though in some models the anthropogenic contribution estimate is obtained by turning on and off parameterizations that link aerosol load to cloud properties (e.g. Wang et al., 2010) rather than changing the aerosol load. In some models aerosols are not interactive and a Twomey effect estimate is obtained by computing the change in TOA radiative forcing due to different prescribed aerosol concentrations (e.g. Boucher and Lohmann, 1995). Over time the GCMs have added representation of more processes (such as vegetation, chemistry, etc.) and increased resolution. While including these processes may improve the estimate of AIE, they also increase the uncertainty. Quass et al. (2009) synthesizes the problem of quantifying AIEs and recommends a radiative flux perturbation approach, which is now being adopted by the IPCC. This effectively lumps all of the AIEs together, which at least includes 2nd AIEs as well. But, this method ignores distinctions between the microphysical perturbation and the macrophysical responses which are essential elements of the problem that occur on different scales and warrant separation in analysis. Most modeling of aerosol-cloud interactions focuses upon either high-resolution idealized simulations on small domains of a few tens of km, or upon global simulations at very low resolution. Here, we use a regional model with real aerosol and aerosol precursor sources forced by observed meteorology but with a resolution (14 km) sufficient to capture transport mechanisms that global models cannot resolve.

5.2 Motivation: Cloud sensitivity to anthropogenic aerosols

We investigate AIEs as an increase in aerosol loading from preindustrial times to 2008 over the SEP. We compare a simulation with anthropogenic emissions and oceanic and volcanic natural emissions (Anth) to a simulation with only natural emissions (NoAnth). This is carried out for a month-long period (15 Oct to 15 Nov, 2008). A detailed description of these simulations is provided in Chapter 3. The time-mean Anth-NoAnth differences in model top of atmosphere albedo (α^{TOA}), droplet concentration ($N_{\rm d}$) and liquid water path ($L_{\rm p}$) are spatially correlated and are stronger near the coast where anthropogenic aerosols exert influence (Fig 5.1a,b,c). Both the microphysical property $N_{\rm d}$ and the macrophysical property $L_{\rm p}$ are larger in the simulation with more aerosols, which suggest that increases in condensate in the model are acting to add to the Twomey effect in the time mean. However, cloud fraction differences ($f_{\rm c}$) show weak incoherent correlation with the α^{TOA} difference (Fig. 5.1d). In the stratocumulus region cloud cover is extensive due to large scale subsidence and cold advection associated with the subtropical high (George and Wood, 2010). In our simulations at least, with binary $f_{\rm c}$ (0 or 1) at individual gridpoints, $f_{\rm c}$ is not particularly sensitive to aerosol loading. The domain mean Anth simulation cloud fraction (f_c^A) is smaller than NoAnth cloud fraction (f_c^N) by only 1-2% (Table 5.1).

Although there are clear increases in $N_{\rm d}$ with aerosol loading in the coastal zone, the distribution of $N_{\rm d}$ on a given day (Fig. 5.2a) shows that it is not unusual for the droplet concentration in NoAnth (N_d^N) to exceed that in Anth (N_d^A). This occurs for 20% of grid boxes/timesteps. $L_{\rm p}$ differences are also highly variable and deviate from the ($L_p^A = L_p^N$) line (Fig. 5.2b). However, despite a significant domain-mean difference between L_p^A and L_p^N (Table 5.1), it is not easy to discern a systematic deviation from the $L_p^A = L_p^N$ in Fig.5.2b. The combined effect of $N_{\rm d}$ and $L_{\rm p}$ changes is a distribution of cloud albedo differences (computation detailed in section 5.2.1) centered just above zero (Fig. 5.2c) but with variability at the individual model grid-box level that greatly exceeds that of the mean differences (Table 5.1). Thus on any particular day the difference between Anth and NoAnth model albedo is generally a small signal and is nearly obscured by meteorological noise. The speckled nature of the offshore Anth-NoAnth cloud property differences (Fig. 5.1) suggests

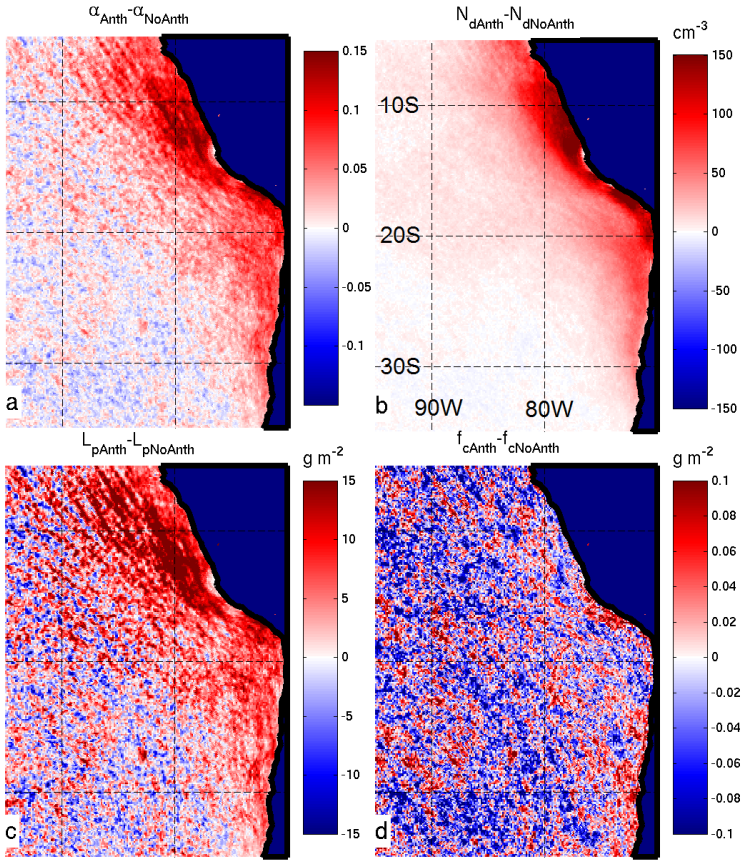

Figure 5.1: Anth-NoAnth REx mean differences in (a) α, (b) N_d, (c) L_p and (d) f_c due to anthropogenic aerosols.

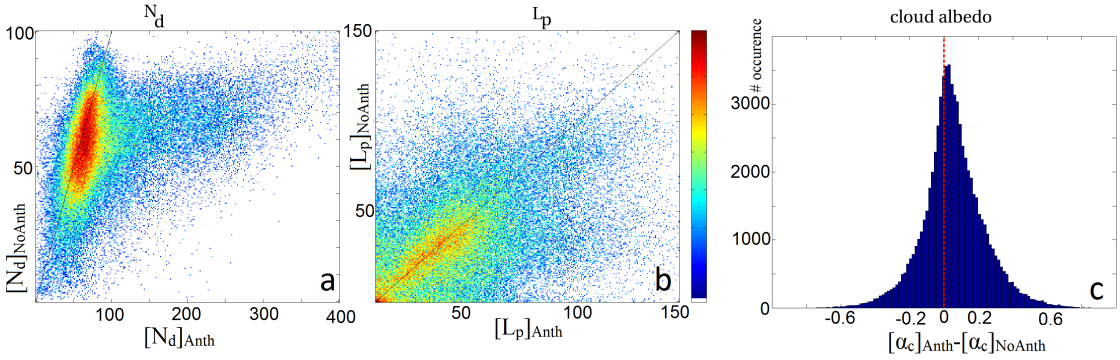

Figure 5.2: A sample day (15 October) density scatter plot of Anth v NoAnth (a) N_d and (b) L_p. Color indicates density of points. (c) shows the distribution of $\alpha_c^A - \alpha_c^N$ on this day for points with $f_c^A = f_c^N = 1$.

that even one full month of averaging does not remove all meteorological noise between Anth and NoAnth simulations. This point will be expanded upon later in this chapter (section 5.2.3) and meteorological noise quantified using an additional model simulation. Given these apparent correlations between clouds upon increased aerosol loading, and that this model reasonably reproduces the mean state and variability of key cloud parameters (N_{d}, L_{p}, f_{c}) and their contributions to albedo variability (see Chapter 3), further investigation of how they contribute to the AIE is warranted.

Table 5.1: Domain-REx mean Anth-NoAnth difference with mean Anth quantity in parenthesis. The Whole domain is 70-95°W, 5-35°S, and the Near-Coast is the region shown in Figure 5.17. Also shown is the mean difference between Anth and an ensemble simulation initialized a day later (see text). α^T = model top of atmosphere albedo.

Domain	$\Delta\alpha^T(\bar{\alpha^T})$	$\Delta\alpha(\bar{\alpha})$	$\Delta\alpha_c(\bar{\alpha_c})$	$\Delta N_d(\bar{N_d})$	$\Delta L_p(\bar{L_p})$	$\Delta f_c(\bar{f_c})$
Whole	0.024(0.26)	0.025(0.27)	0.033(0.32)	28(62)	4.3(39)	-0.011(0.63)
Near-Coast	0.052(0.29)	0.056(0.33)	0.07(0.38)	56(94)	9.1(43)	-0.0081(0.75)
Ensemble	-0.0004	-0.0015	0.0022	0.3	0.5	-0.0088

5.2.1 WRF-Chem AIEs

AIE definition in WRF-Chem

The model configuration used in this study includes representation of the Twomey effect (first AIE) and also aerosol impacts on cloud macrophysical properties (2nd AIEs). In the simulations used here, all processes occur together so that the difference between the Anth and NoAnth simulation albedos represents the sum total of the aerosol indirect effects, direct effects and semi-direct effects included in the model. Separation of the AIE into separate impacts of microphysics (N_{d}), and macrophysics (L_{p} and f_{c}), however, is desirable as it provides important insight into the key processes that produce the overall AIEs. We provide a way to do this using the simple albedo proxy first discussed and applied to satellite data in Chapter 2. The difference between Anth and NoAnth albedo reconstructed using

this method from cloud properties then yields an estimate of the total AIE, as it does not take into account direct and semi-direct effects. Thus the contribution of microphysical and macrophysical cloud variables to this albedo proxy provides estimates of the relative contributions of the 1st and 2nd AIEs to the total AIE. We define the total AIE in the model as the difference in reconstructed albedo between the Anth and NoAnth simulations.

Aerosol indirect effect mechanisms in WRF-Chem

Although any model is limited by the series of parameterizations it employs, exploring how cloud microphysical and macrophysical properties respond to changes in aerosols in a model can provide useful insight into the processes controlling how real clouds behave. The first indirect effect occurs through the impact of aerosols on N_{d} (simulated via Abdul-Razzak and Ghan (2000) cloud activation) on the Goddard shortwave radiation scheme, which incorporates the change to droplet effective radius and cloud optical depth (Gustafson et al., 2007). By definition, the first indirect effect is the change in albedo associated solely with the microphysical changes in N_{d} with the cloud macrophysical variables held constant. The Lin microphysics scheme with the Liu et al. (2005) autoconversion parameterization permits a 2nd AIE by which N_{d} reduces the autoconversion rate and suppresses precipitation as postulated by Albrecht (1989). This autoconversion scheme based on Liu and Daum (2004) tests well against observational estimates of autoconversion processes (Wood, 2005). The aerosol-induced change in N_{d} (Fig. 5.1 and Table 5.1) demonstrates the importance of the 1st AIE in the model, whereas the spatial correlation between the positive change in L_{p} (Fig. 5.1c) and negative change in surface precipitation (Fig. 5.3a) suggest that in the region affected by anthropogenic aerosol (Fig. 5.3c) in the mean, precipitation is suppressed by 30-50+% and L_{p} is likely enhanced as a consequence given the model parameterizations to implement this effect.

Other known secondary effects occur in the model as a result of the Twomey effect and effects on cloud macrophysical properties were not purposefully included to represent AIEs. An impact of smaller droplets and suppressed precipitation leads to a reduction in latent heat release at the cloud level and below-cloud evaporative cooling. Drizzle tends to promote

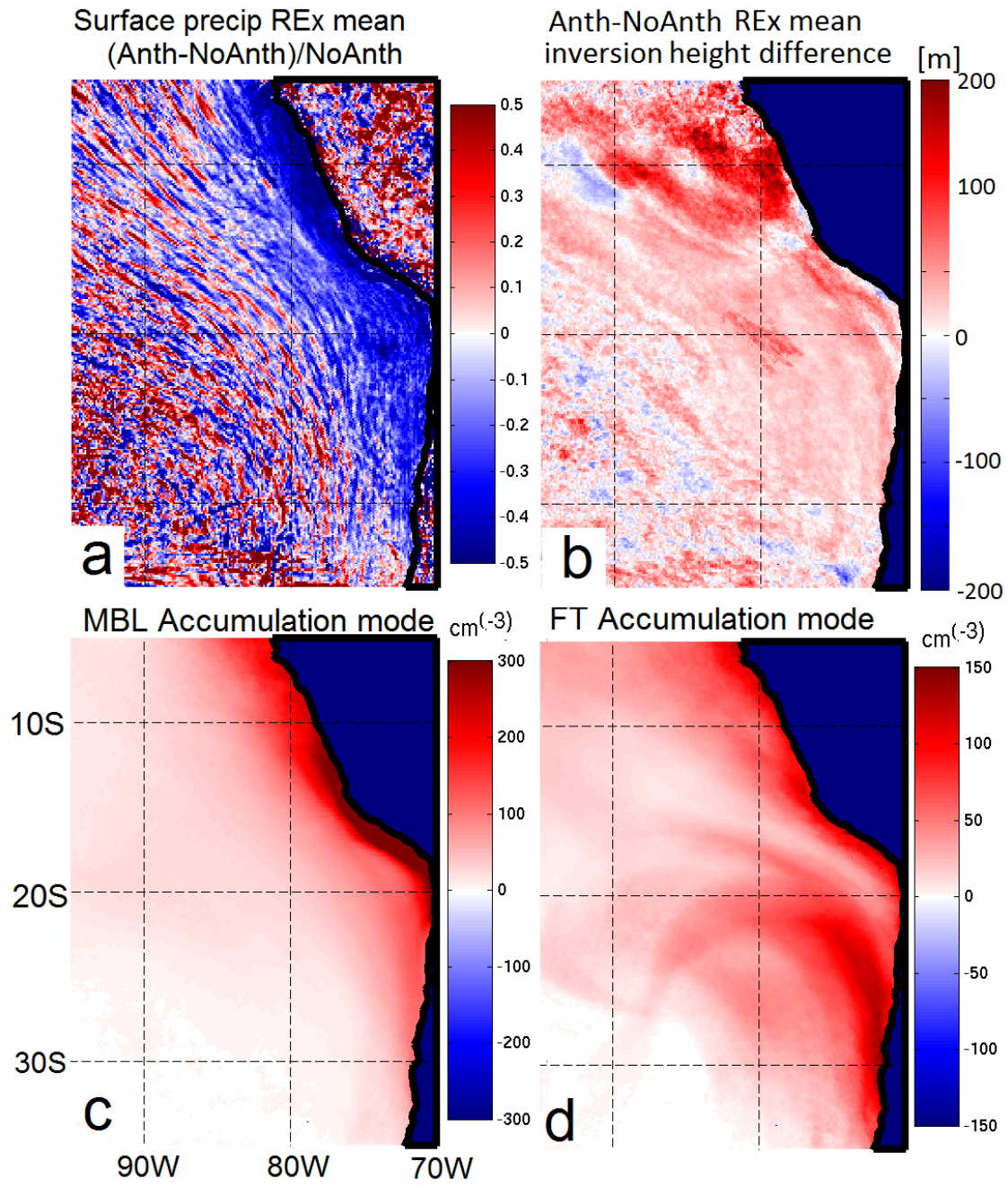

Figure 5.3: REx mean difference between Anth and NoAnth simulations;(a) The relative difference in surface precipitation. (b)Net difference in inversion height. Inversion height is determined in the model as the minimum height at which relative humidity is smaller than 40%. (c) and (d) are accumulation mode aerosol concentration differences in the MBL and FT.

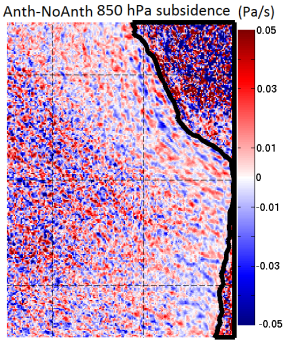

Figure 5.4: REx mean difference between Anth and NoAnth simulations subsidence rate at 850 hPa (units are Pas^{-1})

a reduction in turbulence (Stevens et al., 1998) and thus cloud top entrainment (Ackerman et al., 2004; Wood 2007). Precipitation can lead to an increase in the entrainment rate, as well as a redistribution of energy in the PBL described in Stevens et al. (1998) as the potential buoyancy argument. Both of these processes can affect L_{p}. These effects are permitted in the simulation because the UWPBL scheme explicitly incorporates impacts of buoyancy on entrainment (Bretherton and Park, 2009) and WRF-Chem simulates evaporative effects (Chapman et al., 2009), and releases aerosol particles to the interstitial phase upon evaporation. Figure 5.3b shows a REx mean difference in inversion height between the Anth and NoAnth simulations of 50 m over much of the SEP stratocumulus region, and this exceeds 200 m downstream of Lima (although in this simulation Lima emissions are reduced, downslope offshore transport of La Oroya smelter emissions also influence this region). Outside of the main region of stratocumulus in the southwest part of the domain and away from the influence of anthropogenic sources (see Fig. 1.1 and 5.3c,d), the inversion height difference is spatially variable with pockets of negative and positive differences (due to meteorological noise, as described in previous section and to be explored further in section 5.2.3). The coherent stratocumulus inversion height increase with anthropogenic aerosols is caused by enhanced entrainment rates brought about by precipitation suppression as described above, as the mean large scale subsidence does not differ between simulations over such a large area (see Fig. 5.4). Regardless of the mechanisms by which anthropogenic aerosols lead to

a change in inversion height, this change is clear evidence that the dynamics of the marine boundary layer responds to the AIEs in the model and likely affect the magnitude of AIEs through previously hypothesized avenues.

Some processes that this version of the model does not represent can also potentially affect the magnitude of the AIE, so the particular magnitude we show is subject to some uncertainty. These additional effects have not yet been shown to significantly alter net AIEs in large scale models because they involve physical interactions at the subgrid scale that are difficult to represent explicitly (Stevens and Feingold, 2009). We cannot rule out the possibility that these effects have first order impacts on the magnitude of the AIEs, but we necessarily make the assumption here that these would likely induce small perturbations to our results. One such process unaccounted for is the increase in droplet dispersion due to an increase in aerosol loading (Liu and Daum, 2002), which may reduce the strength of the Twomey effect (e.g. Liu et al., 2008). Also, for increases in vertical velocity, N_{d} increases while the droplet dispersion decreases (Lu et al., 2012), another example of dynamical responses complicating interpretation of aerosol indirect effects. This WRF-Chem simulation does not incorporate changes in droplet dispersion nor aerosol particle dispersion. The modal aerosol standard deviation is held constant and so feedbacks involving the 2nd moment of the aerosol size distribution are not well represented.

Also, cloud droplet sedimentation processes are not included in the microphysics scheme we use. Large-eddy simulation (LES) modeling of stratocumulus (e.g. Ackerman et al., 2004, Bretherton et al., 2007) has demonstrated that reduced sedimentation due to increased N_{d} increases the cloud top entrainment rate and thus dries out the MBL, reducing L_{p}. Greater sedimentation discourages sinking air by removing liquid droplets from the entrainment zone and thus reducing the magnitude of evaporative cooling. This in turn reduces entrainment and increases L_{p}. Smaller droplets associated with the Twomey effect inhibit sedimentation, and thus offset the increase in L_{p} associated with the Albrecht effect. Yang et al. (2012) notes an increase in entrainment rate into the MBL in WRF-Chem due to an increase in aerosol loading. They use a microphysics scheme that does parameterize the effects of cloud droplet sedimentation but the changes in entrainment rate are due to both the potential buoyancy effect and the sedimentation effect. Although they use a sensitivity study to

attribute most of the increase in cloud top height to changes in entrainment induced by sedimentation differences, it is not clear how important cloud droplet sedimentation induced cloud top height changes is to the net AIE magnitude. No published studies exist showing a significant impact of this process on AIEs and an experimental run with CAM showed negligible impact of this process on radiation (personal correspondence, C.S. Bretherton).

Although the simulations presented in this study cannot explore the intricacies of the 2nd AIE fully, to the extent the model reproduces observed cloud, aerosol and albedo variability well WRF-Chem can be used to help us better understand how anthropogenic aerosols affect the radiative budget in nature in the presence of convolved dynamical mechanisms and aerosol-related impacts on the radiative forcing.

Calculation of albedo and AIE in WRF-Chem

Although the model provides outgoing shortwave radiation from which top of atmosphere albedo is computed, we intend to investigate the contributions of cloud parameter (f_c, N_d, Lc) components on albedo. Thus defining a reconstructed albedo proxy as a function of f_c and cloud albedo, α_c in similar manner as the MODIS (Chapter 2) analysis is useful. Cloud albedo is computed from the delta-Eddington method as a function of solar zenith angle and optical depth (τ; George and Wood, 2010). The τ is computed from L_p and N_d as in Chapter 2:

$$\tau = C\mathscr{N}\mathscr{L} \tag{5.1}$$

where C=$\left[\frac{9}{5}\frac{1}{\rho_w K^{2/5}}\right]^{5/6}$=0.2303 $\mathrm{m}^{8/3}\,\mathrm{kg}^{-5/6}$ is effectively a constant (Wood and Hartmann, 2006), $\mathscr{N}=N_d^{1/3}$, and $\mathscr{L} = L_p^{5/6}$.

Our proxy albedo α is computed as:

$$\alpha = f_c\alpha_c + (1 - f_c)\alpha_{clear} \tag{5.2}$$

where α_{clear} is the albedo over the ocean when no cloud is present. We assume this quantity is 0.1 in accordance with satellite broadband radiometric observations (Bony et al., 1992).

When comparing albedo across simulations or in different locations we show primarily the weighted daily mean albedo that takes into account the solar zenith angle change over a whole day. For purposes of comparing to MODIS Terra satellite data, 15 UTC is the most appropriate time for a snapshot comparison, but a weighted daily average is more representative of the actual radiative effect and removes the impact of changing local time for a given UTC time across the 25° longitude span of the domain. A potential problem with a diurnal weighted albedo is that the delta-Eddington method for cloud albedo computation is subject to considerable errors for solar zenith angle (SZA)$>$ 60°. However, these cases occur at times that are weighted the smallest in an irrandiance weighted average (using the cos(SZA)) and including all times during the day worsens the comparison with top of atmosphere diurnal weighted albedo by less than 3% (not shown).

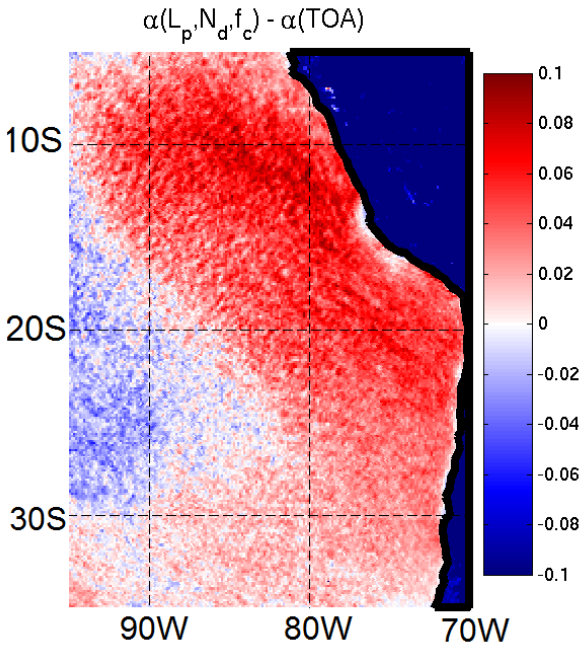

Figure 5.5: Diurnal-weighted REx mean difference in model top of atmosphere albedo and the albedo proxy computed from f_c, L_p and N_d.

The albedo proxy method used for the MODIS analysis (Chapter 2) poorly handles optically thin clouds because the delta-Eddington method results in errors for $\tau < 0.9$ (King

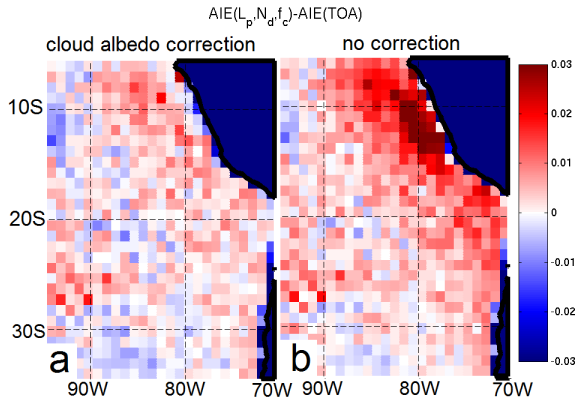

Figure 5.6: REx mean total difference between AIE computed from albedo proxy (as a function of f_c, L_p and N_d) and top of model atmosphere AIE. (a) AIE difference using modified albedo proxy to account for optically thin clouds. (b) AIE difference without adjusting the cloud albedo to account for thin clouds. The $0.125 \times 0.125°$ model resolution has been regridded to $1 \times 1°$ here.

and Harshvardhan, 1986). This leads to derived α_c and α values smaller than the assumed marine clear sky albedo for thin clouds. To better account for optically-thin clouds in the model, we apply a simple multiple scattering theory from Bohren and Clothiaux (2006) to compute the total α_c in the presence of cloud as a function of computed α_c and α_{clear}. The correction applied is:

$$\alpha_c^{corrected} = \alpha_c + \alpha_{clear} \frac{(1-\alpha_c)^2}{1-\alpha_c \alpha_{clear}} \tag{5.3}$$

This albedo calculation does not take into account absorption of solar radiation by cloud, horizontal scattering from heterogeneous non-plane-parallel clouds, nor the effect of aerosols between the top of the atmosphere and the cloud (e.g. the direct and semi-direct effects). In the MODIS study, the combined impacts led to a 14% overestimation of albedo compared to CERES observations, and a single correction factor was applied to all data in that analysis. The same biases considered in MODIS apply to the WRF-Chem albedo proxy and, in the cloudier regions in the east of the domain, results in a similar 0.04-0.07 (10-20%) difference between the albedo proxy and albedo derived from the models own radiative transfer code

at the top of the atmosphere (TOA; Fig. 5.5). However, because this bias affects NoAnth and Anth simulations similarly, the discrepancy in total AIE magnitude is small (typically < 0.01; Fig. 5.6a). Not including the correction for optically-thin clouds leads to differences in AIE between using the proxy albedo and the model TOA albedo that are significantly larger and in some near-coast locations more than 3 times larger (Fig. 5.6b). Thus the correction to the albedo formulation to account for optically-thin clouds improves the proxy AIE estimate, which we use exclusively in the rest of the chapter. The agreement between AIE from the albedo proxy and model TOA is excellent not just in the REx mean, but is also generally good in time and space (Fig. 5.7). We are therefore confident that the proxy AIE method is suitable for analysis of the various contributions to the AIE from the different contributing cloud variables.

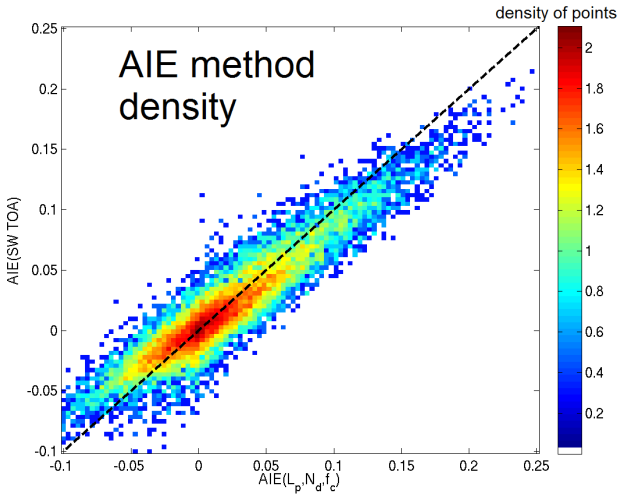

Figure 5.7: REx period SEP time-space scatter plot of AIE computed using the proxy albedo (a function of f_c, L_p and N_d) vs AIE at the TOA. Colors represent log(point density).

5.2.2 Quantifying the contributions of 1st and 2nd AIEs

In this section we explain a few possible approaches to breaking the total model AIE into components associated with the 1st and 2nd effects. We describe the reasons for our choice of method and show the regional time averaged contributions of each AIE category to total

AIE.

Two estimates of the AIE components

To distinguish impacts of microphysical changes (i.e. $N_{\rm d}$ changes) on albedo from changes in the macrophysical variables ($L_{\rm p}$ and $f_{\rm c}$) we create proxy albedo computed using $L_{\rm p}$ and $f_{\rm c}$ from a base simulation and $N_{\rm d}$ from another simulation that has a different aerosol loading. We estimate the Twomey effect initially in a similar manner as Lohmann et al. (2007), that is by subtracting the albedo computed using Anth $L_{\rm p}$ and $f_{\rm c}$ and NoAnth $N_{\rm d}$ from the Anth simulation albedo.

Defining C_{xy} as the cloud proxy albedo derived using $N_{\rm d}$ from simulation x and $L_{\rm p}$ from simulation y. In this study, simulations x and y generally refer to N=NoAnth and A =Anth. The clear sky albedo C_{clear} is again assumed to be a constant value of 0.1. We define the following four albedo proxies that represent different combinations of microphysical and macrophysical variables from the Anth and NoAnth simulations:

$$\alpha_{AA} = \alpha(N_d^A, L_p^A, f_c^A), \tag{5.4}$$

$$\alpha_{NN} = \alpha(N_d^N, L_p^N, f_c^N), \tag{5.5}$$

$$\alpha_{NA} = \alpha(N_d^N, L_p^A, f_c^A), \tag{5.6}$$

$$\alpha_{AN} = \alpha(N_d^A, L_p^N, f_c^N). \tag{5.7}$$

In cases where one simulation is cloudy and the other is clear, the cloud albedo is not computed. Using these, we can then define a Twomey effect T_A as the difference when NoAnth $N_{\rm d}$ is used in place of Anth $N_{\rm d}$ but with the Anth macrophysical properties held constant:

$$T_A = \alpha_{AA} - \alpha_{NA} = f_c^A(C_{AA} - C_{NA}), \text{ from Eq.5.2} \tag{5.8}$$

The 2nd AIE, S_A, is represented as the remaining portion of the total AIE, i.e.

$$S_A = \alpha_{NA} - \alpha_{NN} = f_c^A(C_{NA} - C_{clear}) - f_c^N(C_{NN} - C_{clear}) \tag{5.9}$$

On a gridpoint/timestep basis, the total AIE quantity $\delta = \alpha_{AA} - \alpha_{NN}$ includes meteorological variability between the simulations and thus both T_A and S_A are a combination of AIEs and this variability. Averaged over large enough temporal and spatial scales this random variability is reduced and an aerosol signal becomes significant above this noise. Although the calculation of T_A and S_A can be used to estimate the contribution of microphysics to albedo with constant cloud macrophysical properties, the physical interpretation of AIEs describes first an increase in N_d followed by change in macrophysics as a response. By referencing to the Anth simulation macrophysics, our Twomey effect is a negative change in N_d (a removal of aerosol), so the physical interpretation is not quite the same as Twomey and Albrecht originally envisioned. Thus we can alternately estimate the 1st and 2nd AIEs using the NoAnth as the reference simulation:

$$T_N = \alpha_{AN} - \alpha_{NN} = f_c^N (C_{AN} - C_{NN}) \tag{5.10}$$

$$S_N = \alpha_{AA} - \alpha_{AN} = f_c^A (C_{AA} - C_{clear}) - f_c^N (C_{AN} - C_{clear}) \tag{5.11}$$

The difference between these two methods is due to the choice of reference simulation in which to hold f_c and L_p constant. By construction:

$$\delta = T_A + S_A = T_N + S_N T_A - T_N = S_A - S_N \tag{5.12}$$

Figure 5.8 shows diurnal-weighted REx mean magnitudes of the estimated AIE components **T** and **S**. Although at any given time and location L_p^A is quite different from L_p^N (Fig. 5.2ab), on average over the REx mean these differences average near the one-to-one line. We therefore might expect differences in T_A and T_N to be small when averaged over the entire month. Instead, we see that over most of the domain T_N is negative and T_A is positive, with agreement in sign only near the coast. In general, since N_d^A exceeds or is close to N_d^N most of the time (Fig. 5.2a), the Twomey effect should be positive or negligible most of the time, but here we see strong opposing signs in estimates of the 1st and 2nd AIEs. The strong negative time-mean T_N also makes no physical sense.

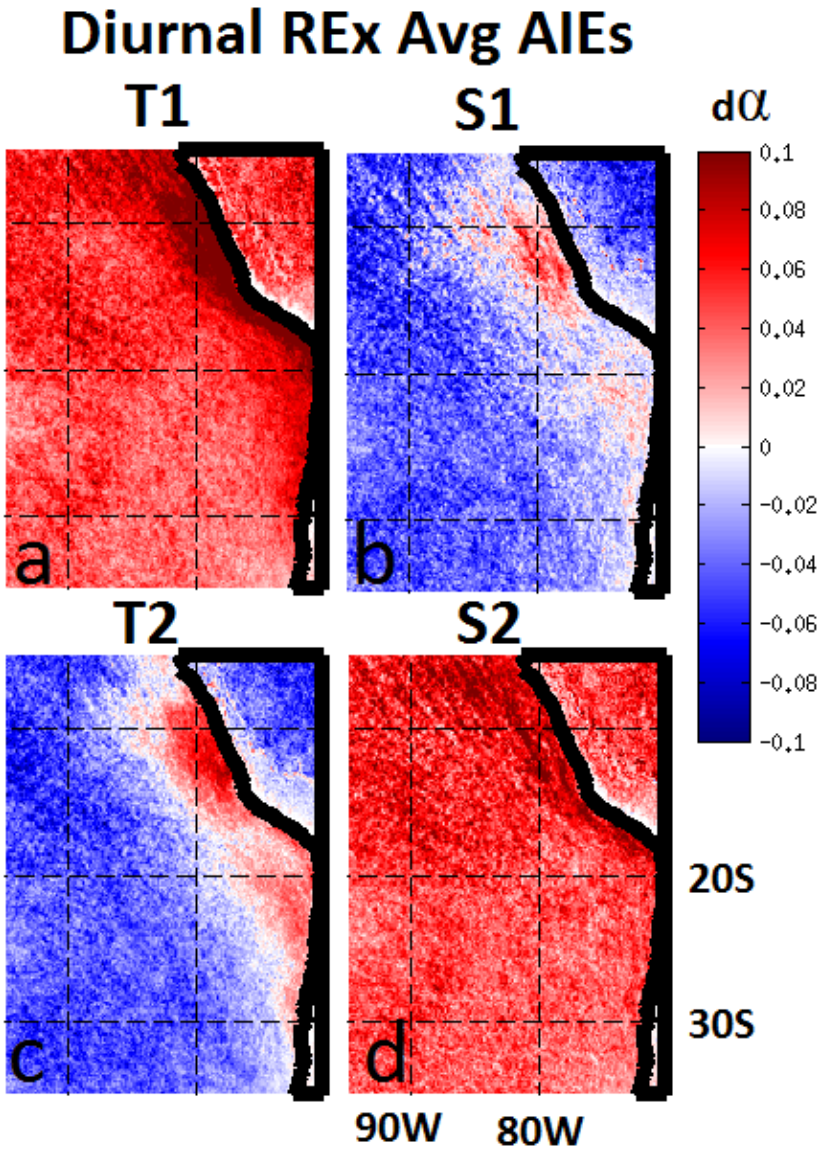

Figure 5.8: REx mean components of total AIE using the Anth simulation as the base case in (a) and (b) to compute the Twomey effect T1 and the secondary AIEs S1. (c) and (d) show this computation using the NoAnth simulation as the base case.

The problem of binary model cloud fraction

The discrepancy between estimates of the Twomey effect, T_A and T_N, is due primarily to the binary nature (0 or 1) of WRF-Chems f_c variable. When both Anth and NoAnth simulation gridpoints are cloudy, estimates of AIEs are distributed fairly symmetrically around the $T_A = T_N$ and $S_A = S_N$ lines (Fig. 5.9). However, if one simulation gridpoint is cloudy and the other is clear (XOR cases), which occurs in 20% of the marine gridpoints during REx, the values of T_A and T_N are extreme and represent not only a change in the microphysics, but also a change in cloudiness, which is defined to be fixed for estimates of the Twomey effect. We note the effect with simple algebra:

If $f_c^N = 0$ and $f_c^A = 1$,

$$T_A = C_{AA} \tag{5.13}$$

$$T_N = 0 \tag{5.14}$$

$$S_A = -C_{clear} < 0 \tag{5.15}$$

$$S_N = (C_{AA}C_{clear}) > 0 \tag{5.16}$$

$$\tag{5.17}$$

If $f_c^N = 1$ and $f_c^A = 0$,

$$T_A = 0 \tag{5.18}$$

$$T_N = -C_{NN} \tag{5.19}$$

$$S_A = -(C_{NN}C_{clear}) < 0 \tag{5.20}$$

$$S_N = C_{clear} > 0 \tag{5.21}$$

$$\tag{5.22}$$

The impact of these cases on the relationship between the two AIE methods (Fig.5.9) is to cause a systematic negative bias in S_A and T_N, and a positive bias in S_N and T_A. This largely explains the strange behavior in the REx mean values (Fig. 5.8).

An instantaneous Twomey effect cannot be defined for the XOR cases. If, at a particular location, Anth is cloudy with a polluted droplet concentration and NoAnth is cloud-free, the change in macrophysics indicates that the computed T_A and T_N do not isolate microphysical impacts alone. However, in this case N_d^A is larger than the normal range of N_d^N, so the Twomey effect cannot be zero. This represents a conundrum. One option is to proceed by labeling these cases undefined and then to compute T_A and T_N only using cases when both simulations are cloudy or cloud-free. However, this will neglect 20% of the data. The enhancement in $N_{\rm d}$ in the cloudy Anth and cloud-free NoAnth cases certainly contributes to the overall Twomey effect, and ignoring it can affect the estimate of total $N_{\rm d}$ enhancement.

Biases in AIE component estimates without binary cloud fraction

One approach is to eliminate or at least heavily reduce the number of XOR cases by averaging cloud properties to a lower resolution. **T** and **S** values derived from albedo computed using $N_{\rm d}$, $L_{\rm p}$ and $f_{\rm c}$ averaged over $1 \times 1^\circ$ areas (64 gridpoints) leads to much closer agreement between T_A and T_N and between S_A and S_N (Fig. 5.10) and a narrowing of the distributions of **T** and **S** values. The reduction in AIE component magnitudes and variability caused by averaging is striking. This type of averaging has occurred in our MODIS estimates of albedo (which estimate T_A and S_A by referencing to an estimate of remote ocean clean $N_{\rm d}$). However, MODIS averages 1 km resolution data to 5 km to derive cloud fraction and the dominant spatial scale of $L_{\rm p}$ variability is 5-50 km (Wood and Hartmann, 2006), so high resolution MODIS data may not have removed the relevant variability in the same way that assuming a 14 km gridbox has to be either completely clear or completely cloudy does. The $1 \times 1^\circ$ data we employ however, is likely missing some macrophysical variability. The difference between T_A and T_N (or S_A and S_N) computed from $1 \times 1^\circ$ data (which is more pronounced near the Peruvian coast) is generally small (< 0.01) but distinct (Fig. 5.11). This means the use of T_A for MODIS Twomey is still be subject to a small bias even when averaging has reduced the impact of XOR cases.

A difference in T_A and T_N exists even if XOR cases are ignored as demonstrated by the scatter plots of T_A vs T_N (Fig. 5.9). Mathematically this is due to the choice of

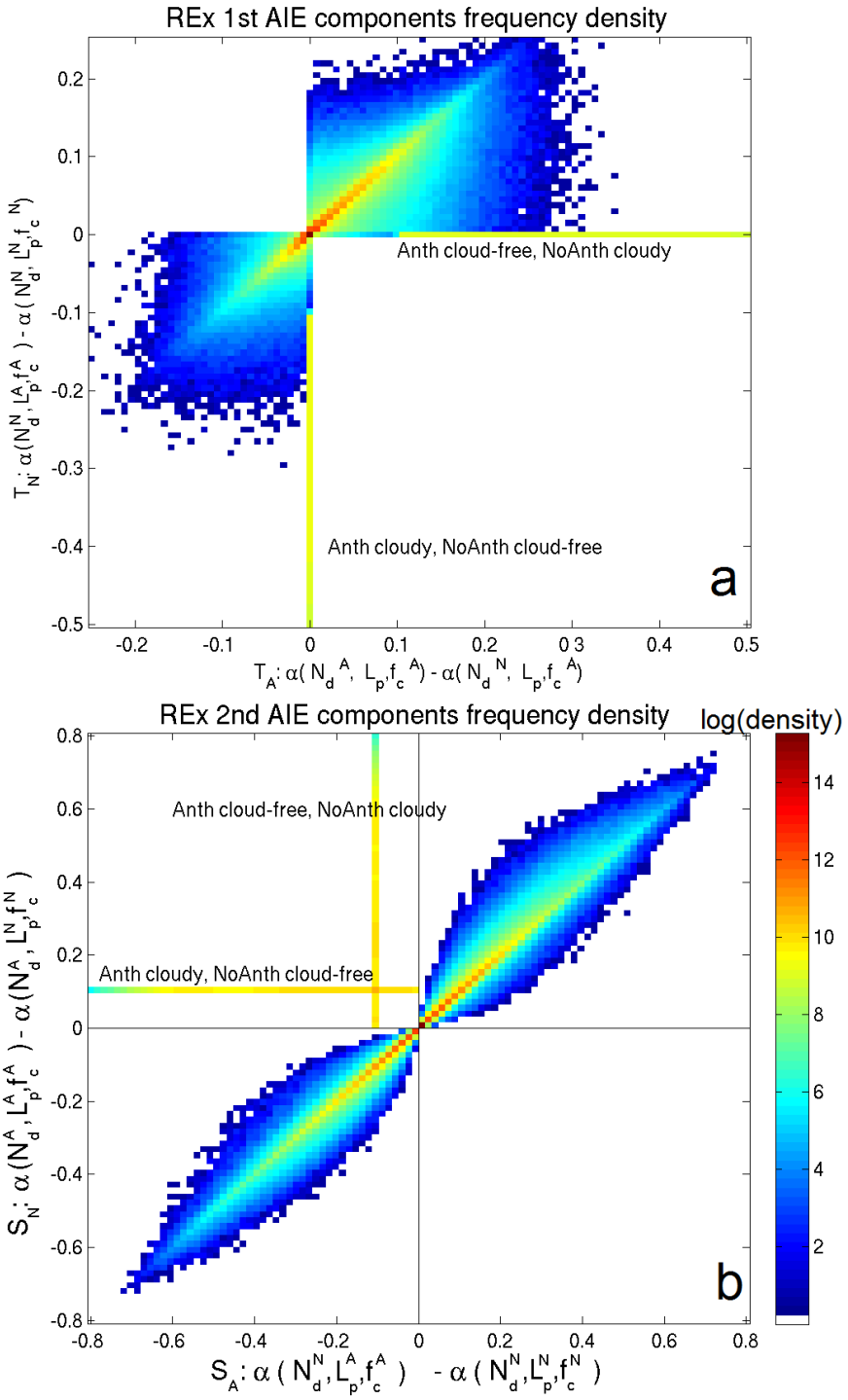

Figure 5.9: Scatterplot of the Twomey effect estimates (T_A vs T_N) and secondary AIEs (S_A vs S_N) in marine SEP over REx period. XOR cases when one simulation is cloudy and the other cloud-free are labeled.

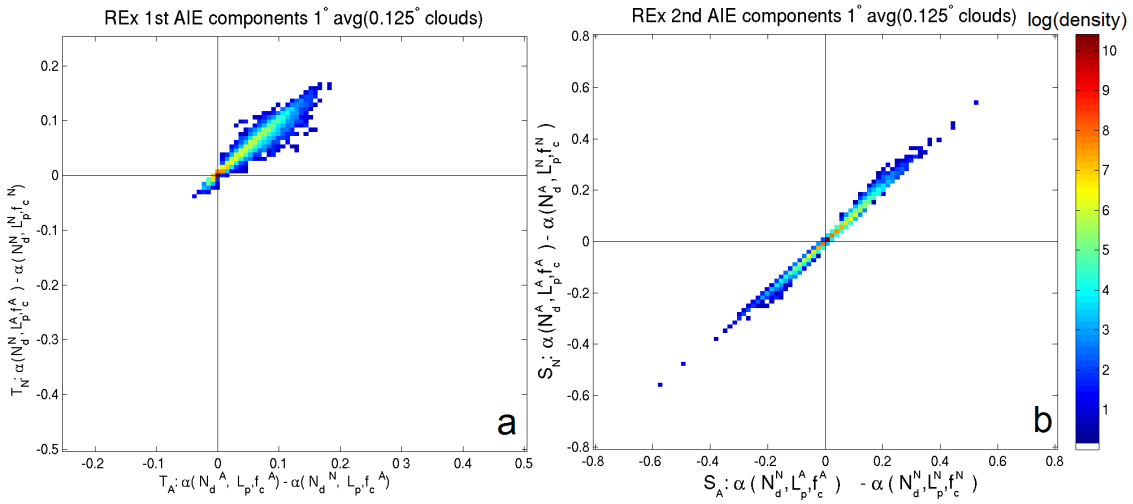

Figure 5.10: Same as Fig. 5.9, but for AIEs computed from $1 \times 1°$ area averages of f_c, L_p and N_d.

constant macrophysical properties. Conceptually it also has to do with the likelihood that the difference in N_d between Anth and NoAnth does not solely represent a difference in aerosol loading/microphysics. The computed Twomey effect includes the effects of feedbacks on N_d due to N_d-induced changes in L_p and f_c. For example, increased N_d may suppress precipitation and therefore increase the lifetime of aerosols leading to even larger N_d than the initial perturbation by increased anthropogenic emissions. One could argue that the Twomey effect should be identified based on the changes in N_d solely due to the introduced aerosols (without feedbacks on aerosols), but in this model scenario it is not possible to isolate this change. We are estimating an effect of integrated cloud susceptibility over a large difference in N_d in a simplified form and T_A and T_N contain biases from the real Twomey effect in opposing directions.

Our estimate of AIE components

The differences between T_A and T_N depend on the complex interaction between changes in L_p, N_d, and f_c between the Anth and NoAnth simulations. When Anth and NoAnth gridboxes are both cloudy (Fig. 5.9) the differences $T_A - T_N$ and $S_A - S_N$ are centered

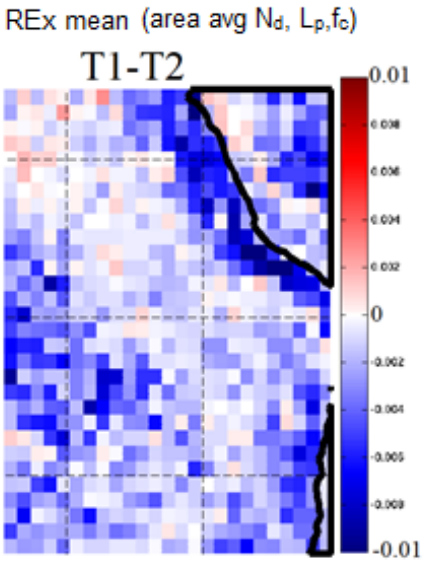

Figure 5.11: Diurnal weighted REx-mean difference between AIE component estimates computed from the $1 \times 1^{\circ}$ area averages of f_{c}, L_{p} and N_{d}.

on 0, that is the scatter plots are very symmetric about the $T_A = T_N$ and $S_A = S_N$ lines. A histogram of $T_A - T_N$ (Fig. 5.12) demonstrates that indeed the differences between the estimates are frequently small (instances of $|T_A - T_N| < 10^{-4}$ not shown because they dominate the distribution) and symmetric around 0. It is thus reasonable to average the estimates of the 1st and 2nd AIEs from the two estimates. Not only does this reduce the bias from choosing either T_A or T_N in cloudy comparisons, but also reduces the impact of XOR cases. The magnitude of the Twomey effect in XOR cases is cut in half (reducing its influence on the total Twomey effect estimate), and this moves the 2nd AIE XOR cases into the same quadrant as the other negative 2nd AIE cases. This produces much more plausible estimates of the AIE components (Fig. 5.13). We thus define the Twomey effect as the mean $\bar{\mathbf{T}}$ of T_A and T_N (i.e. $[T_A + T_N]/2$) and the 2nd AIEs as the mean $\bar{\mathbf{S}}$ of S_A and S_N for the rest of our analysis. These estimates add up to by design, so the comparison of $\bar{\mathbf{T}}$ and $\bar{\mathbf{S}}$ yields the relative contributions of 1st vs 2nd AIEs. This method results in a Twomey effect estimate that is on average over the domain 10% larger than had we ignored

XOR cases before averaging, which indicates the influence of enhanced N_{d}^{A} information that is removed with XOR cases.

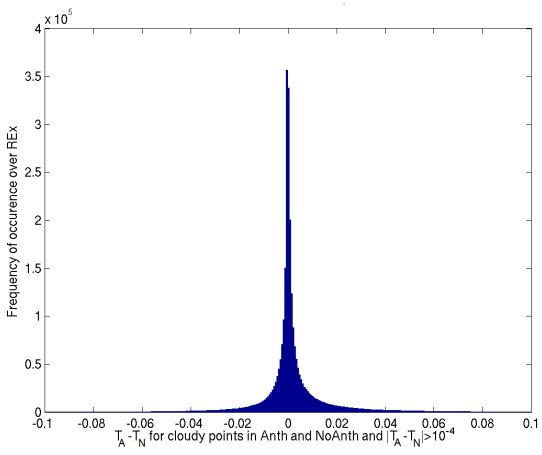

Figure 5.12: The frequency distribution of $T_A - T_N$ from Fig. 5.9 for Anth and NoAnth cloudy cases and for cases of absolute difference $> 10^{-4}$.

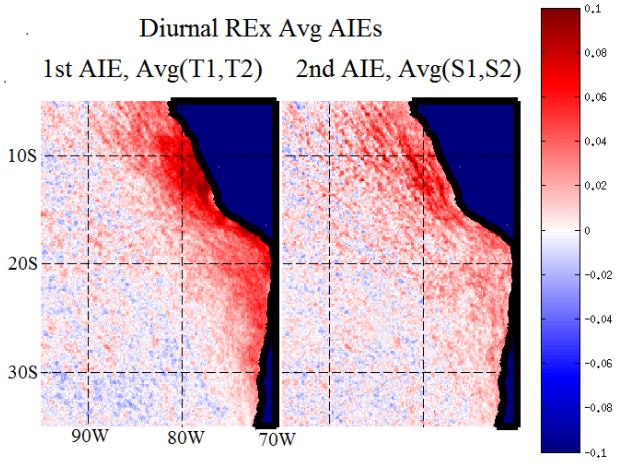

Figure 5.13: Diurnal weighted REx-mean AIE components computed at 0.125° model run resolution by averaging T_A and T_N shown in (a) and S_A and S_N in (b).

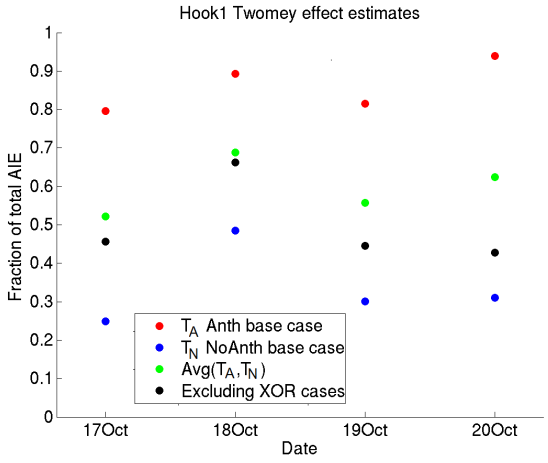

Figure 5.14: Following Hook1 (Chapter 4) the fractional contribution of the Twomey effect to total AIE computed by 4 methods.

Impact of AIE estimate choice on Hook albedo calculation

We refer back to the case of an extended hook of enhanced cloud droplet concentration from Chapter N to demonstrate the impact of our choice of Twomey effect definition. Hooks represent periodic episodes of offshore flow that allow transport of high concentrations of anthropogenic aerosols into the remote ocean, inducing AIEs on albedo. They are thus a good example by which our estimates of AIE contributions can be evaluated. Using $\bar{\mathbf{T}}$ as described in the previous section to account for the first order biases associated with using T_A or T_N the 1st AIE thus contributes about 50-70% of the total AIE following the hook. Including XOR cases has a marked impact and the choice of using T_A or T_N as the 1st AIE leads to opposing conclusions about the relative strength of the 1st and 2nd AIEs associated with the hook (Fig. 5.14). Excluding XOR cases (and averaging the two estimates) lowers the relative importance of the 1st AIE to 40-70% of the total AIE following the hook. But, excluding these cases significantly reduces the estimate of mean albedo because it excludes several points in which Anth is cloudy with large enhanced albedo and NoAnth is cloud-free and is thus not as appropriate of a choice as T. Next we will show that for regions subject to polluted aerosol, this range of contribution is typical for an aerosol response Hook1 then is not a special case of stronger AIEs than is typical over the SEP, but rather is important

because these AIEs occur in a region which generally has little anthropogenic aerosol.

AIE component contributions

We now report the contributions of 1st and 2nd AIEs to the total AIE using the method of averaging estimates described in the previous section.

Spatial variability of AIE component contributions

On average the WRF-Chem simulated 2nd AIE during REx enhances the 1st AIE by a similar but weaker magnitude than the 1st AIE (Fig. 5.15). The relative contribution of the mean 1st AIE to the total AIE in the region affected by anthropogenic aerosols is thus about 50-80%, leaving 20-50% from 2nd AIEs. The regions of largest 2nd AIE are downstream of the main stratocumulus deck over the northwest part of the domain and offshore on the edges of anthropogenic influence, suggestive of the temporal component to secondary AIEs. Thus the region most likely to demonstrate 2nd AIEs is north of 20°S, outside the region sampled by VOCALS aircraft/ships and on the edge of mean anthropogenic influence. Averaged over 15-25°S, the contribution of the 2nd AIE increases offshore in the mean, both due to the temporal delay in the cloud lifetime effect (see Fig. 4.6), but also due to the larger L_{p} offshore associated with a deeper boundary layer (Fig. 5.16). Further offshore the 2nd AIE contribution exceeds the 1st, but the total AIE is much smaller there.

Estimates of AIE contributions using linear theory

To provide a consistency check on the reported contributions of 1st and 2nd AIEs to total AIE we also compute estimates of the contributions of microphysical and macrophysical changes to the magnitude of the AIEs by using a simplified form of the derivative of our albedo proxy equation such that

$$\Delta\alpha \approx \alpha_c \Delta f_c + f_c \Delta\alpha_c \tag{5.23}$$

and

$$\Delta\alpha_c \approx A\Delta N_d + B\Delta L_p \tag{5.24}$$

where $A = \frac{\delta\alpha_c}{\delta\tau}\frac{\delta\tau}{\delta N_d}$ and $B = \frac{\delta\alpha_c}{\delta\tau}\frac{\delta\tau}{\delta L_p}$.

We take domain averages of REx period time mean differences between Anth and NoAnth quantities then to estimate the contributions of each change in cloud property to the change

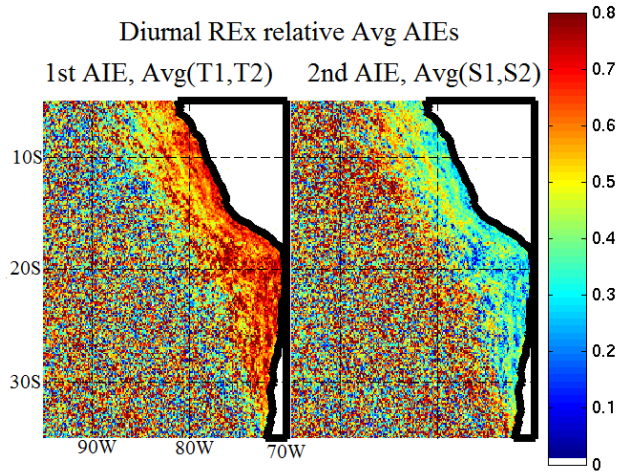

Figure 5.15: Diurnal weighted REx-mean relative contribution of AIE component shown in Fig. 5.13 to the total AIE.

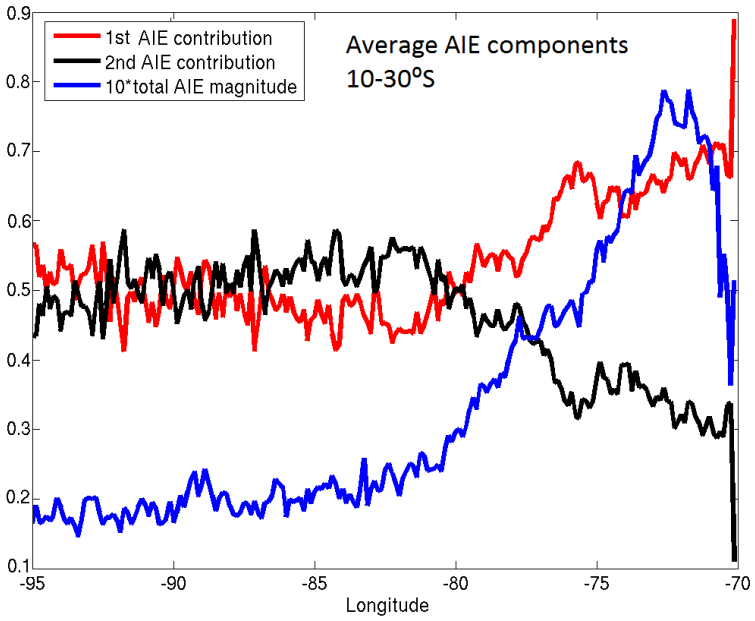

Figure 5.16: Fractional REx-mean AIE components to total AIE averaged over 15-25°S vs longitude. The blue line shows $10 * AIE$ magnitude for reference.

in albedo between simulations. Table 5.1 shows the relevant mean and difference quantities that we need for this calculation. For our purposes here we find the best estimate of mean c using mean N_{d} and L_{p} is

$$\alpha_c = \frac{0.73\tau}{\tau + 7} \tag{5.25}$$

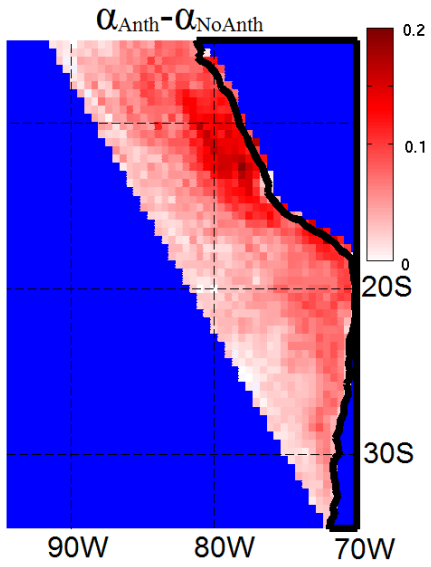

Figure 5.17: The total AIE with regions in blue indicating regions excluded from analysis when analyzing the near-coast domain. This is also the domain used to compute AIE magnitude significance as a function of time and space in Fig. 5.22.

We can then compute the partial derivative of Equations 5.2.1 and 5.2.2 with mean estimates of N_{d} and L_{p} from Table 5.1 to calculate A and B. Using Table 5.1 the predicted $\Delta\alpha$ is 0.025 for the whole SEP domain and 0.049 for the near-coast domain (Fig. 5.17), which is consistent with the top of atmosphere albedo differences (0.024 and 0.052 for respective domains). Using the table values, ΔN_{d} contributes 69(56)% in the whole (near-coast) domain to the $\Delta\alpha$, while the 31(44)% due to macrophysical terms derives from a 42(49)% contribution from L_{p} and a -11(-5)% contribution from f_{c}. This is consistent with the analysis in the previous section. It also suggests that the nonlinearitiesof the system present

in neglected higher order terms (such as covariances between cloud variables) either cancel or are small. The difference $f_c^A - f_c^A$ is small, not significantly larger than the difference in f_c between Anth and an ensemble simulation (Table 5.1) and thus its contribution is indistinguishable from meteorological noise between simulations.Therefore, despite being a nonlinear system, simplified linear estimates of the contributions of AIEs reasonably predict the contributions of N_d and L_p changes, as interpreted as 1st and 2nd AIE contributions.

5.2.3 Spatial and temporal variability

Despite the fact that many studies (both modeling and observational) focus on aerosol-cloud interactions (ACIs), the subtlety of the feedbacks between various physical process at several temporal and spatial scales has prevented a consensus on the optimal method of quantifying ACIs, which contribute to the total AIE. Coarse resolution satellite studies tend to show lower cloud albedo susceptibility (the sensitivity of cloud albedo to changes in N_d at fixed L_p, see Platnick and Twomey, 1994 and Oreopoulos et al., 2008a,b) than do high resolution observational studies. This is due largely to the fact that many observational studies do not put a constraint on L_p in spite of the 1st AIE definition that requires constant macrophysics (McComiskey and Feingold, 2012). Additionally, satellite aerosol loading measurements are not collocated with cloud measurements and this introduces a degree of noise to the ACI estimates. In observational studies where cloud measurements are, on average, further separated in space from aerosol measurements, this leads to weaker ACIs at coarser resolutions (McComiskey and Feingold 2012). In our simulations we often aggregate to coarser scales to purposefully remove small scale meteorological variability between compared simulations, which helps distinguish the total AIE signal from the noise and is not subject to the same problems as observational studies.

Impact of the order of spatial averaging

Although rough linear estimates do a reasonable job of predicting the time-mean AIE contributions, nonlinearities affect our computation of these components when using the full spatially and temporally resolved method described in section 3.2.3 above. In section 3.3.3

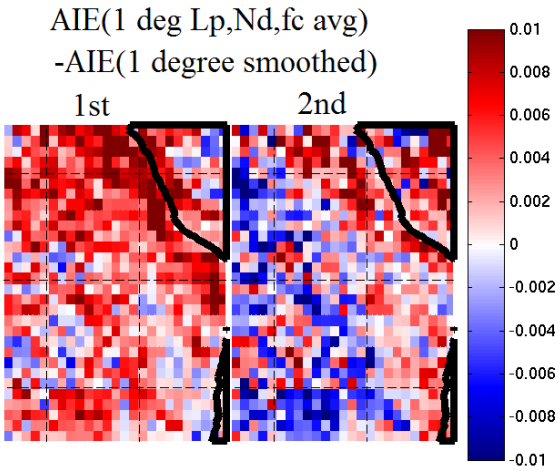

Figure 5.18: Diurnal weighted REx mean difference plots between 1st and 2nd AIEs computed using the $1 \times 1°$ area averages of N_d, L_p and f_c and 0.125° AIEs smoothed to 1°.

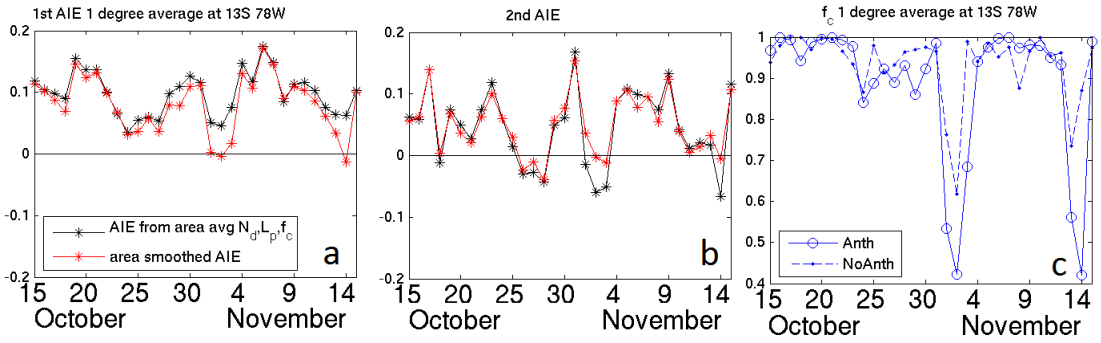

Figure 5.19: Diurnal weighted daily REx time series of (a) 1st and (b) 2nd AIEs computed using the $1 \times 1°$ area averages of N_d, L_p and f_c (black) and 0.125° AIEs smoothed to 1° (red) at 13°S, 78°W. (c) The Diurnal weighted daily REx time series of f_c in the Anth (solid) and NoAnth (dashed) simulations.

we showed results from computing albedo from area averaged cloud properties. The order of spatially regridding results and averaging influences our estimates of AIE contributions. The region of largest mean 2nd AIEs is also where the largest difference between the 2nd AIE computed from $1 \times 1^\circ$ area averages of N_d, L_p, and f_c and the 2nd AIE from the $0.125 \times 0.125^\circ$ output smoothed to $1 \times 1^\circ$ resolution (Fig. 5.18). This smoothing order difference is small (< 0.01), but not insignificant compared to the 0.05-0.1 REx-mean magnitude of the AIE components. Because N_d and L_p are nonlinearly related to albedo, some smoothing order difference is expected, but these errors can be attributed to the binary f_c. These REx mean smoothing order differences are not uniform over time, but rather arise from a few days of large difference (Fig. 5.19a,b) and correspond strongly to periods of small $1 \times 1^\circ$ average f_c (Fig. 5.19c). The particular example area shown in Fig. 5.19 holds true in general, as in the entire near-coastal region the $1 \times 1^\circ$ Anth f_c is 0.5 averaged over all REx time-space points that have a difference between averaging methods larger than 0.05, and 0.75 when the averaging order makes a smaller difference. There are small differences in L_p (35 vs. 45 gm^{-2}) and N_d (113 vs. 106 cm^{-3}) so it is mainly f_c that causes the smoothing order AIE differences. Small area mean f_c indicates a large number of cloud free points are included in the average, so there are several gridpoints with no cloud albedo. When L_p, N_d, and f_c are averaged before c is computed during times of small average f_c the N_d and L_p are smeared over on average twice the area they represent. Therefore when looking at the time variability of the 1st and 2nd AIEs any area averaging (to reduce the impact of meteorological noise on the signal) should be done after the simulation albedos are computed at each grid point.

Meteorological noise

In this section we compute an estimate of the dependence of meteorological noise on spatial and temporal scales of averaging. The $0.125 \times 0.125^\circ$ model resolution plots we have shown comparing Anth and NoAnth (for example Fig. 5.3) appear fairly noisy and incoherent outside the region of strong anthropogenic aerosol influence, even in the time-mean over the month, due to quasi-random meteorological noise between simulations. Much of the XOR

case complication is due the random variability between simulations that can shift cloudy pixels and cloud free pixels slightly so that determining the contribution of microphysics to differences in Anth and NoAnth albedo at a particular grid point/time is not possible. Averaging over space and time reduces the influence of this meteorological noise to an extent and allows weaker AIE magnitudes to be distinguished from this noise.

Quantifying the meteorological noise can be done with an ensemble approach by running the model many times exposed to small perturbations in initial meteorological conditions (Deser et al., 2012). The standard deviation of the difference of each ensemble albedo from the original simulation gives a metric for the noise level of inter-simulation albedo comparisons, and thus the variability in albedo differences due to purely non-aerosol driven meteorological noise. To save on computational expenses, we run only one additional ensemble member, with aerosol emissions as in Anth, but initialized a day later than the original Anth simulation. We also quantified the noise metric over spatial and temporal scales of averaging using an ensemble member initialized 6 hours later than the Anth simulation, and it yields very similar estimates of the meteorological noise. The analysis period is exactly the same as that for Anth. The standard deviation over time of the differences between Anth and the ensemble member ($\mathrm{Anth_{ens}}$) albedo at each point in space yields an indicator of the meteorological variability than can arise between two ensemble members.

Averaging over space and time reduces the ensemble noise and allows us to quantify the meteorological noise level we should expect between Anth and NoAnth for different averaging intervals/scales. Figure 5.20 shows the standard deviation of ensemble albedo differences as a function of space and time scale averaging resolutions. At a given noise level, the temporal scale of averaging is related to the spatial scale of averaging by a power law, estimate with a best fit line as $T \sim L^{-5/6}$. Thus there is a roughly log-linear correspondence between temporal and spatial scales of averaging. The magnitude of this noise also depends on geographic location, as AIE variability is dependent on L_{p} variability, which increases offshore. Figure 5.21 demonstrates the range of the noise level at the model resolution.

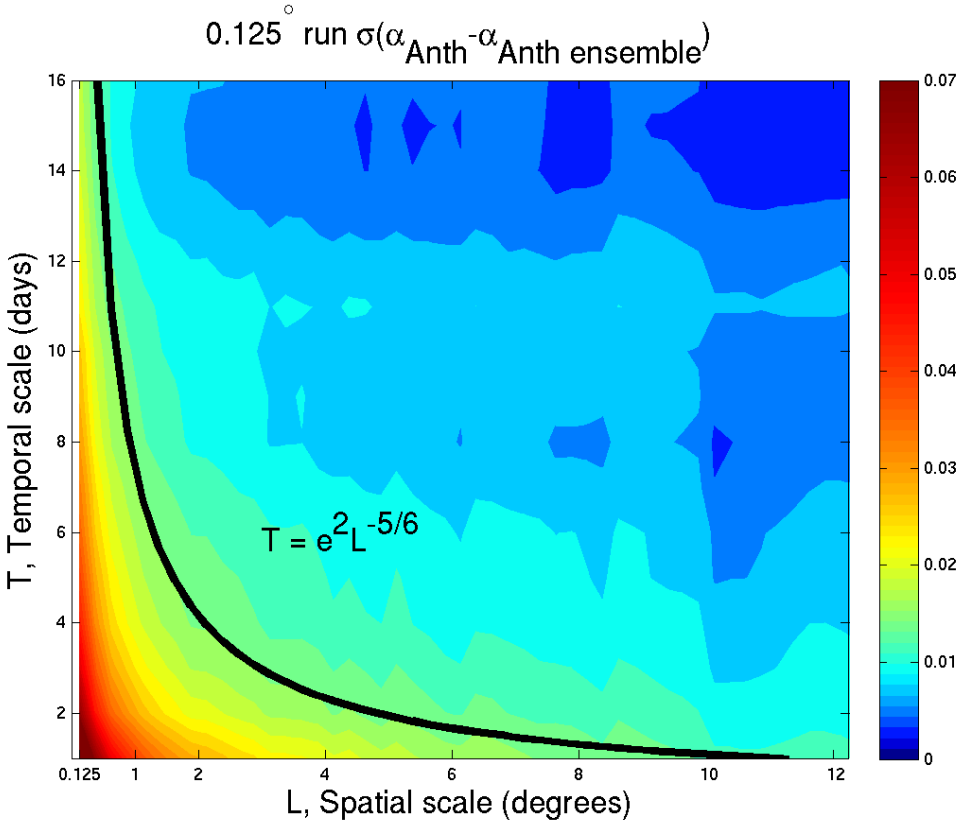

Figure 5.20: Domain (marine SEP 70-95°W, 5-35°S) average of temporal standard deviation (over the REx period 15 Oct-16 Nov) between the Anth and Anth_{ens} albedos. The latter simulation is created using the same model parameters as Anth, but is initialized a day later (7 Oct instead of 6 October).

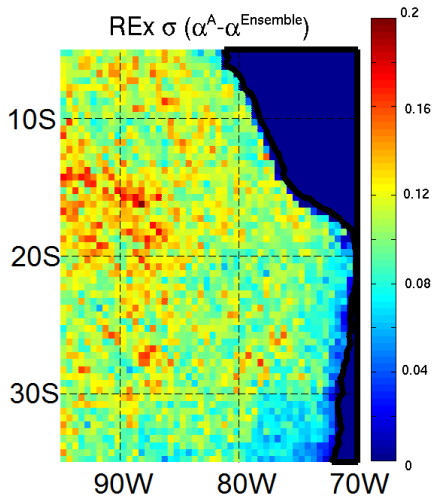

Figure 5.21: Standard deviation over REx period of the difference in albedo between the Anth simulation and an ensemble (initialized 7 Oct instead of 6 October).

AIE significance above meteorological noise

With an estimate of the noise level, we can estimate the spatial and temporal scales over which our computed AIEs are significant above this noise. If the AIE averaged over a given spatial and temporal scale is greater than twice the noise level metric, it means that the AIE is significant at roughly the 95% confidence level above the inter-simulation noise. A more accurate estimate of the confidence interval would require more ensemble members to characterize more completely the noise distribution, but we consider the two-member ensemble a reasonable first attempt. That ensembles initialized 1 day and 6 hours later than Anth result in similar noise levels supports the use of 2 member ensemble. This is powerful and allows us to rigorously establish the significance of a given change in albedo between Anth and NoAnth and determine whether it signifies a statistically-significant AIE or not. For any arbitrary averaging time and spatial scale (subdomain) we can compute appropriate confidence intervals. Figure 5.17 shows a domain that we use to compute the significance of near-shore AIE over temporal and spatial scales of averaging (Fig. 5.22). For this domain, we need to average over at least $5 \times 5^{\circ}$ areas to consider daily changes

in AIE or for periods longer than 8 days when considering the AIE at the $0.5 \times 0.5^{\circ}$ scale. At the $0.125 \times 0.125^{\circ}$ model resolution, we find that 14 days of averaging is needed for an AIE magnitude of 0.063 (20 Wm^{-2}), the near-coast (Fig. 5.17) REx time and space mean AIE, to be significant. Thus the model resolution AIE estimates shown in Fig. 5.1 a that are larger than this threshold are significant and even AIE estimates based on a single near-coastal grid point would allow a statistically robust inference of the sign of AIE. This is consistent with Fig. 5.17, which shows that even on the grid point scale, the monthly-mean AIE estimates are all positive in the near-coastal regime, and the relative scatter of AIE between nearby gridpoints is fairly small.

Figure 5.23 shows an example of how this can be used. The AIE estimate from the difference in albedo between the Anth and NoAnth smulations is averaged over 16 days at $1.625 \times 1.635^{\circ}$ resolution. The region of significant AIE above the simulation noise is identified by the dashed black line, where the AIE estimate equals twice the ensemble noise metric over this scale of averaging.

REx time variability of AIEs

With the ensemble-derived noise metric described in the previous section we can begin to examine the temporal variability of AIEs and characterize statistical significance of particular events, like hooks in the remote ocean. Based on the significance levels of near-coast AIEs, we average over areas larger than $5 \times 5^{\circ}$ to provide sufficient time resolution. Somewhat larger ($5 \times 8^{\circ}$) regions are used to aid in identifying significant AIEs that are weaker than the mean near-shore AIE. For each averaging domain we compute the noise metric described above and establish a 95% significance level.

Figure 5.24 shows the time series of three averaging regions depicted in Fig. 5.23. There is a clear change in the time variability of AIE, which is usually significant near-shore and becomes more infrequent and episodic offshore. The model 2nd AIE does not exceed the 1st AIE very often and is rarely negative (and when it is, its magnitude is small), generally enhancing the 1st AIE and increasing the net AIE variability. The model may represent physical processes that result in negative 2nd AIEs on smaller spatial scales that we remove

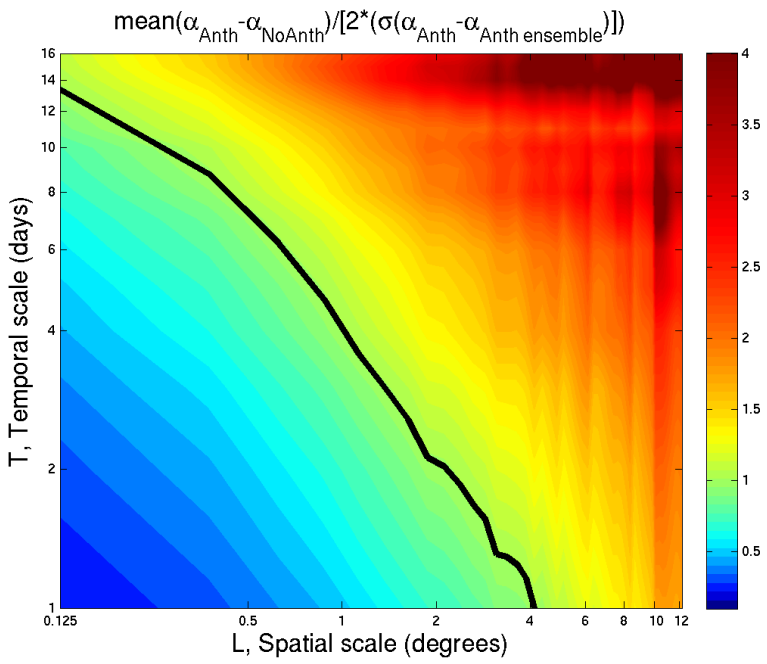

Figure 5.22: The ratio of mean AIE in the near-coast domain of Fig. 5.17 to 2 times the standard deviation between Anth and Anth_{ens} simulations as a function of spatial and temporal scales of averaging, shown in Fig. 5.20.

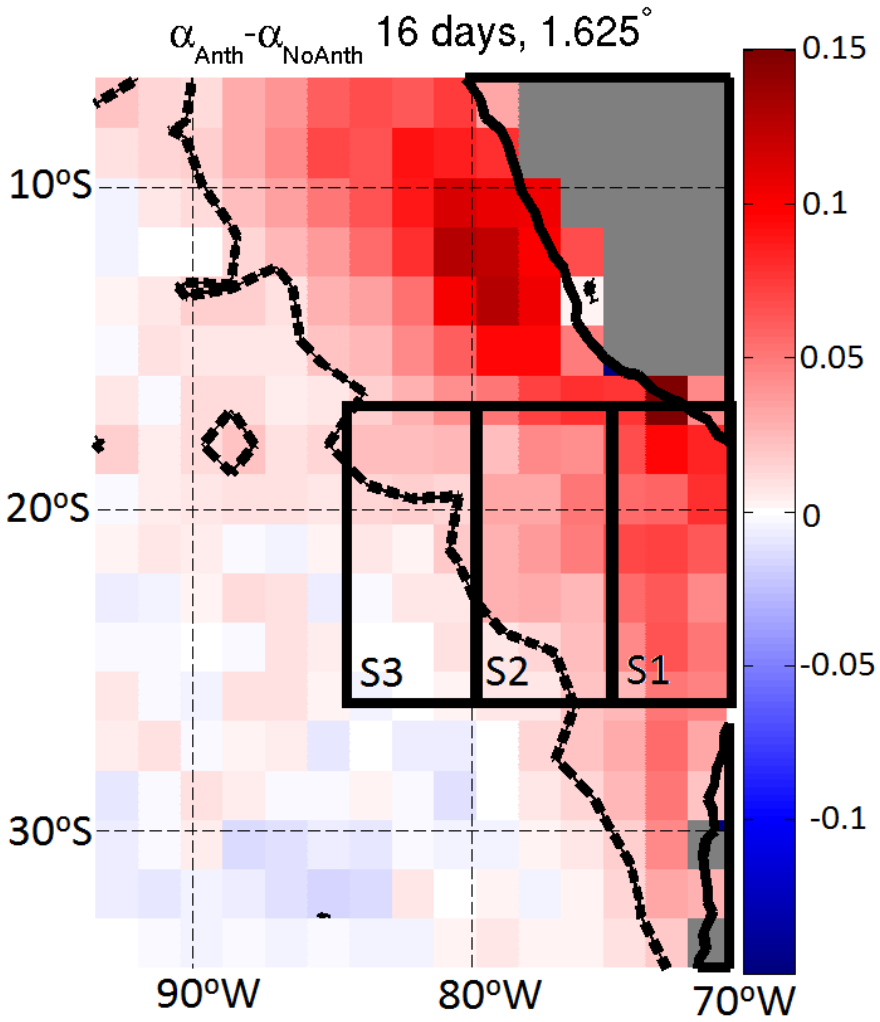

Figure 5.23: AIE estimate $\alpha^A - \alpha^N$ averaged over 16 days (31 Oct - 16 Nov) and regridded to $1.625 \times 1.625°$ resolution. The black dashed lines show where the AIE equals twice the meteorological noise at this scale of averaging, or $\alpha^A - \alpha^N = 2\sigma(\alpha^A - \alpha^{ens})$. AIE larger than the dashed line contour is significant at the 95% confidence level.The boxes labeled S1, S2, and S3 are areas averaged over in Figure 5.24

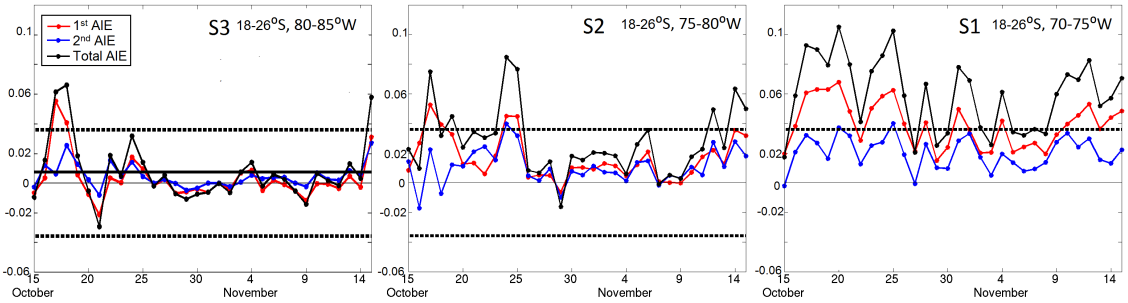

Figure 5.24: Diurnal weighted daily REx time series of 1st (red), 2nd (blue) and total (black) AIEs averaged over areas (S1) 18-26°S, 70-75°W, (S2) 18-26°S, 75-80°W and (S3) 18-26°S, 80-85°W. These regions are shown on map in Fig. 5.23. Horizontal dashed black lines indicate the 95% confidence level for AIE signal above noise associated with variability between 2 simulations. (S3) includes the mean AIE over the REx period (solid black line).

with the area average, but such values are indistinguishable from the statistical simulation noise. Averaged over timescales longer than REx, processes occurring on smaller spatial scales could become significant, but any negative components of second AIE may operate on shorter timescales as well. Thus, our model simulations are not suited to parsing individual 2nd AIEs that occur on small spatial and temporal timescales and higher resolution models such as LES are necessary to analyze processes like these. If these processes do not aggregate up to larger scales, then it is arguable that they are unlikely to generate substantial AIEs at the regional scale. The solid line in (S3) of Fig. 5.24 shows the REx mean AIE for that domain. Several cases of AIE may appear significantly larger than the mean AIE, but only with the simulation noise metric do we realize that these are indistinguishable. On October 21 it appears that both 1st and 2nd AIEs are negative, causing a strong negative total AIE signature, but is not significant above the simulation noise. A negative 1st AIE is nonsensical and this case is due to cloud fraction differences between simulations that may have nothing to do with aerosols. Without significance above simulation noise, we cannot attribute physical processes to explain this deviation of the AIE.

The similar temporal variability between the 1st and 2nd AIEs (for example R^2 = 0.53 , significant at 95% near the Peruvian coast in Fig. 5.25) enhances the total AIE variability, which appears to include quasi-periodicity on the order of 6-10 days near shore

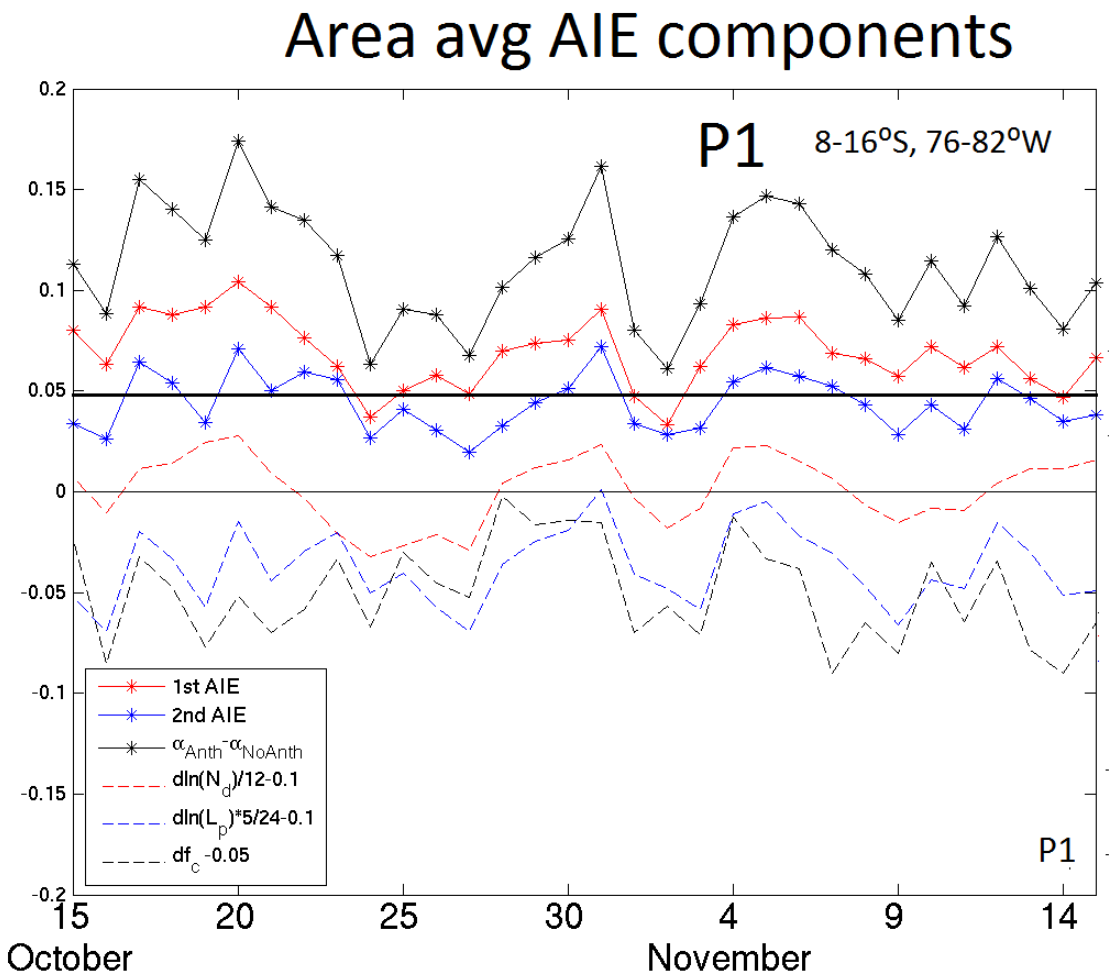

Figure 5.25: Diurnal weighted daily REx time series of 1st (red), 2nd (blue) and total (black) AIEs averaged over 0.125° resolution points (P1) 8-16°S, 76-82°W. This region is shown on map in Fig. 5.27. Nonzero horizontal black lines indicate the 95% confidence level for AIE signal above noise associated with variability between 2 simulations. This includes diurnal weighted daily area averaged differences between Anth and NoAnth $log(N_d)$ (red dashed), $log(L_p)$ (blue dashed) and f_c (black dashed) adjusted by constant factors and offsets to plot these effects on the same scale as the AIEs.

(Fig. 5.25). Using red noise 1 day lag autocorrelation, there are 29-30 degrees of freedom for AIE variables, 22 for $N_{\rm d}$, 26 for $f_{\rm c}$ and 32 for $L_{\rm p}$. In regions with the largest coverage of stratocumulus exceeding 70% $f_{\rm c}$ temporal variability is relatively small, so the time variability in area-averaged total AIE is dominated by the difference in cloud albedo between the Anth and NoAnth simulations (not shown). Fig. 5.25a includes differences between Anth and NoAnth $f_{\rm c}$, $\log(N_{\rm d})$ and $\log(L_{\rm p})$. Since α is a nonlinear function of τ, linear correlation coefficients may miss the complexities of the relationship between $N_{\rm d}$ and α, but at least give a first order approximation. The Anth-NoAnth differences in $\log(N_{\rm d})$ vary with the 1st AIE estimate ($R^2 = 0.61$, significant at 99% confidence level) and the differences in $\ln(L_{\rm p})$ correspond even more linearly with the 2nd AIE estimate ($R^2 = 0.8$), with $f_{\rm c}$ insignificantly correlated with the AIE components ($R^2 = 0.12 - 0.15$).

More than 500 km from the coast, the AIE is intermittent and largely attributable to episodic aerosol transport events (e.g. Fig. 5.24S3). Nevertheless the 2nd AIE magnitude still generally enhances the 1st AIE. Over remote ocean regions the AIE magnitudes are mostly small over large area averages, except in the case of hooks (e.g. day 17-19 Oct) explored in Chapter 4. Fig. 5.26 shows the 85-90°W averages (1500-2000 km from shore) over different latitude bands, which clearly capture Hook1 (see Chapter 4 section 4.2.2), the only event simulated during REx that reaches such distances from the coast. The enhancement of the 2nd AIE from 18-26°S to 10-18°S and the one day lag between peak 1st AIE and peak 2nd AIE in the northern domain demonstrate a delayed 2nd AIE (Fig. 5.26Q1,Q2). Figure 5.27 visualizes AIE magnitudes on 18 October at $1 \times 1^\circ$ resolution, during Hook1, showing the spatial distribution of the 2nd AIE enhancement of the 1st AIE as well as showing the large pixel-to-pixel variability at the 0.125° resolution, especially in the 2nd AIE magnitude.

Also of particular note on 18 October is a broad region of negative AIE magnitude in the unpolluted remote ocean in the southern portion of the displayed domain (28-35°S, 72-92°W, Fig. 5.27) that IS significant above the simulation noise. Figure 5.26Q3 indicates that the negative AIE magnitude here is of a similar magnitude to the positive AIE further north and is significant above the noise level for the given scales of averaging. This negative AIE is a result of broad $f_{\rm c}$ displacement between Anth and NoAnth simulations. Whereas day to day

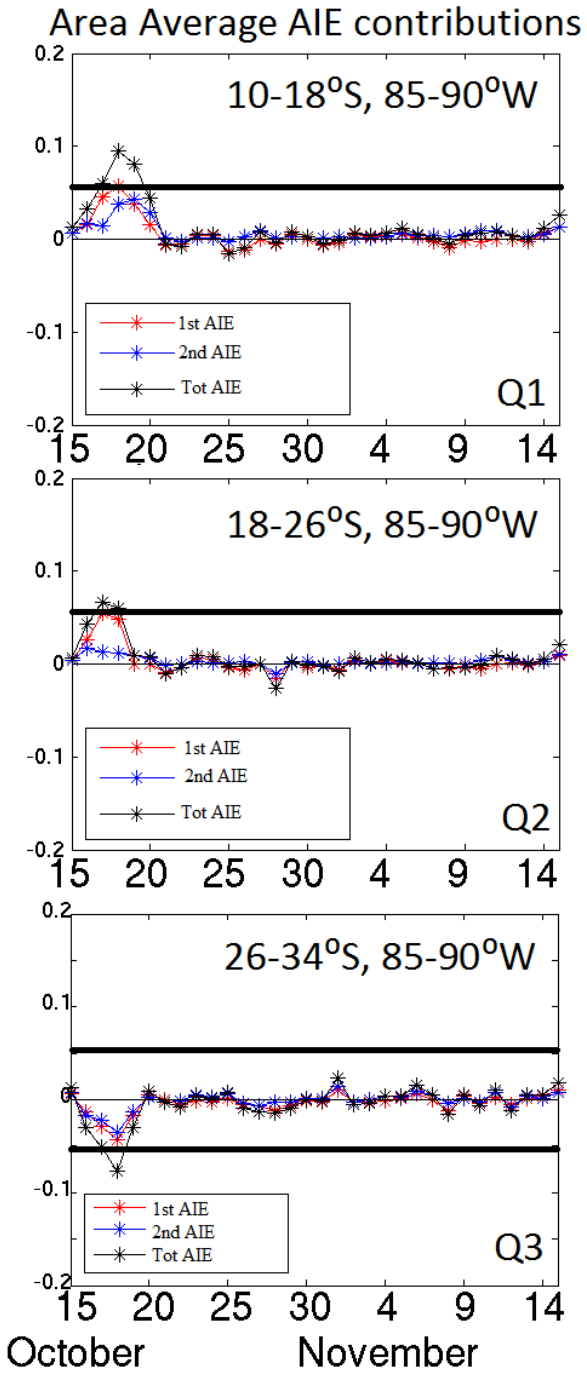

Figure 5.26: Diurnal weighted daily REx time series of 1st (red), 2nd (blue) and total (black) AIEs averaged over 0.125° resolution points (Q1) 10-18°S, 85-90°W, (Q2) 18-26°S, 85-90°W, and (Q3) 24-34°S, 85-90°W. Nonzero horizontal black lines indicate the 95% confidence level for AIE signal above noise associated with variability between 2 ensemble simulations.

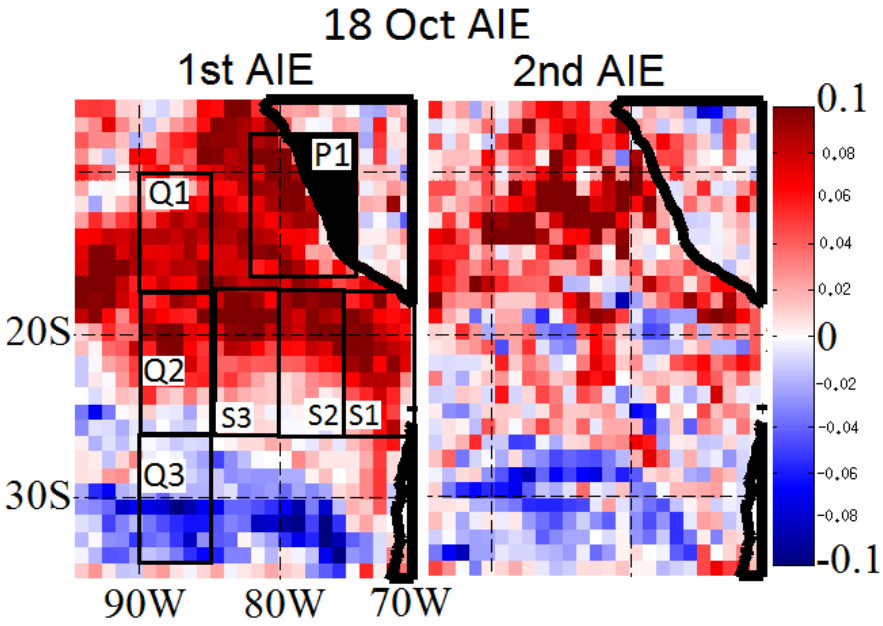

Figure 5.27: Diurnal weighted 1st and 2nd AIE components on 19 October, 2008. Right column shows this data smoothed to 1° resolution.

variations between ensemble members do occasionally demonstrate coherent area regions of albedo difference caused by f_c differences, they are generally much smaller than the region here. It is difficult to establish whether this difference, once again large a consequence of the dichotomy between cloudy and cloud-free regions in the different simulations, is due to simulation noise, or is a physical consequence of aerosols modifying the regional dynamics in unexpected ways. The fact that it coincides with an episode of exceptionally strong AIEs offshore (a hook) further to the north, leads us to suspect there may be a physical basis.

During Hook1 on 18 Oct a broad region of 80-250 m higher inversion height in Anth than NoAnth coincides with the hook. South of 30°S the inversion height formulation identifies a stripe of large inversion heights (more than 3 km) ahead/northeast of a region of low (800 m) heights on 18 October. The NoAnth feature is shifted several degrees to the southwest of the Anth feature , causing large inversion height differences in this region and shifted cloud features (Fig. 5.28). A propagating wave induced by changes in inversion height is one possibility. However, there is no obvious difference between the magnitude and distribution

of Anth and NoAnth simulation vertical velocity $\sim$ 100 mb above the inversion (Fig. 5.29). The difference between Anth and NoAnth free tropospheric vertical velocity (Fig. 5.30) indicates a wave-like offset, but this could be due to the meteorological differences between Anth and NoAnth simulations rather than a wave set off by changes in inversion height. It is thus unclear whether this case represents a failure of the noise metric or a real physical phenomena.

Although we note significance above the simulation meteorological noise, it is possible this characterization fails south of 30°S, where variability in meteorology is much less quiescent than in the stratocumulus region and broad regions of difference cloud fraction coverage can occur between ensemble members (not shown) on individual days. This does not appear to increase the ensemble noise (Fig. 5.21) over the REx period but can impact ensemble differences on individual days. The noise between simulations may not be a normal distribution best characterized by the standard deviation, which would be a good next step to investigate along with other possible physical mechanisms for the presence of the hook inducing a change in cloud coverage south of the hook.

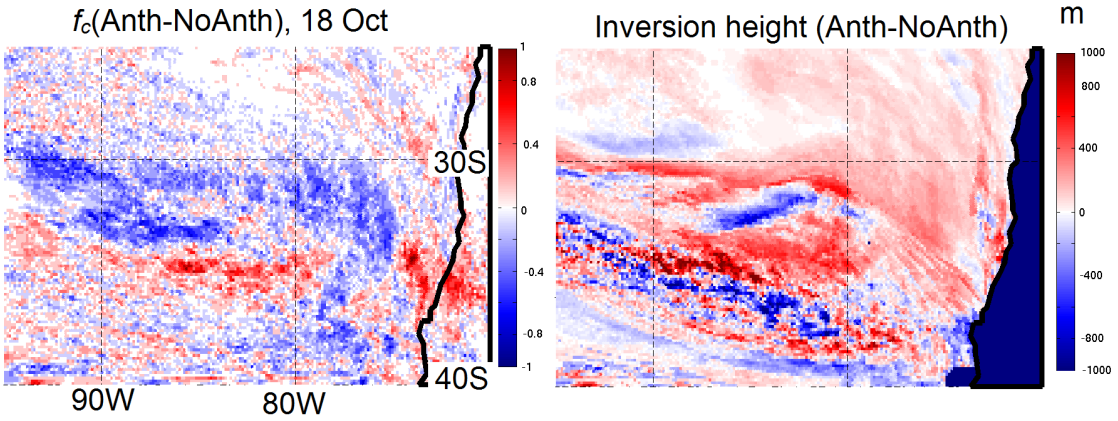

Figure 5.28: Average over 18 October difference between Anth and NoAnth f_c and inversion height.

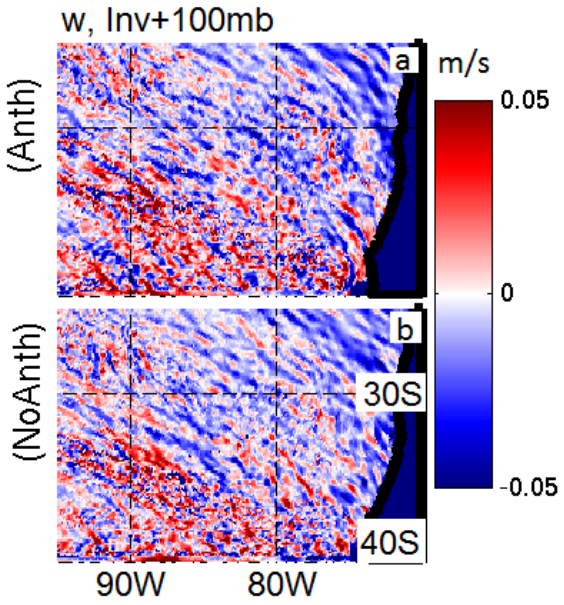

Figure 5.29: Average over 18 October (a) Anth and (b) NoAnth vertical velocity 4 model levels above the inversion ($\sim$ 100 mb).

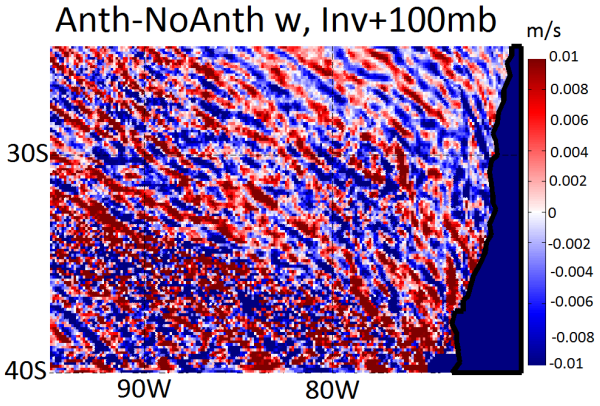

Figure 5.30: Average over 18 October difference between Anth and NoAnth vertical velocity 4 model levels above the inversion ($\sim$ 100 mb).

5.3 AIE Conclusions

This chapter demonstrates complications that arise when distinguishing between microphysical and macrophysical impacts total aerosol indirect effects during REx using a regional model. WRF-Chem is fairly suitable to studying AIEs as it permits both microphysical impact on radiation and feedback physics that lead to 2nd AIEs such as the lifetime effect. There is uncertainty in how much unrepresented processes such as sedimentation and dispersion would influence our characterization of AIEs, especially since the strength of these processes in altering albedo has not been clearly established in the literature. We make the necessary assumption that these would have little impact. We compare a simulation with anthropogenic emissions to one without to compute an estimate of AIE due to anthropogenic aerosols, which is simply the difference in albedo between the two simulations (assuming direct and semi-direct effects are small, which we find they are). We define an albedo proxy that is a function of key cloud variables (f_c, N_d, L_p) as in Chapter 2, though enhance it to handle cases of optically thin clouds. We use this approach to separate the contributions from microphysics and the 1st AIE from macrophysics and the 2nd AIE. An estimate of the Twomey effect is made by computing an albedo using microphysics (N_d) from one simulation and the macrophysics (f_c, L_p) from the other. However, due to meteorological variability between the two simulations, there may be a cloud in only one of the simulations at a particular gridpoint. This makes the Twomey effect estimate strongly dependent on the choice of simulation for constant macrophysics. When this is accounted for, by area averaging or ignoring the cases of differing cloudiness between simulations, there is still a small, fairly symmetric difference between Twomey effect estimates using different constant macrophysics. This is representative of inherent uncertainty in the magnitude of the Twomey effect and we choose an average of the estimates as a reasonable metric. We find that the Twomey effect contributes about 50-80% of the total AIE and its contribution is spatially and temporally variable. Secondary AIEs make up the rest and are modeled to enhance rather than offset the 1st AIE. While processes that would offset the 1st AIE are permitted in the model, the positive feedback effects dominate. These effects are shown mostly through L_p changes in as there is little difference in f_c between simulations.

The noise between simulations is largely related to that the gridpoints that are cloudy and cloud-free can shift unrelated to aerosols. Meteorological variability between simulations can swamp the magnitude of the AIE. Although this is a model specific issue, it is reflective of the more general problem of distinguishing aerosol related processes from meteorological ones. An ensemble simulation is run to compute an estimate of the model simulation noise as a function of spatial and temporal scales of averaging. This give an estimate of how much averaging is necessary to detect a significant AIE and puts errorbars on the magnitudes we present. Averaged over sufficiently large areas we present the time variability of AIE in various regions in the SEP. The time variability in AIE is dominated by variability in the albedo of the simulation with anthropogenic aerosols. There is a clear subseasonal variability in the strength of the AIEs. In the remote ocean the AIE estimate is typically insignificant except during times of a hook, when AIE strengths are similar to those seen regularly near the coast. On the particular day of the Hook1 the strong AIE magnitude in the hook region is paired with a large region of significantly negative AIE. This is possible due to a propagating wave initiated by changed in entrainment and inversion height in the hook region, though further investigation is needed. The magnitude of the AIEs reported here is not meant to be representative of the climate relevant AIE, which would need to sample much longer time periods and more of the meteorological variability of the region in all seasons. Rather the benefit of this work arises from the analysis approach. Quantifying aerosol processes in the presence of convolving variability is an essential reason why the net AIE contribution to climate change is so uncertain. We share a method for finding appropriate scales of averaging needed to detect an AIE signal. While using this will be model and platform specific, it is important to recognize AIE estimates should be paired with significance values.

Chapter 6

CONCLUSIONS

6.1 Summary

The purpose of this work has been to deepen our understanding of how aerosol-cloud interactions (ACI) affect net regional radiative properties in the stratocumulus dominated region of the southeast Pacific. We investigate aerosol indirect effects (AIE), the influence of aerosols on radiation through their impact on cloud properties, by examining meteorological and microphysical controls on albedo variability and aerosol transport mechanisms. We have been the fortunate position of having three major modes of information to work with: satellite data, in situ data from the VOCALS field campaign and a regional model with interactive chemistry and aerosol processes (WRF-Chem). The information from any one of these platforms is useful for recognizing specific parts of the ACIs as demonstrated by the vast number of papers that define and derive AIEs using one data source. But, integration of all three is powerful and allows us to gain confidence in our model, adding credibility to the results and ensuing interpretations. Additionally, this work crosses boundaries by addressing a wide range of physical, chemical, and meteorological processes across multiple scales in time and space. Nonetheless, it is also recognized in this work that the convolved nature of aerosol and meteorological processes remains a challenging problem requiring careful analysis and caveats.

In this work we divide AIEs into two distinct process categories as microphysical and macrophysical mechanisms (1st and 2nd AIEs) and develop a method to consider their respective impacts on shortwave radiation as separately as possible. We use this approach to understand albedo and stratocumulus cloud variability in the SEP both in MODIS data and the model. At the heart of the microphysical processes relating aerosols to microphysics is the the activation of aerosols to cloud droplets, but also important are hygroscopic aerosol growth and aqueous chemistry that can affect the number and size of aerosols and thus

cloud droplets. Macrophysical responses to these microphysical changes affect cloud cover and liquid water path mainly through precipitation changes. Meteorological variability helps to control the temporal variability of both aerosols (and thus cloud microphysical properties) and cloud macrophysical properties, and thus isolating the aerosol related effects from meteorology is a challenge. Correlations of cloud microphysical and macrophysical parameters with meteorological parameters are significant, consistent with simple physical explanations, but also quite weak (George and Wood, 2010). This leaves a large amount of cloud variability unexplained by simple large-scale meteorological variables. Part of the reason for the lack of a single predictive meteorological control parameter for clouds on short timescales is that other processes, some of which are likely internal MBL processes, operate on timescales short enough that they average out in the time periods we consider. There are many meteorological factors that act over large regional areas but can also affect cloud on small time/space scales, including gravity waves, cold advection, and stability.

We show in Chapter 2 that microphysical variability contributes only weakly to observed variability. This might be used to argue that AIEs are inconsequential to albedo variability and that their main influence is upon the mean longitudinal N_{d} gradient. However, the strong contributions from covariability between variables and the large changes in N_{d} associated with the subtropical high variability suggest that microphysical processes are highly convolved with meteorological ones and that aerosol impact is not so simple as Twomey's argument. Given that meteorological variability swamps the signal associated with microphysics on short timescales in our observational study we use modeling to isolate AIEs better by comparing simulations with anthropogenic aerosols to a simulation without them.

We identify a pathway for aerosol transport to the remote ocean that results in 'hooks' of large droplet concentration against an unpolluted background. By studying hooks, particular episodes of strong offshore aerosol transport, we show that on individual days the impact of anthropogenic aerosol on the SEP cloud properties can be strong. We use a Lagrangian framework following a particular event of offshore aerosol transport to capture the temporal component of the macrophysical response to microphysical changes more clearly than in the Eulerian framework. This allows us to demonstrate the timeframe over

which secondary impacts occur associated with an increase in aerosol loading in the remote ocean. The macrophysics and albedo following hook do appear affected significantly by the aerosol-cloud interactions in specific events and thus the transport of anthropogenic aerosols is shown to contribute to the remote ocean albedo variability. Additionally chapter 5 demonstrates that the AIEs associated with hooks events are significant to the time variability of AIEs.

However, even in the context of a specific aerosol transport event, the chaotic nature of meteorological variability between two ensemble simulations limits the temporal and spatial scales over which AIEs can be reliably quantified. The binary representation of f_c causes similar challenges as missing data in observational studies. In this case, not only does it affect the analytic techniques, but also strongly affects our Anth vs NoAnth model simulation comparisons. By design, with the method developed in chapter 5, we can still use the model isolate aerosol effects, as long as we use spatial and temporal averaging scales that reduce the model-model meteorological noise compared to the AIE signal.

6.2 Future work

Since stratocumulus clouds over the SEP and in other regions globally contribute strongly to the uncertainty in AIE magnitude this work has implications for the total AIE uncertainty, though experiments would need to verify the behavior of the SEP is repeated over other subtropical eastern ocean basins dominated by stratocumulus cloud. The aerosol transport mechanisms in other regions may not have the same behavior we note in the SEP and may have different dominant temporal and spatial scales dependent on the variability of local meteorology. The Andes mountains have a strong influence on the SEP aerosol transport, and it would be interesting to investigate how aerosol transport and aerosol cloud interactions differ in regions of lower elevation coastal topography. A similar scenario of three pillars of data: satellite, model and field observations may come to fruition in the next few years through an experiment on the west coast of Africa, home to another region of stratocumulus. There is thus opportunity to test the extent to which findings here apply to other stratocumulus regions and the utility of the methods developed here.

Other future work on the SEP or other stratocumulus regions could involve more and

improved versions of the analysis done here. An effort should be made to use in-situ and satellite observations to constrain the model rather than just validate the properties of a particular set-up, particularly using N_{d} (e.g. Saide et al., 2012b). This way, when experimenting with different parameterizations in the model, a constraint within the model would maintain reasonable microphysics and a wider variety of parameterizations could be tested. In the way we have used the model here, a parameterization change usually causes some important variable to become unrealistic and better constraining the model microphysical processes might help. Additionally, a newer version of the model that includes more advanced microphysics may better predict precipitation and L_{p}. Particularly the Morrison scheme predicts two moments in rain, which Yang et al. (2012) found to be relevant in the SEP.

Increasing model resolution might improve the realism of processes permitted and thus the match of model to observations, though with an end-goal of improving the representation of aerosol processes in GCMs this may not be particularly useful. Rather, a marked increase in resolution over the Andes in a separate run could be used to create boundary conditions for a simulation over the SEP marine domain. Or, the implementation of variable resolution domains, an active area of development, could be useful to improving offshore aerosol transport. This would improve the quality of chemical/aerosol transport and would likely improve the timing/extent issues in hook representation. Additionally, increasing vertical resolution would allow for multi-level representation of cloud processes. Though, the choice of physics parameterizations would need to be reevaluated because initial experiments increasing vertical resolution in our model resulted in marked reduction in simulation quality.

Incorporation of the UW cumulus scheme that pairs with the UWPBL scheme already implemented in WRF-Chem, may lead to model improvements as well, especially in the remote ocean regions where cumulus plays more of a role. There is active work being done to also allow for aerosol feedbacks upon the cumulus schemes in WRF-Chem and this feature would motivate use of the UW cumulus scheme further. In general modeling ACIs with cumulus has additional complications, such as transient aerool perturbations, that need more focus (Xue et al., 2008; Lee and Feingold, 2012).

Additionally, running the model for a longer time period would be useful for testing further the hypothesis described in Wood and George (2010) regarding the role of the subtropical high pressure variability on meteorological and cloud cloud fields and their covariability compared to its impact on aerosol transport. This would also reduce the Anth-NoAnth meteorological noise in simulation average features. Several barriers would need to be overcome before such work would be done. The model would need to be stripped down to its essential features by saving less variables less often. Anthropogenic emissions would need to be extended beyond the VOCALS period either by assuming invariant emissions or compiling a longer data source. The strength of AIE during other seasons could be evaluated. During other synoptic scenarios the strength of the AIE likely oscillates due to transport changes, and one could search for the minimum time period necessary for the mean AIE to stabilize. Additionally a full ensemble study with more than two enemble members would improve characterization of the noise level.

Work on quantifying AIEs within the context of known meteorological variability is fascinating and will likely evolve in the coming years. It encompasses fundamental atmospheric science issues of interactions between multiple scales of physical processes. Here we have made a contribution towards understanding these AIEs from a variety of perspectives and proposed a methodology to address them.

References

Abdul-Razzak, H. and Ghan, S.J.: A parameterization of aerosol activation 2. Multiple aerosol types, J. Geophys. Res.-Atmos., 105, 6837–6844, 2000.

Ackerman, A.S., Kirkpatrick, M.P., Stevens, D.E., and Toon, O.B.: The impact of humidity above stratiform clouds on indirect aerosol climate forcing, Nature, 432, 1014–1017, doi:10.1038/nature03174, 2004.

Ackermann, I.J., Hass, H., Memmesheimer, M., Ebel, A., Binkowski, F.S., and Shankar, U.: Modal aerosol dynamics model for Europe: Development and first applications, Atmos. Environ., 32, 2981–2999, doi:10.1016/S1352-2310(98)00006-5, 1998.

Albrecht, B.A.: Aerosols, cloud microphysics, and fractional cloudiness, Science, 245, 1227–1230, 1989.

Albrecht, B.A., Fairall, C.W., Thomson, D.W., White, A.B., Snider, J.B., and Schubert, W.H.: Surfacebased remote sensing of the observed and the Adiabatic liquid water content of stratocumulus clouds, Geophys. Res. Lett., 17, 89–92, doi:10.1029/GL017i001p00089, 1990.

Allen, G., Coe, H., Clarke, A., Bretherton, C., Wood, R., Abel, S.J., Barrett, P., Brown, P., George, R., Freitag, S., McNaughton, C., Howell, S., Shank, L., Kapustin, V., Brekhovskikh, V., Kleinman, L., Lee, Y.N., Springston, S., Toniazzo, T., Krejci, R., Fochesatto, J., Shaw, G., Krecl, P., Brooks, B., McMeeking, G., Bower, K.N., Williams, P.I., Crosier, J., Crawford, I., Connolly, P., Allan, J.D., Covert, D., Bandy, A.R., Russell, L.M., Trembath, J., Bart, M., McQuaid, J.B., Wang, J., and Chand, D.: South East Pacific atmospheric composition and variability sampled along 20 degrees S during VOCALS-REx, Atmos. Chem. Phys., 11, 2011.

Bandy, A.R., Thornton, D.C., Tu, F.H., Blomquist, B.W., Nadler, W., Mitchell, G.M., and Lenschow, D.H.: Determination of the vertical flux of dimethyl sulfide by eddy correlation and atmospheric pressure ionization mass spectrometry (APIMS), J. Geophys. Res.-Atmos., 107, 4743, doi:10.1029/2002JD00247, 2002.

Bates, T.S., Lamb, B.K., Guenther, A., Dignon, J., and Stoiber, R.E.: Sulfur emissions to the atmopshere from natural sources, Journal of Atmospheric Chemistry, 14, 315–337, 1992.

Benkovitz, C.M., Scholtz, M.T., Pacyna, J., Tarrason, L., Dignon, J., Voldner, E.C., Spiro, P.A., Logan, J.A., and Graedel, T.E.: Global gridded inventories of anthropogenic emissions of sulfur and nitrogen, J. Geophys. Res. -Atmos., 101, 29 239–29 253, 1996.

Bennartz, R.: Global assessment of marine boundary layer cloud droplet number concentration from satellite, J. Geophys. Res.-Atmos., 112, D02 201, doi:10.1029/2006JD007547, 2007.

Boers, R.: Influence of seasonal variation in cloud condensation nuclei, drizzle, and solar radiation,

on marine stratocumulus optical depth, Tellus Series B-Chemical and Physical Meteorology, 47, 578–586, 1995.

Bohren, C.F. and Clothiaux, E.: Fundamentals of Atmospheric Radiation, Wiley-VCH, Hoboken, NJ, 2006.

Bony, S., Letreut, H., Duvel, J.P., and Kandel, R.S.: Satellite validation of GCM-simulated annual cycle of the earth radiation budget and cloud forcing, J. Geophys. Res. -Atmos., 97, 18 061–18 081, 1992.

Boucher, O. and Lohmann, U.: The sulfate-CCN-cloud albedo effect: A sensitivity study with two general circulation models, Tellus Series B-Chemical and Physical Meteorology, 47, 281–300, 1995.

Brenguier, J.L., Pawlowska, H., and Schuller, L.: Cloud microphysical and radiative properties for parameterization and satellite monitoring of the indirect effect of aerosol on climate, J. Geophys. Res. -Atmos., 108, 14, 2003.

Bretherton, C.S. and Park, S.: A New Moist Turbulence Parameterization in the Community Atmosphere Model, J. Clim., 22, 3422–3448, 2009.

Bretherton, C.S., Widmann, M., Dymnikov, V.P., Wallace, J.M., and Blade, I.: The effective number of spatial degrees of freedom of a time-varying field, J. Clim., 12, 1990–2009, 1999.

Bretherton, C.S., Uttal, T., Fairall, C.W., Yuter, S.E., Weller, R.A., Baumgardner, D., Comstock, K., Wood, R., and Raga, G.B.: The EPIC 2001 stratocumulus study, Bulletin of the American Meteorological Society, 85, 967–+, 2004.

Bretherton, C.S., Blossey, P.N., and Uchida, J.: Cloud droplet sedimentation, entrainment efficiency, and subtropical stratocumulus albedo, Geophys. Res. Lett., 34, L03 813, doi:DOI: 10.1029/2006GL027648, 2007.

Bretherton, C.S., Wood, R., George, R.C., Leon, D., Allen, G., and Zheng, X.: Southeast Pacific stratocumulus clouds, precipitation and boundary layer structure sampled along 20 degrees S during VOCALS-REx, Atmos. Chem. Phys., 10, 8, 2010.

Cahalan, R.F., Ridgway, W., Wiscombe, W.J., Bell, T.L., , and Snider, J.: The albedo of fractal stratocumulus clouds, J.Atmos. Sci., 51, 2434–2455, 1994.

Caldwell, P., Bretherton, C.S., and Wood, R.: Mixed-layer budget analysis of the diurnal cycle of entrainment in Southeast Pacific stratocumulus, J.Atmos. Sci., 62, 3775–3791, 2005.

Carn, S.A., Krueger, A.J., Krotkov, N.A., Yang, K., and Levelt, P.F.: Sulfur dioxide emissions from Peruvian copper smelters detected by the Ozone Monitoring Instrument, Geophys. Res. Lett., 34, L09 801, doi:DOI: 10.1029/2006GL029020, 2007.

Cess, R.D.: Climate change – appraisal of atmospheric feedback mechanisms employing zonal cli-

matology, J.Atmos. Sci., 33, 1831–1843, 1976.

Chang, J.S., Binkowski, F., Seaman, N., McHenry, J., Samson, P., Stockwell, W., Walcek, C., Madronich, S., Middleton, P., Pleim, J., and Lansford, H.: The regional acid deposition model and engineering model, in: Acidic Deposition: State of Science and Technology, pp. 29–78, National Acid Precipitation Assessment Program, Washington D.C., 1990.

Chapman, E.G., Gustafson, W.I., Jr., Easter, R.C., Barnard, J.C., Ghan, S.J., Pekour, M.S., and Fast, J.D.: Coupling aerosol-cloud-radiative processes in the WRF-Chem model: Investigating the radiative impact of elevated point sources, Atmos. Chem. Phys., 9, 2009.

Chou, M.D., Suarez, M.J., Ho, C.H., Yan, M. M.H., and Lee, K.T.: Parameterizations for cloud overlapping and shortwave single-scattering properties for use in general circulation and cloud ensemble models, J. Clim., 11, 202–214, doi:10.1175/1520-0442(1998)011¡0202:PFCOAS¿2.0.CO;2, 1998.

Deser, C., Phillips, A., Bourdette, V., and Teng, H.Y.: Uncertainty in climate change projections: the role of internal variability, Climate Dynamics, 38, 527–546, 2012.

Emmons, L.K., Walters, S., Hess, P.G., Lamarque, J.F., Pfister, G.G., Fillmore, D., Granier, C., Guenther, A., Kinnison, D., Laepple, T., Orlando, J., Tie, X., Tyndall, G., Wiedinmyer, C., Baughcum, S.L., and Kloster, S.: Description and evaluation of the Model for Ozone and Related chemical Tracers, version 4 (MOZART-4), Geoscientific Model Development, 3, 2010.

Fahey, K.M. and Pandis, S.N.: Optimizing model performance: variable size resolution in cloud chemistry modeling, Atmos. Environ., 35, 4471–4478, doi:10.1016/S1352-2310(01)00224-2, 2001.

Fast, J., Aiken, A.C., Allan, J., Alexander, L., Campos, T., Canagaratna, M.R., Chapman, E., DeCarlo, P.F., deFoy, B., Gaffney, J., deGouw, J., Doran, J.C., Emmons, L., Hodzic, A., Herndon, S.C., Huey, G., Jayne, J.T., Jimenez, J.L., Kleinman, L., Kuster, W., Marley, N., Russell, L., Ochoa, C., Onasch, T.B., Pekour, M., Song, C., Ulbrich, I.M., Warneke, C., Welsh-Bon, D., Wiedinmyer, C., Worsnop, D.R., Yu, X.Y., and Zaveri, R.: Evaluating simulated primary anthropogenic and biomass burning organic aerosols during MILAGRO: implications for assessing treatments of secondary organic aerosols, Atmos. Chem. Phys., 9, 2009.

Fast, J.D., Gustafson, W.I., Jr., Easter, R.C., Zaveri, R.A., Barnard, J.C., Chapman, E.G., Grell, G.A., and Peckham, S.E.: Evolution of ozone, particulates, and aerosol direct radiative forcing in the vicinity of Houston using a fully coupled meteorology-chemistry-aerosol model, J. Geophys. Res.-Atmos., 111, D21 305, doi:10.1029/2005JD006721, 2006.

Fu, Q. and Liou, K.N.: On the correlated k-distribution method for radiative transfer in nonhomogenous atmospheres, J.Atmos. Sci., 49, 2139–2156, 1992.

Fu, Q. and Liou, K.N.: Parameterization of the radiative properties pf cirrus clouds, J.Atmos. Sci., 50, 2008–2025, 1993.

Garreaud, R.D. and Munoz, R.C.: The low-level jet off the west coast of subtropical South America: Structure and variability, Monthly Weather Review, 133, 2246–2261, 2005.

Garreaud, R.D. and Rutllant, J.: Coastal lows along the subtropical west coast of South America: Numerical simulation of a typical case, Monthly Weather Review, 131, 891–908, 2003.

Garreaud, R.D., Rutllant, J., Quintana, J., Carrasco, J., and Minnis, P.: CIMAR-5: A snapshot of the lower troposphere over the subtropical southeast Pacific, Bulletin of the American Meteorological Society, 82, 2193–2207, 2001.

Garreaud, R.D., Rutllant, J.A., and Fuenzalida, H.: Coastal lows along the subtropical west coast of South America: Mean structure and evolution, Monthly Weather Review, 130, 75–88, 2002.

George, R.C. and Wood, R.: Subseasonal variability of low cloud radiative properties over the southeast Pacific Ocean, Atmos. Chem. Phys., 10, 2010.

Gettelman, A., Liu, X., Ghan, S.J., Morrison, H., Park, S., Conley, A.J., Klein, S.A., Boyle, J., Mitchell, D.L., and Li, J. L.F.: Global simulations of ice nucleation and ice supersaturation with an improved cloud scheme in the Community Atmosphere Model, J. Geophys. Res.-Atmos., 115, D18 216, doi:10.1029/2009JD013797, 2010.

Gong, S.L., Barrie, L.A., and Blanchet, J.P.: Modeling sea-salt aerosols in the atmosphere .1. Model development, J. Geophys. Res.-Atmos., 102, 3805–3818, doi:10.1029/96jd02953, 1997.

Grell, G.A., Peckham, S.E., Schmitz, R., McKeen, S.A., Frost, G., Skamarock, W.C., and Eder, B.: Fully coupled "online" chemistry within the WRF model, Atmos. Environ., 39, 6957–6975, doi:10.1016/j.atmosenv.2005.04.027, 2005.

Gustafson, W.I., Jr., Chapman, E.G., Ghan, S.J., Easter, R.C., and Fast, J.D.: Impact on modeled cloud characteristics due to simplified treatment of uniform cloud condensation nuclei during NEAQS 2004, Geophys. Res. Lett., 34, L19 809, doi:10.1029/2007GL030021, 2007.

Han, Q.Y., Rossow, W.B., and Lacis, A.A.: Near-global survey of effective droplet radii in liquid water clouds using ISCCP data, J. Clim., 7, 465–497, 1994.

Hartmann, D.L. and Short, D.A.: On the use of Earth radiation budget statistics for studies of clouds and climate, J.Atmos. Sci., 37, 1233–1250, 1980.

Huneeus, N., Gallardo, L., and Rutllant, J.A.: Offshore transport episodes of anthropogenic sulfur in northern Chile: Potential impact on the stratocumulus cloud deck, Geophys. Res. Lett., 33, L19 819, doi:10.1029/2006GL026921, 2006.

Isaksen, I. S.A., Granier, C., Myhre, G., Berntsen, T.K., Dalsoren, S.B., Gauss, M., Klimont, Z.,

Benestad, R., Bousquet, P., Collins, W., Cox, T., Eyring, V., Fowler, D., Fuzzi, S., Jockel, P., Laj, P., Lohmann, U., Maione, M., Monks, P., Prevot, A. S.H., Raes, F., Richter, A., Rognerud, B., Schulz, M., Shindell, D., Stevenson, D.S., Storelvmo, T., Wang, W.C., van Weele, M., Wild, M., and Wuebbles, D.: Atmospheric composition change: Climate-Chemistry interactions, Atmospheric Environment, 43, 5138–5192, 2009.

Kalnay, E., Kanamitsu, M., Kistler, R., Collins, W., Deaven, D., Gandin, L., Iredell, M., Saha, S., White, G., Woollen, J., Zhu, Y., Chelliah, M., Ebisuzaki, W., Higgins, W., Janowiak, J., Mo, K.C., Ropelewski, C., Wang, J., Leetmaa, A., Reynolds, R., Jenne, R., and Joseph, D.: The NCEP/NCAR 40-year reanalysis project, Bulletin of the American Meteorological Society, 77, 437–471, 1996.

Kaufman, Y.J., Koren, I., Remer, L.A., Rosenfeld, D., and Rudich, Y.: The effect of smoke, dust, and pollution aerosol on shallow cloud development over the Atlantic Ocean, Proceedings of the National Academy of Sciences of the United States of America, 102, 11 207–11 212, 2005.

Kazil, J., Wang, H., Feingold, G., Clarke, A.D., Snider, J.R., and Bandy, A.R.: Modeling chemical and aerosol processes in the transition from closed to open cells during VOCALS-REx, Atmos. Chem. Phys.s, 11, 7491–7514, 2011.

Kiehl, J.T.: Twentieth century climate model response and climate sensitivity, Geophys. Res. Lett., 34, 2007.

Kindel, B.C., Pilewskie, P., Schmidt, K.S., Coddington, O., and King, M.D.: Solar spectral absorption by marine stratus clouds: Measurements and modeling, J. Geophys. Res. -Atmos., 116, 2011.

King, M.D. and Harshvardhan: Comparative accuracy of selected multiple-scattering approximations, J.Atmos. Sci., 43, 1986.

King, M.D., Tsay, S.-C., Platnick, S.E., Wang, M., and Liou, K.-N.: Cloud retrieval algorithms for MODIS: Optical thickness, effective particle radius, and thermodynamic phase, in: NASA, MODIS Algorithm Theoretical Basis Doc, 1997.

Klein, S.A.: Synoptic variability of low-cloud properties and meteorological parameters in the subtropical trade wind boundary layer, J. Clim., 10, 2018–2039, 1997.

Klein, S.A. and Hartmann, D.L.: The seasonal cycle of low stratiform clouds, J. Clim., 6, 1587–1606, doi:10.1175/1520-0442(1993)006¡1587:TSCOLS¿2.0.CO;2, 1993.

Klein, S.A., Hartmann, D.L., and Norris, J.R.: On the relationships among low-cloud structure, sea-surface temperature, and atmospheric circulation in the summertime northeast Pacific, J. Clim., 8, 1140–1155, 1995.

Lebsock, M.D., Stephens, G.L., and Kummerow, C.: Multisensor satellite observations of aerosol effects on warm clouds, J. Geophys. Res. -Atmos., 113, 2008.

Lee, S.S., Feingold, G., and Chuang, P.Y.: Effect of Aerosol on Cloud-Environment Interactions in Trade Cumulus, J. Atmos.Sci., 69, 3607–3632, 2012.

Liu, Y., Daum, P.H., Guo, H., and Peng, Y.: Dispersion bias, dispersion effect, and the aerosol-cloud conundrum, Environmental Research Letters, 3, 2008.

Liu, Y.G. and Daum, P.H.: Anthropogenica erosols - Indirect warming effect from dispersion forcing, Nature, 419, 580–581, 2002.

Liu, Y.G. and Daum, P.H.: Parameterization of the autoconversion process. Part I: Analytical formulation of the Kessler-type parameterizations, J.Atmos. Sci., 61, 1539–1548, 2004.

Liu, Y.G., Daum, P.H., and McGraw, R.L.: Size truncation effect, threshold behavior, and a new type of autoconversion parameterization, Geophys. Res. Lett., 32, 2005.

Loeb, N.G. and Kato, S.: Top-of-atmosphere direct radiative effect of aerosols over the tropical oceans from the Clouds and the Earth's Radiant Energy System (CERES) satellite instrument, J. Clim., 15, 1474–1484, 2002.

Lohmann, U. and Feichter, J.: Global indirect aerosol effects: a review, Atmos. Chem. Phys., 5, 2005.

Lohmann, U., Stier, P., Hoose, C., Ferrachat, S., Kloster, S., Roeckner, E., and Zhang, J.: Cloud microphysics and aerosol indirect effects in the global climate model ECHAM5-HAM, Atmos. Chem. Phys.s, 7, 3425–3446, 2007.

Lu, C., Liu, Y., Niu, S., and Vogelmann, A.M.: Observed impacts of vertical velocity on cloud microphysics and implications for aerosol indirect effects, Geophys. Res. Lett., 39, 2012.

Martin, G.M., Johnson, D.W., and Spice, A.: The measurement and parameterization of effective radius of droplets in warm stratocumulus clouds, J.Atmos. Sci., 51, 1823–1842, 1994.

Matheson, M.A., Coakley, J.A., and Tahnk, W.R.: Aerosol and cloud property relationships for summertime stratiform clouds in the northeastern Atlantic from Advanced Very High Resolution Radiometer observations, J. Geophys. Res. -Atmos., 110, 2005.

Mauger, G.S. and Norris, J.R.: Meteorological bias in satellite estimates of aerosol-cloud relationships, Geophys. Res. Lett., 34, 2007.

McComiskey, A. and Feingold, G.: The scale problem in quantifying aerosol indirect effects, Atmos. Chem. Phys.s, 12, 1031–1049, 2012.

Mena-Carrasco, M., Ruiz, P., Stambuk, A., Stambuk, L., Granifo, R., and Jerardino, M.: Antecedentes para la Revision de las Normas Primarias de Calidad de Aire para Dioxido de Azufre

, Monoxido de Carbono, Ozono, Dioxido de Nitrogeno, 2010.

Morrison, H. and Pinto, J.O.: Mesoscale modeling of springtime Arctic mixed-phase stratiform clouds using a new two-moment bulk microphysics scheme, J.Atmos. Sci., 62, 3683–3704, doi: 10.1175/JAS3564.1, 2005.

Muñoz, R.C. and Alcafuz, R.I.: Variability of Urban Aerosols over Santiago, Chile: Comparison of Surface PM10 Concentrations and Remote Sensing with Ceilometer and Lidar, Aerosol and Air Quality Research, 12, 8–19, doi:10.4209/aaqr.2011.08.0133, 2012.

Nightingale, P.D., Malin, G., Law, C.S., Watson, A.J., Liss, P.S., Liddicoat, M.I., Boutin, J., and Upstill-Goddard, R.C.: In situ evaluation of air-sea gas exchange parameterizations using novel conservative and volatile tracers, Global Biogeochemical Cycles, 14, 373–387, doi: 10.1029/1999GB900091, 2000.

Norris, J.R. and Leovy, C.B.: Interannual variability in stratiform cloudiness and sea-surface temperature, J. Clim., 7, 1915–1925, 1994.

North, G.R., Bell, T.L., Cahalan, R.F., and Moeng, F.J.: Sampling errors in the estimation of empirical orthogonal functions, Monthly Weather Review, 110, 699–706, 1982.

Oreopoulos, L. and Platnick, S.: Radiative susceptibility of cloudy atmospheres to droplet number perturbations: 2. Global analysis from MODIS, J. Geophys. Res. -Atmos., 113, 2008.

Painemal, D. and Zuidema, P.: Assessment of MODIS cloud effective radius and optical thickness retrievals over the Southeast Pacific with VOCALS-REx in situ measurements, J. Geophys. Res. -Atmos., 116, 2011.

Painemal, D., Minnis, P., Ayers, J.K., and O'Neill, L.: GOES-10 microphysical retrievals in marine warm clouds: Multi-instrument validation and daytime cycle over the southeast Pacific, J. Geophys. Res.-Atmos., 117, D19 212, doi:10.1029/2012JD017822, 2012.

Penner, J.E., Andreae, M., Annegarn, H., Barrie, L., Feichter, J., Hegg, D., Jayaraman, A., Leaitch, R., Murphy, D., Nganga, J., and Pitari, G.: Aerosols, their Direct and Indirect Effects, in: Climate Change 2001: The Scientic Basis. Report to Intergovernmental Panel on Climate Change from the Scientic Assessment Working Group (WGI), edited by Houghton, J.T., Ding, Y., Griggs, D.J., Noguer, M., Vander Linden, P.J., Dai, X., Maskell, K., and Johnson, C.A., pp. 289–416, Cambridge University Press, Cambridge, UK, 2001.

Penner, J.E., Quaas, J., Storelvmo, T., Takemura, T., Boucher, O., Guo, H., Kirkevag, A., Kristjansson, J.E., and Seland, O.: Model intercomparison of indirect aerosol effects, Atmos. Chem. Phys.s, 6, 3391–3405, 2006.

Petterssen, S.: Weather Analysis and Forecasting, McGraw-Hill, New York, 1940.

Platnick, S. and Oreopoulos, L.: Radiative susceptibility of cloudy atmospheres to droplet number perturbations: 1. Theoretical analysis and examples from MODIS, J. Geophys. Res. -Atmos., 113, 2008.

Platnick, S. and Twomey, S.: Determining the susceptibility of cloud albedo to changes in droplet concentrations with the Advanced Very High Resolution Radiometer, J. Appl. Meteorol., 33, 334–347, doi:10.1175/1520-0450(1994)033¡0334:DTSOCA¿2.0.CO;2, 1994.

Quaas, J., Boucher, O., Bellouin, N., and Kinne, S.: Satellite-based estimate of the direct and indirect aerosol climate forcing, J. Geophys. Res. -Atmos., 113, 2008.

Quass, J., Bony, S., Collins, W., Donner, L., Illingworth, A., Jones, A., Lohmann, U., Satoh, M., Schwartz, S., Tao, W., and Wood, R.: Current Understanding and Quantifi cation of Clouds in the Changing Climate System and Strategies for Reducing Critical Uncertainties, in: Clouds in the Perturbed Climate System:Their Relationship to Energy Balance, edited by Heintzenberg, J. and Charlson, R., MIT press, 2009.

Rahn, D.A. and Garreaud, R.: Marine boundary layer over the subtropical southeast Pacific during VOCALS-REx - Part 1: Mean structure and diurnal cycle, Atmos. Chem. Phys., 10, 2010a.

Rahn, D.A. and Garreaud, R.: Marine boundary layer over the subtropical southeast Pacific during VOCALS-REx - Part 2: Synoptic variability, Atmos. Chem. Phys., 10, 2010b.

Randall, D., Wood, R., Bony, S., Colman, R., Fichefet, T., Fyfe, J., Kattsov, V., Pitman, A., Shukla, J., Srinivasan, J., Stouffer, R., Sumi, A., and Taylor, K.: Climate Models and Their Evaluation., in: Climate Change 2007: The Physical Science Basis. Contribution of Working Group I to the Fourth Assessment Report of the Intergovernmental Panel on Climate Change, pp. 153–185, Cambridge University Press, Cambridge, United Kingdom and New York, NY, USA, 2007.

Richter, I. and Mechoso, C.R.: Orographic influences on the annual cycle of Namibian stratocumulus clouds, Geophys. Res. Lett., 31, 2004.

Riddle, E.E., Voss, P.B., Stohl, A., Holcomb, D., Maczka, D., Washburn, K., and Talbot, R.W.: Trajectory model validation using newly developed altitude-controlled balloons during the International Consortium for Atmospheric Research on Transport and Transformations 2004 campaign, J. Geophys. Res.-Atmos., 111, D23S57, doi:10.1029/2006JD007456, 2006.

Rossow, W.B., Delo, C., and Cairns, B.: Implications of the observed mesoscale variations of clouds for the Earth's radiation budget, J. Clim., 15, 557–585, 2002.

Rozendaal, M.A., Leovy, C.B., and Klein, S.A.: An observational study of diurnal-variations of marin stratiform cloud, J. Clim., 8, 1795–1809, 1995.

Rutllant, J.A. and Garreaud, R.D.: Episodes of strong flow down the western slope of the subtropical

Andes, Monthly Weather Review, 132, 611–622, 2004.

Saide, P.E., Spak, S.N., Carmichael, G.R., Mena-Carrasco, M.A., Yang, Q., Howell, S., Leon, D.C., Snider, J.R., Bandy, A.R., Collett, J.L., Benedict, K.B., deSzoeke, S.P., Hawkins, L.N., Allen, G., Crawford, I., Crosier, J., and Springston, S.R.: Evaluating WRF-Chem aerosol indirect effects in Southeast Pacific marine stratocumulus during VOCALS-REx, Atmos. Chem. Phys., 12, 2012.

Saide, P.E., Carmichael, G.R., Spak, S.N., Minnis, P., and Ayers, J.: Improving aerosol distributions below clouds by assimilating satellite-retrieved cloud droplet number, PNAS, 109, 11 939–11 943, 2012b.

Sandu, I., Brenguier, J.L., Thouron, O., and Stevens, B.: How important is the vertical structure for the representation of aerosol impacts on the diurnal cycle of marine stratocumulus?, Atmos. Chem. Phys.s, 9, 4039–4052, 2009.

Schell, B., Ackermann, I.J., Hass, H., Binkowski, F.S., and Ebel, A.: Modeling the formation of secondary organic aerosol within a comprehensive air quality model system, J. Geophys. Res.-Atmos., 106, 28 275–28 293, doi:10.1029/2001JD000384, 2001.

Schüller, M., Estrada, A., and Bringezu, S.: Mapping environmental performance of international raw material production ows: a comparative case study for the copper industry of Chile and Germany, Miner. Energ., 23, 29–45, 2008.

Schwartz, S.E., Harshvardhan, and Benkovitz, C.M.: Influence of anthropogenic aerosol on cloud optical depth and albedo shown by satellite measurements and chemical transport modeling, P. Natl. Acad. Sci. U.S.A., 99, 1784–1789, doi:10.1073/pnas.261712099, 2002.

Seinfeld, J. and Pandis, S.: Atmospheric Chemistry and Physics: From Air Pollution to Climate Change, J. Wiley, New York, 1st edn., 1998.

Shank, L.M., Howell, S., Clarke, A.D., Freitag, S., Brekhovskikh, V., Kapustin, V., McNaughton, C., Campos, T., and Wood, R.: Organic matter and non-refractory aerosol over the remote Southeast Pacific: oceanic and combustion sources, Atmos. Chem. Phys., 12, 2012.

Slingo, A. and Schrecker, H.M.: On the shortwave radiative properties of stratiform water clouds, Quarterly Journal of the Royal Meteorological Society, 108, 407–426, 1982.

Snider, J.R., Petters, M.D., Wechsler, P., and Liu, P. S.K.: Supersaturation in the Wyoming CCN instrument, J. Atmos. Ocean. Tech., 23, 1323–1339, doi:10.1175/JTECH1916.1, 2006.

Stephens, G.L.: Radiation profiles in extended water clouds. 1. Theory, J.Atmos. Sci., 35, 2111–2122, 1978.

Stephens, G.L. and Kummerow, C.D.: The remote sensing of clouds and precipitation from space: A review, J.Atmos. Sci., 64, 3742–3765, stephens, Graeme L. Kummerow, Christian D., 2007.

Stevens, B. and Feingold, G.: Untangling aerosol effects on clouds and precipitation in a buffered system, Nature, 461, 607–613, 2009.

Stevens, B., Cotton, W.R., Feingold, G., and Moeng, C.H.: Large-eddy simulations of strongly precipitating, shallow, stratocumulus-topped boundary layers, J.Atmos. Sci., 55, 3616–3638, 1998.

Stockwell, W.R., Middleton, P., Chang, J.S., and Tang, X.Y.: The second generation regional acid deposition model chemical mechanism for regional air quality modeling, J. Geophys. Res.-Atmos., 95, 16 343–16 367, doi:10.1029/JD095iD10p16343, 1990.

Stohl, A., Wotawa, G., Seibert, P., and Krompkolb, H.: Interpolation errors in wind fields as a function of spatial and temporal resolution and their impact on different types of kinematic trajectories, J. Appl. Meteorol., 34, 2149–2165, doi:10.1175/1520-0450(1995)034¡2149:IEIWFA¿2.0.CO;2, 1995.

Szczodrak, M., Austin, P.H., and Krummel, P.B.: Variability of optical depth and effective radius in marine stratocumulus clouds, J.Atmos. Sci., 58, 2912–2926, 2001.

Takahashi, K. and Battisti, D.S.: Processes controlling the mean tropical pacific precipitation pattern. Part II: The SPCZ and the southeast pacific dry zone, J. Clim., 20, 5696–5706, 2007.

Terai, C.R., Wood, R., Leon, D.C., and Zuidema, P.: Does precipitation susceptibility vary with increasing cloud thickness in marine stratocumulus?, Atmos. Chem. Phys.s, 12, 4567–4583, 2012.

Thornton, D.C., Bandy, A.R., Tu, F.H., Blomquist, B.W., Mitchell, G.M., Nadler, W., and Lenschow, D.H.: Fast airborne sulfur dioxide measurements by Atmospheric Pressure Ionization Mass Spectrometry (APIMS), J. Geophys. Res.-Atmos., 107, 4632, doi:10.1029/2002JD002289, 2002.

Toniazzo, T., Abel, S.J., Wood, R., Mechoso, C.R., Allen, G., and Shaffrey, L.C.: Large-scale and synoptic meteorology in the south-east Pacific during the observations campaign VOCALS-REx in austral Spring 2008, Atmos. Chem. Phys., 11, 2011.

Tsapakis, M., Lagoudaki, E., Stephanou, E.G., Kavouras, I.G., Koutrakis, P., Oyola, P., and von Baer, D.: The composition and sources of PM2.5 organic aerosol in two urban areas of Chile, Atmos. Environ., 36, 3851–3863, doi:10.1016/S1352-2310(02)00269-8, 2002.

Twohy, C.H., Petters, M.D., Snider, J.R., Stevens, B., Tahnk, W., Wetzel, M., Russell, L., and Burnet, F.: Evaluation of the aerosol indirect effect in marine stratocumulus clouds: Droplet number, size, liquid water path, and radiative impact, J. Geophys. Res. -Atmos., 110, 2005.

Twohy, C.H., Anderson, J.R., Toohey, D.W., Andrejczuk, M., Adams, A., Lytle, M., George, R.C., Wood, R., Saide, P., Spak, S., Zuidema, P., and Leon, D.: Impacts of aerosol particles on the microphysical and radiative properties of stratocumulus clouds over the Southeast Pacific ocean,

Atmos. Chem. Phys. Discuss., 12, 19 715–19 767, 2012.

Twomey, S.: Pollution and planetary albedo, Atmos. Environ., 8, 1251–1256, doi:10.1016/0004-6981(74)90004-3, 1974.

Wang, S.P., Wang, Q., and Feingold, G.: Turbulence, condensation, and liquid water transport in numerically simulated nonprecipitating stratocumulus clouds, J.Atmos. Sci., 60, 262–278, 2003.

Wang, T., Li, S., Shen, Y., Deng, J., and Xie, M.: Investigations on direct and indirect effect of nitrate on temperature and precipitation in China using a regional climate chemistry modeling system, J. Geophys. Res. -Atmos., 115, 2010.

Wood, R.: Drizzle in stratiform boundary layer clouds. Part II: Microphysical aspects, J.Atmos. Sci., 62, 3034–3050, 2005.

Wood, R.: Cancellation of aerosol indirect effects in marine stratocumulus through cloud thinning, J.Atmos. Sci., 64, 2657–2669, 2007.

Wood, R.: Stratocumulus Clouds, Mon. Weather Rev., 140, 2012.

Wood, R. and Bretherton, C.S.: Boundary layer depth, entrainment, and decoupling in the cloud-capped subtropical and tropical marine boundary layer, J. Clim., 17, 3576–3588, 2004.

Wood, R. and Bretherton, C.S.: On the relationship between stratiform low cloud cover and lower-tropospheric stability, J. Clim., 19, 6425–6432, 2006.

Wood, R. and Hartmann, D.L.: Spatial variability of liquid water path in marine low cloud: The importance of mesoscale cellular convection, J. Clim., 19, 1748–1764, 2006.

Wood, R. and Taylor, J.P.: Liquid water path variability in unbroken marine stratocumulus cloud, Quarterly Journal of the Royal Meteorological Society, 127, 2635–2662, 2001.

Wood, R., Bretherton, C.S., and Hartmann, D.L.: Diurnal cycle of liquid water path over the subtropical and tropical oceans, Geophys. Res. Lett., 29, 2002.

Wood, R., Comstock, K.K., Bretherton, C.S., Cornish, C., Tomlinson, J., Collins, D.R., and Fairall, C.: Open cellular structure in marine stratocumulus sheets, J. Geophys. Res. -Atmos., 113, 2008.

Wood, R., Bretherton, C.S., Leon, D., Clarke, A.D., Zuidema, P., Allen, G., and Coe, H.: An aircraft case study of the spatial transition from closed to open mesoscale cellular convection over the Southeast Pacific, Atmos. Chem. Phys., 11, 2011a.

Wood, R., Mechoso, C.R., Bretherton, C.S., Weller, R.A., Huebert, B., Straneo, F., Albrecht, B.A., Coe, H., Allen, G., Vaughan, G., Daum, P., Fairall, C., Chand, D., GallardoKlenner, L., Garreaud, R., Grados, C., Covert, D.S., Bates, T.S., Krejci, R., Russell, L.M., deSzoeke, S., Brewer, A., Yuter, S.E., Springston, S.R., Chaigneau, A., Toniazzo, T., Minnis, P., Palikonda, R., Abel, S.J., Brown, W. O.J., Williams, S., Fochesatto, J., Brioude, J., and Bower, K.N.: The VAMOS Ocean-

Cloud-Atmosphere-Land Study Regional Experiment (VOCALS-REx): goals, platforms, and field operations, Atmos. Chem. Phys., 11, 2011b.

Wood, R., Leon, D., Lebsock, M., Snider, J., and Clarke, A.D.: Precipitation driving of droplet concentration variability in marine low clouds, J. Geophys. Res. -Atmos., 117, 2012.

Woodhouse, M.T., Carslaw, K.S., Mann, G.W., Vallina, S.M., Vogt, M., Halloran, P.R., and Boucher, O.: Low sensitivity of cloud condensation nuclei to changes in the sea-air flux of dimethyl-sulphide, Atmos. Chem. Phys., 10, 2010.

Wyant, M.C., Wood, R., Bretherton, C.S., Mechoso, C.R., Bacmeister, J., Balmaseda, M.A., Barrett, B., Codron, F., Earnshaw, P., Fast, J., Hannay, C., Kaiser, J.W., Kitagawa, H., Klein, S.A., Kohler, M., Manganello, J., Pan, H.L., Sun, F., Wang, S., and Wang, Y.: The PreVOCA experiment: modeling the lower troposphere in the Southeast Pacific, Atmos. Chem. Phys.s, 10, 4757–4774, 2010.

Xu, H.M., Xie, S.P., and Wang, Y.Q.: Subseasonal variability of the southeast Pacific stratus cloud deck, J. Clim., 18, 131–142, 2005.

Xue, H.W. and Feingold, G.: Large-eddy simulations of trade wind cumuli: Investigation of aerosol indirect effects, J.Atmos. Sci., 63, 1605–1622, 2006.

Yang, M., Huebert, B.J., Blomquist, B.W., Howell, S.G., Shank, L.M., McNaughton, C.S., Clarke, A.D., Hawkins, L.N., Russell, L.M., Covert, D.S., Coffman, D.J., Bates, T.S., Quinn, P.K., Zagorac, N., Bandy, A.R., deSzoeke, S.P., Zuidema, P.D., Tucker, S.C., Brewer, W.A., Benedict, K.B., and Collett, J.L.: Atmospheric sulfur cycling in the southeastern Pacific - longitudinal distribution, vertical profile, and diel variability observed during VOCALS-REx, Atmos. Chem. Phys.s, 11, 5079–5097, 2011a.

Yang, Q., Gustafson, W.I., Jr., Fast, J.D., Wang, H., Easter, R.C., Morrison, H., Lee, Y.N., Chapman, E.G., Spak, S.N., and Mena-Carrasco, M.A.: Assessing regional scale predictions of aerosols, marine stratocumulus, and their interactions during VOCALS-REx using WRF-Chem, Atmos. Chem. Phys., 11, 2011b.

Yang, Q., Gustafson, W.I., Jr., Fast, J.D., Wang, H., Easter, R.C., Wang, M., Ghan, S.J., Berg, L.K., Leung, L.R., and Morrison, H.: Impact of natural and anthropogenic aerosols on stratocumulus and precipitation in the Southeast Pacific: a regional modelling study using WRF-Chem, Atmos. Chem. Phys.s, 12, 8777–8796, 2012.

Zhang, M.H., Lin, W.Y., Klein, S.A., Bacmeister, J.T., Bony, S., Cederwall, R.T., DelGenio, A.D., Hack, J.J., Loeb, N.G., Lohmann, U., Minnis, P., Musat, I., Pincus, R., Stier, P., Suarez, M.J., Webb, M.J., Wu, J.B., Xie, S.C., Yao, M.S., and Zhang, J.H.: Comparing clouds and their seasonal

variations in 10 atmospheric general circulation models with satellite measurements, J. Geophys. Res. -Atmos., 110, 2005.

Zhou, M.Y., Zeng, X.B., Brunke, M., Zhang, Z.H., and Fairall, C.: An analysis of statistical characteristics of stratus and stratocumulus over eastern Pacific, Geophys. Res. Lett., 33, 2006.

Zuidema, P., Painemal, D., deSzoeke, S., and Fairall, C.: Stratocumulus Cloud-Top Height Estimates and Their Climatic Implications, J. Clim., 22, 4652–4666, 2009.

Appendix A

VARIANCE OF A PRODUCT

A.1

Variance of a product

We let A be a simple product of two variables:

$$A = XY \tag{A.1}$$

We can rephrase each variable V as a sum of a mean $\overline{v}$ and a perturbation $v^{'}$, such that $A = \overline{a} + a^{'}, X = \overline{x} + x^{'}$ and $Y = \overline{y} + y^{'}$. So

$$A^2 = \overline{a}^2 + a^{'2} + 2\overline{a}a^{'} \tag{A.2}$$

The mean of the perturbations is 0 by construction, so

$$\overline{A^2} = \overline{a}^2 + \overline{a^{'2}}. \tag{A.3}$$

$\overline{a^{'2}}$ is an estimate of the variance of A defined by

$$\sigma_a^2 = \lim_{N\to\infty} \frac{1}{N} \sum_{i=1}^{N} (a_i - \overline{a})^2 \approx \overline{a^{'2}}. \tag{A.4}$$

So the variance of A is estimated to be

$$\overline{a^{'2}} = \overline{[(\overline{x} + x^{'})(\overline{y} + y^{'})]^2} - \overline{(\overline{x} + x^{'})(\overline{y} + y^{'})}^2. \tag{A.5}$$

Expanding the terms and removing mean of single perturbation terms, this becomes

$$\overline{a^{'2}} = \overline{y}^2\overline{x^{'2}} + \overline{x}^2\overline{y^{'2}} + 2\overline{x}\overline{y}\overline{x^{'}y^{'}} + 2\overline{x}\overline{x^{'}y^{'2}} + 2\overline{y}\overline{x^{'2}y^{'}} + \overline{x^{'2}y^{'2}} - (\overline{x^{'}y^{'}})^2. \tag{A.6}$$

Which can be further algebraically simplified by combining the third order terms and a fourth order term with the first order terms in (A6).

$$\overline{a^{'2}} = \overline{X^2y^{'2}} + \overline{x^{'2}Y^2} + 2(\overline{x})(\overline{y})\overline{x^{'}y^{'}} - \left[\overline{x^{'2}y^{'2}} + (\overline{x^{'}y^{'}})^2\right]. \tag{A.7}$$

Substituting albedo, for A, α_{cld}-α_{clear} for X and f_c for Y gives Eq.(5).

We interpret the first term in (A7) as the contribution of Y variance to the variance of A. Besides some leftover fourth order terms, this combines all terms that involve the variance of Y. Although the value of X plays a role in this term, the squared coefficients of variation of variable considered in this study were small ($\left(\frac{x'}{\overline{x}}\right)^2 < 1$) in the domain considered, so variations in should be relatively unimportant in the term compared to y'^2 and the average product thus represents the contribution from the variance in Y. Similarly the second term represents the contribution from the variance in X, and the third the contribution from the covariance between X and Y. The final term is fourth order nonlinear effects.

Because it is possible for some of these terms to be negative, the relative contribution of each term is computed by dividing each term by the sum of the absolute values of all terms.

$$\overline{a'^2_{\text{abs}}} = \left|\overline{X^2 y'^2}\right| + \left|\overline{x'^2 Y^2}\right| + \left|2\overline{x}\,\overline{y}\,\overline{x'y'}\right| + \left|-\overline{x'^2 y'^2} - \left(\overline{x'y'}\right)^2\right|. \tag{A.8}$$

Appendix B

TRAJECTORIES

Trajectories are computed by solving the equation

$$\mathrm{d}\vec{X}/\mathrm{d}t = \vec{v}(\vec{X}(t), t) \tag{B.1}$$

where t is time, $\vec{X}$ is the position vector, and $\vec{v}$ the wind vector in 3 dimensions. This equation is integrated over time using the iterative Petterssen (1940) scheme.

$$\vec{X}(t_i) = \vec{X}(t_{i-1}) + dt/2 \cdot \{\vec{v}(\vec{X}(t_{i-1}), t_{i-1}) + \vec{v}(\vec{X}(t_i), t_i)\} \tag{B.2}$$

$\vec{X_{\mathrm{init}}}(t_i)$ is initially approximated as $\vec{X}(t_{i-1}) + \vec{v}(\vec{X}(t_{i-1}), t_{i-1}) \cdot dt$. Then $\vec{v}(\vec{X_{\mathrm{init}}}(t_i), t_i)$ is interpolated to compute a new $\vec{X}(t_i)$ from Eq. (A2). If $\vec{X}(t_i) - \vec{X_{\mathrm{init}}}(t_i)$ is below a threshold error, the iteration stops, otherwise $\vec{X}(t_i)$ becomes the new $\vec{X_{\mathrm{init}}}(t_i)$ and the calculation continues until $\vec{X}(t_i) - \vec{X_{\mathrm{init}}}(t_i)$ is sufficiently small. 3D ECMWF trajectories are computed using its hybrid sigma pressure coordinates, while the WRF-Chem trajectories are based on the terrain following eta coordinate. 2D trajectories are computed by setting vertical velocity to 0. Trajectories are computed both forward and backward in time.

2D MBL model trajectories start from two model levels below the inversion, which is around 900-950 mb and 2D ECMWF trajectories start at 950 mb. Trajectories remain at a fixed eta or hybrid sigma pressure level, and given the deepening of the boundary layer in the SEP east-west direction, trajectories forward in time are further below the inversion than earlier along the trajectory. Due to the relative homogeneity (little shear) of winds within the boundary layer, these trajectories track the hook (model or observed) well.

Over the ocean computed trajectories are assumed to capture the direction and magnitude of transport because of the strong meteorological forcing of the subtropical high and relative homogeneity of the MBL winds. Near the Andes the land-sea thermal contrast, diurnal land heating cycle, and mountain effects complicate the wind fields. Enough variability occurs within the 6 hour timesteps of the ECMWF that confidence in the path of

the ECMWF trajectories over land is greatly reduced. Model trajectories computed at 3 hour intervals are subject to similar time resolution errors, but in some cases follow plumes of high CCN quite well (Figs. 4.11 and 4.12).

Over short periods of time an idealize parcel will be representative of air motion (Stohl et al., 1995). The length of time that trajectories continue to represent bulk transport of air is a limiting factor in using trajectory analysis. Sources of trajectory errors include the length of the timestep, wind field errors due to subgrid variability not captured by interpolation, and wind gradient errors (Riddle et al., 2006).